Quaternary defect adamantine compounds of the type I-III-IV-^{2}-VI4.

Rivera, Adan Lopez

Award date:
1981

Awarding institution:
University of Bath

Quaternary Defect Adamantine Compounds of the Type $I\text{-}III\text{-}IV\text{-}\square\text{-}VI_4$

submitted by Adán López Rivera

for the degree of Ph.D.

of the University of Bath

1981

Copyright

S. Adán López R.

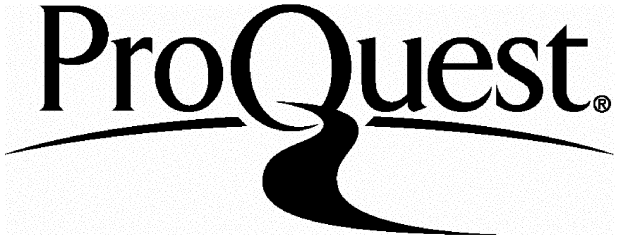

ABSTRACT

A review of the systematic prediction of new quaternary materials is given. Many new quaternary adamantine phases are proposed. The preparation of a range of polycrystalline selenides and sulphides of composition I-III-IV-□-VI_4 was undertaken. In twelve selenide compounds and three of the sulphur compounds the structure was found to be tetragonal with a c/a ratio of approximately 2. A systematic variation of unit cell volume and c/a was found over the entire range of compounds grown. Single crystals of $CuGaSn□Se_4$, $CuGaGe□Se_4$, $AgGaSn□Se_4$ and $AgGaGe□Se_4$ were grown by a modification of the Pendölofen vapour transport method. This interesting technique proved that it is possible to transport simultaneously three non-volatile metals in a closed tube. Single crystal diffraction methods have been used to solve the crystal structure of $CuGaSn□Se_4$. The structure was found to be the partially ordered defect chalcopyrite structure, space group $I\bar{4}2d$ (D_{2d}^{12}) copper and gallium are on one metallic sublattice and tin and vacancy on the other of the ABX_2 pattern. Room temperature lattice parameters were determined for all the compounds, and the variations of the lattice parameters with temperature up to the melting point of $CuGaSn□Se_4$ were studied using a high temperature x-ray camera. This compound shows an increase in the tetragonal compression with temperature. The results are interpreted in terms of the thermal expansions of the A-Se ($A = \frac{1}{2}(Cu + Ga)$) and B-Se ($B = \frac{1}{2}(Sn + □)$) bonds. The fundamental absorption edges of the compounds were studied at

room temperature, and the lowest direct transitions were determined at room temperature by reflectance and wavelength modulation reflectance. The reflectance measurements of $CuGaSn\square Se_4$ were studied at different temperatures between 4K to room temperature (295K) to find the temperature dependence of the band structure. It was deduced that all the compounds have direct gaps. The principles of operation and construction details of a sensitive wavelength modulation spectrometer are described. The derivative spectra of these compounds show clear improvement of resolution over the conventional technique. The melting points and transition temperatures were determined for some of these compounds by differential thermal analysis.

ACKNOWLEDGEMENTS

I would like to thank Dr.B.R.Pamplin for his continual help and encouragement throughout this work and the Universisad de los Andes for my financial support.

My thanks are also due to Professor G.A.Saunders, Dr.W.C.Clark, Mr.R.C.J.Draper, Mr.B.Chapman, Mr.H.Hopkins, for many helpful and stimulating discussions and much experimental assistance.

Part of the work of this thesis was carried out at Ottawa University, so I must thank Professor J.C.Woolley for his help his invitation and the hospitality received.

My thanks also go to Mrs. Megan Hughes-Jones for typing the manuscript.

Quaternary Defect Adamantine Compounds of the Type I-III-IV-□-VI_4

CONTENTS

Chapter 3. Quaternary defect adamantine compounds, synthesis, growth and characterization

Chapter 4. Crystal structure analysis, temperature dependence of lattice parameters and thermal expansion of $CuGaSn\square Se_4$

Chapter 5. Optical properties of I-II-IV- -VI_4 semiconductors

Chapter 6. Study of the optical properties of I-III-IV-□-VI_4 semiconductors by wavelength modulation

Chapter 7. Conclusions

CHAPTER 1

GENERAL INTRODUCTION

The first important application of semiconductors was to provide rectifiers for low-frequency alternating currents. But the most fortunate application came with the discovery of transistor action and the invention of the transistor. Another important application is the infra-red detectors. The modern successor to the transistor is the integrated circuit (I.C.). This silicon chip technology has revolutionized the electronics industry for the second time and has made complex systems such as the modern electronic digital microprocessor possible.

A new application followed with the study of the optical properties of semiconductors, the solid state laser. This has provided a tunable light source of very narrow bandwidth. As a source it can be modulated and linked to optical fibres and is playing a vital part in optical communications. A less complex but related device is the light-emitting diode. (Though this application is becoming less important with the new technology of liquid-crystals).

The discovery of the laser and the interest in nonlinear optical material in the 1950s stimulated renewed effort in the research of new semiconductors.

One universal feature in the search for new inorganic semiconductors is its interdisciplinary nature of the research. (Solid state physics and chemistry, crystallography etc.) The primary aim of the investigation is neither to determine the physics of a material nor its chemistry, but rather their mutual interaction.

Compounds with structures related to the diamond structure (which is one of the most symmetrical arrangements of atoms known in crystallography) have extensive potential applications for semiconductors devices. Any compound with a structure derived from the tetrahedrally bonded diamond structure can be called adamantine. We can say that the roots of the adamantine family are the elements of the group IV of the periodic table. The binary compounds II-VI and III-V follow and they are used for certain special applications. The obvious next step is the ternary compounds; these are the grandchildren of the group IV. The next "generation" of this important family of semiconductors are the quaternary compounds. These quaternary compounds are divided into two groups, one is the normal quaternary adamantine compounds and the defect quaternary adamantine compounds. The object of this thesis is to consider the possibility of preparing and growing crystals of the defect quaternary compounds with composition I-III-IV-□-VI_4, and then to find the structure and characterize these compounds.

We have divided this thesis into seven chapters. The second chapter contains a review of the general characteristic of the adamantine family of semiconductors, their systematic prediction and all the quaternary compound, synthesized up till now, including some of the compounds which have been synthesized for the first time in this work. Chapter 3 develops the method of synthesis and crystal growth of these compounds. Also we consider two different characterizations; one is the x-ray powder analysis and the other is the differential thermal analysis. Chapter 4 contains the determination of the chemical composition, crystal structure analysis by single crystal methods, temperature

dependence of lattice parameters and evaluation of the coefficients of thermal expansions of $CuGaSn\square Se_4$. Chapter 5 presents the study of the optical properties of I-III-IV-□-VI_4 semiconductors, and the behaviour of band structure with the temperature. Chapter 6 contains the study of the optical properties of $AgGaSn\square Se_4$ and $CuGaGe\square Se_4$ by wavelength modulation reflectance and a description of the experimental technique and apparatus. Chapter 7 contains the concluding discussion.

CHAPTER 2

FORMATION OF QUATERNARY ADAMANTINE COMPOUNDS

2.1 Introduction

The experimental and theoretical investigations of the adamantine group of compounds was the first contribution of the new science of semiconductor physics to engineering and electronics. Compounds with structures related to the diamond structure have extensive potential applications for semiconductor devices. Practical requirements outstrip the actual possibilities of the science of semiconductor materials. New compounds and alloys with new qualities and combinations of properties are constantly needed.

In the field of adamantine compounds, one of the trends of this research is concerned with systematic prediction, preparation and growth of new materials on the basis of complex, multicomponent substances of the diamond-zinc blende related structures. Binary compounds have been fairly fully exploited. The ternary compounds have attracted widespread interest in the last past twenty years. The obvious next step, leads to the consideration of quaternary compounds. The numbers of quaternary and even higher compounds is quite large. Some compositions of this group of quaternary compounds have been studied but not in depth and it will indeed be surprising if one or two new materials with rather special properties do not emerge.

It is the object of this chapter to review the general characteristics of the family of adamantine compounds, their systematic prediction and to consider specially the group of quaternary compounds. This group is divided into two sub-groups; the normal quaternary adamantine compounds and the defect

quaternary adamantine compounds. The list of these two sub-groups, together with their structure and lattice parameters are given in tables 2.1 and 2.2. We include in this list the compounds studied in this work, some of which have been synthesized for the first time.

2.2 General characteristic for adamantine compounds

The group IV elements of the periodic table C, Si, Ge, α-Sn have the diamond structure which consists of two interpenetrating face centered cubic lattices, arranged so that each atom has four neighbours at the corners of a regular tetrahedron bonded by hybrid sp^3 orbitals (symmetry Fd3m or O_h^7). The directions of four equivalent sp^3 hybrid orbitals form tetrahedral angles of 109.4^o with each other.

There is another structure of silicon and carbon, also tetrahedrally bonded to four neighbours, this is the rare lonsdaleite structure which consists of two interpenetrating hexagonal close packed lattices (symmetry $P6_3/mmc$ or D_{6h}^4).

Any compound with a structure derived from one or both of these tetrahedrally bonded parents is called adamantine.

A perfect sp^3 hybrid should occur only if one atom is bonded to four equal ligand atoms. If the ligands are not identical the tetrahedrons are most probably slightly distorted and the tetrahedral bonds are bent. (This is the case for chalcopyrite). This deviation from the ideal tetrahedral bond angle has been explained by taking the wave functions of the hybrid orbitals but combined with different amounts of s wave functions. Other complications arise in some compounds where d and f wave functions also participate in the hybridization.

By definition, a structure is called a normal tetrahedral structure if every atom in the structure has four nearest neighbours which are located at the vertices of a surrounding tetrahedron. (1).

There is a special group of tetrahedral structures, the group of defect tetrahedral structures. These structures do not have all four corners of the tetrahedron occupied with an atom. In order to discuss these two groups, we can define a parameter, z, the ratio of the numbers of cations and anions in a unit cell (2):

$$z = \frac{\text{number of cations in a unit cell}}{\text{number of anions in a unit cell}}$$

The z value of a normal tetrahedral structure is one, and for the defect tetrahedral structure is less than one.

It is interesting to try and specify the rules for the existence of adamantine compounds. These general descriptive rules are guides in the search for entirely new semiconductors. The simplest kind of derived adamantine compounds has been to make use of compounds that are related to the elemental semiconductors of group IV of the periodic table by the rule of cross-substitution. In this rule the condition being that the valence-electron: atom remains constant. An example of this rule is given in figure 2.1.

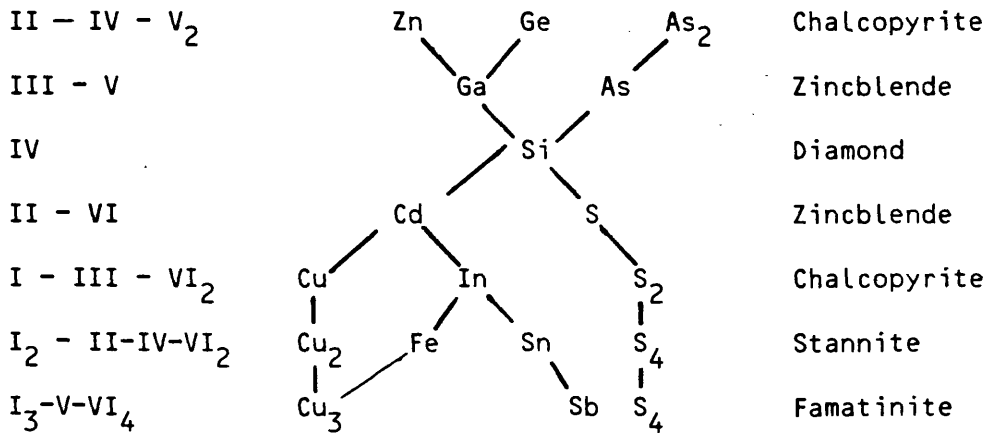

Fig. 2.1. Relationship between diamond and normal tetrahedral structures by the cross-substitution rule.

The given splitting diagram is one of several possibilities. The question arises as to how to tabulate all possible compositions of adamantine structures.

All the possible adamantine compounds must have an average valence electron concentration of four per atom or more general per site. This valence electron concentration rule was found by Pamplin (3) and Parthe (4) independently. This rule means that every atom has on the average four electrons and will form an sp^3 hybrid with four tetrahedral orbitals. The orbitals of neighbouring atoms will interact to form covalent bonds. A vacancy in the case of defect tetrahedral structures is surrounded by four neighbour atoms, each of them extending one of its tetrahedral orbitals in the direction of the vacancy. These four orbitals are not used for bonding. Every tetrahedral orbital which is not used for bonding must obtain a second electron with antiparallel spin to become a non-bonding orbital.

This rule may also be derived from either Goldschmidt's rule or the Mooser and Pearson rule for semiconductors. There are exceptions to this rule. Thus CuH and CuD are wurtzite structure, for reasons of close packing one supposes. We can write this rule in the form of equation:

$$\frac{\Sigma\, n_i v_i}{\Sigma\, n_i} = 4 \qquad (2.1)$$

Where n_i is the number of atoms of the i^{th} kind per formula and v_i the number of outer valence electrons. Vacant sites are counted but assigned zero valence. For example consider the ordered quaternary Cu_2FeSnS_4 (the mineral stannite). It is a tetragonal analogue of the zincblende structure; $a \approx a_z$ and $c \approx 2a_z$.

Applying equation (2.1) one obtains

$$\frac{(2)(1)+(1)(2)+(1)(4)+(4)(6)}{2+1+1+4} = \frac{32}{8} = 4$$

Another example is a partially ordered defect chalcopyrite quaternary $CuGaSn\square Se_4$. Applying equation (2.1) one obtains

$$\frac{(1)(1)+(1)(3)+(1)(4)+(1)(0)+(4)(6)}{1+1+1+1+4} \cong \frac{32}{8} = 4$$

Earlier it was believed that adamantine compounds with mixed anions could not form. But the II_3-□-V-VII_3 compounds: $Zn_3\square PI_3$ and $Zn_3\square AsI_3$ and the I-III_2-□-VI_3-VII compounds: $AgIn_2\square Se_3I$, $CuIn_2\square Se_3Br$ and $CuIn_2\square Se_3I$ show that they are true ternary and quaternary adamantine compounds.

Some of the heavy elements of the 6th period Au, Tl, Pb have difficulties in forming sp^3 hybrids. Gold and lead compounds with tetrahedral structure are not known. The different energy levels in these heavy atoms (5d, 5f, 6s, 6p) are very close together. Different kinds of hybridization involving d or f electrons may therefore successfully compete with the sp^3 hybridization. In general, atoms with partly filled d shells prefer to form hybridizations which also involve d electrons. This leads to octahedral structures, structures with planar four coordination, and others, but not tetrahedral structures.

The atoms of alkali and alkaline earth metals of the fourth and higher period are not found in tetrahedral structures. The electronegativity coefficients of these elements have the value of one, or smaller than that. Instead of picking up three or two electrons respectively as required for an sp^3 hybrid, these atoms prefer to give away the valence electrons to form single, or respectively double, positive ions with inert gas electronic structures. As a matter of interest it should be noted that in the

example given in Fig. 2.1 the cross-substitution has been confined to the cationic constituents. In principle it might be expected that the anionic sub-lattice should be capable of cross-substitution and that a series of structures should exist anti-isomorphous to those already described. Goodman (5) reported an attempt to prepare some III_2-IV-VI anti-chalcopyrite compounds. Al_2SnTe, Al_2GeTe, and Al_2GeSe compositions proved very unstable in air, with rapid evolution of H_2Te or H_2Se. The expected anti-chalcopyrite structures were not obtained, but the possibility of such series can not be entirely ruled out. One explanation of this point should be the lower energy of the segregated phases.

In compounds and alloys the two interpenetrating close packed lattices, that make up with the related sphalerite and wurtzite structures, must be populated with equal numbers of cation and anion sites.

2.3 Extending the adamantine family

We have seen that the adamantine family can be extended by considering pseudo binary (or pseudo ternary) systems of known adamantine phases.

We can say that the roots of the adamantine family are the elements of the group IV of the periodic table. In this group, silicon which is one of the simplest semiconductors of this family, remains by far the most important one in practice. The binary compounds follow and they are used for certain special applications, (such as GaAs). The obvious next step, in the pursuit of variety (and lowered symmetry) to meet particular needs, leads to the consideration of ternary compounds. These are the grandchildren of the group IV, being notionally related to them

as shown in Fig. 2.1. These compounds have attracted widespread interest in the last two decades. While they have not yet found extensive commercial applications, they have become established as a topic of continued research. In a book devoted entirely to the subject of ternary chalcopyrite semiconductors J.L. Shay and J.H. Wernick have dealt with the known properties (until 1975) of a large number of compounds (6). There is also a series of proceedings of international conferences about these materials.

The next "generation" of this important family of semiconductors are the quaternaries. The possibility of having quarternary compound semiconductors, has been appreciated for some time, but very little progress has been made in this direction, mainly owing to the difficulties of making the compounds.

Clearly, when we include ternary and quaternary or even higher, compounds the number of possible semiconducting compounds becomes very great. The complete list of this adamantine family would be tediously long, and out of the scope of this thesis. Instead we shall discuss the possible list of the quaternary compound semiconductors in the next section of this chapter.

2.4 Quaternary normal adamantine structure compounds

Simple considerations, based on the rules for adamantine family of semiconductors, indicate that for quaternary normal adamantine structure compounds of general composition A_2BCX_4, only four particular compositions are possible:

$$I_2\text{-}II\text{-}IV\text{-}VI_4,\ I\text{-}II_2\text{-}III\text{-}VI_4,\ I\text{-}III\text{-}IV_2\text{-}V_4,\ II\text{-}III_2\text{-}IV\text{-}V_4.$$

These compounds can be regarded as super-lattice formations in solid solutions of the ternary compound A_2CX_3 plus BX, or ternary compound BCX_2 plus $A_2X_2(2AX)$. For the general composition

$A_4BC_2X_7$, only four particular compositions are possible:

I_4-II-IV_2-VI_7, II_4-IV-I_2-VI_7, III_4-I-IV_2-V_7, IV_4-I-II_2-V_7 .

Only two of these compounds have been synthesized (Sec. 2.4.4).

For the general composition $A_2BC_5X_8$, only four particular compositions are possible:

I_2-II-IV_5-V_8, III_2-V-I_5-VI_8, IV_2-III-I_5-VI_8, IV_2-I-III_5-V_8.

And for the general composition A_3BCX_5 there are also four possible particular compositions:

I_3-III-IV-VI_5, II_3-I-III-VI_5, III_3-II-IV-V_5, IV_3-I-II-V_5.

The last 8 group of compounds has not been yet synthesized.

Some of the compounds of the general composition A_2BCX_4, (I_2-II-IV-VI_4 and I-II_2-III-VI_4) have been studied in 1934 by Brockway (7), in 1965 by Hahn and Schulze (8), in 1967 by Nitsche, Sargent and Wild (9), in 1969 by E.Parthe, K.Yvon and Deitch (10), in 1974 by W.Schäfer and R.Nitsche (11). All of these papers reported crystal structure and x-ray powder analysis. In 1972, U.Ganiel, E.Hermon and S.Shtrikman (12) studied magnetic ordering in Cu_2FeSnS_4 by Mössbauer spectroscopy. In 1980 L.Gueen and W.S.Glaunsinger (13) reported, electrical, magnetic and EPR studies in Cu_2BCX_4 (B=II, C=IV, X=S or Se). In 1977, L.K.Samanta and G.C.Bhar (14) calculated nonlinearity (Millers Δ) and average refractive index for some stannite crystals. In 1977, Donald, M.S. and Aaron Wold (15) reported, electrical and optical characterization on four compounds: Cu_2ZnSiS_4, $Cu_2ZnSiSe_4$, Cu_2ZnGeS_4, $Cu_2ZnGeSe_4$. It is interesting to point out that these are the only optical measurements that have been done on these compounds. With the exception of these four compounds all of the energy gaps remained unknown until now.

The crystal structure of these compounds, can be divided into three types, differing in symmetry and unit cell. 1. The stannite structure (tetragonal superstructure of sphalerite with $a_{tetr} \approx a_{sph}$,

$c_{tetr} \approx 2a_{sph}$). 2. An orthorhombic or wurzite ($a_{or} \approx 2a_w$, $b_{or} \approx \sqrt{3}a_w$, $c_{or} \approx c_w$). 3. A hitherto unknown structure type based on slightly distorted sphalerite-sized cells of tetragonal, orthohombic or monoclinic symmetry.

2.4.1 Quaternary compounds of the type stannite related to sphalerite.

The compounds Cu_2FeSnS_4, Cu_2FeGeS_4 and Ag_2SnFeS_4 are known as the minerals stannite, briartite and hocartite, respectively. They are a very good example of a quaternary normal adamantine structure compounds. The atomic arrangement of Cu_2FeSnS_4 is shown in Fig. 2.2, space group $I\bar{4}2m$ (D''_{2d}) and point positions are:

Cu_2FeSnS_4 - $I\bar{4}2m$			
Atoms	x	y	z
2Fe in (2a)	0	0	0
2Sn in (2b)	0	0	$\frac{1}{2}$
4Cu in (4d) $0,\frac{1}{2},\frac{1}{4};\frac{1}{2},0,\frac{1}{4}$	$0,\frac{1}{2}$	$\frac{1}{2},0$	$\frac{1}{4},\frac{1}{4}$
8S in (8i) $x,x,z;\bar{x},\bar{x},z;x,\bar{x},\bar{z};\bar{x},x,\bar{z}$	$\frac{1}{4}$		$\frac{1}{4}$

This structure consists of alternating cation layers of mixed B and C atoms, which are separated by layers of Cu atoms. The unit cell is tetragonal with $c/a \approx 2$. Every sulphur atom is surrounded by 1Sn, 1Fe and 2Cu. This ordering leads to tetragonal supercells, with $a_{stan} \approx a_{zbl}$ and $c_{stann} \approx 2a_{zbl}$.

The compounds isotype with stannite are listed in table 2.1, with their lattice parameters.

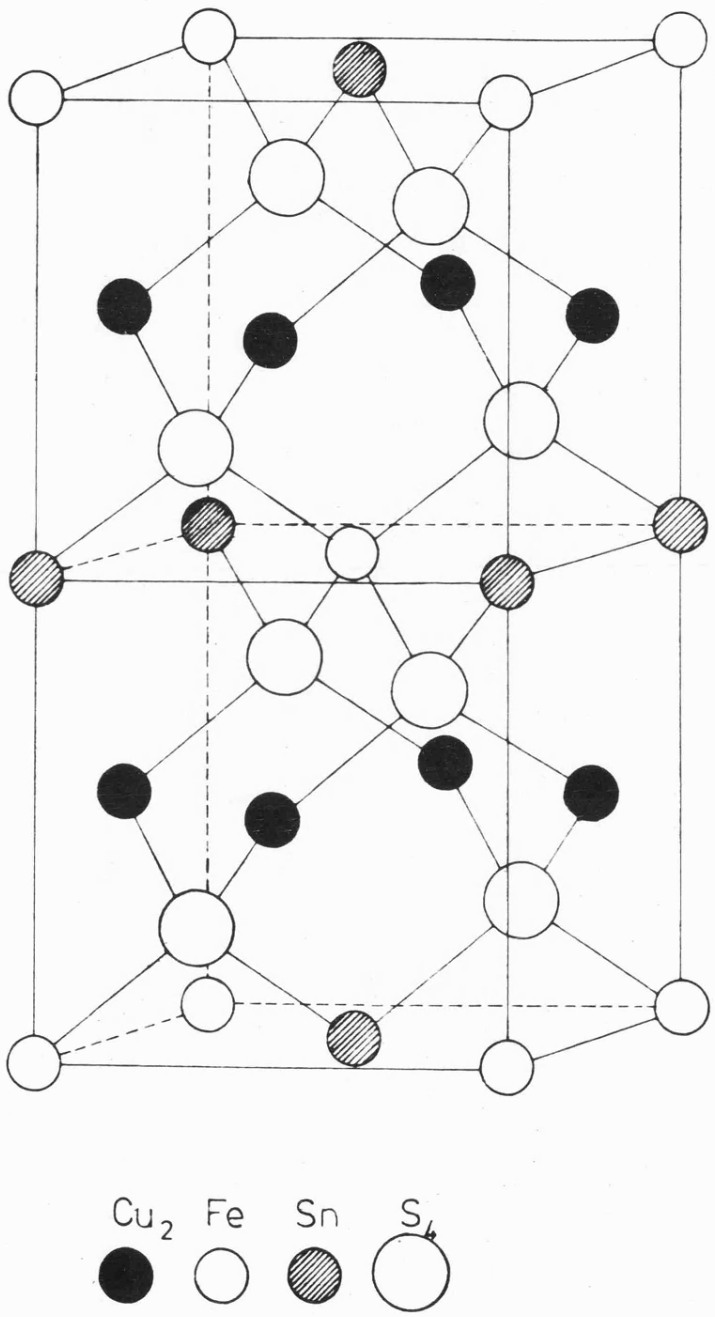

Fig. 2.2 Stannite structure (e.g. Cu_2FeSnS_4), $I\bar{4}2m$

2.4.2 Quaternary compounds of the type related to wurzite

There are two wurtzite related quaternary superstructure types: the orthorhombic Cu_2CdGeS_4 and the monoclinic Na_2ZnSiO_4 type. Type Cu_2CdGeS_4 is an orthorhombic superstructure of wurzite with cell dimensions: $a_{or} \approx 2a_w$, $b_{or} \approx \sqrt{3}a_w$, $c_{or} \approx c_w$. In analogy to Stannite it shall be called wurtz-stannite (wst) hereafter. Wurtz-stannite is also acentric (space group $Pmn2_1$) and the unit cell is derived by doubling an orthohexagonal wurtzite-cell in the a-direction. The metal coordination around each sulphur atom is the same as in stannite. The atomic arrangement is shown in Fig. 2.3, and point positions are:

Cu_2CdGeS_4 - $Pmn2_1$ (C_{2v}^7)			
Atoms	x	y	z
4Cu in 4(b)	$\frac{1}{4}$	$\frac{1}{3}$	0
2Cd in 2(a)		$\frac{5}{6}$	0
2Ge in 2(a)		$\frac{1}{6}$	$\frac{1}{2}$
4S(1) in 4(b)	$\frac{1}{4}$	$\frac{1}{3}$	$\frac{3}{8}$
2S(2) in 2(a)		$\frac{5}{6}$	$\frac{3}{8}$
2S(3) in 2(a)		$\frac{1}{6}$	$\frac{7}{8}$

Type Na_2ZnSiO_4, the unit cell of Na_2ZnSiO_4 is a monoclinic superstructure of wurzite with the same ratio of parameters that of the unit cell of Cu_2CdGeS_4. The space group of this structure is $Pn(C_s^2)$ and the representation of the unit cell is pseudo-orthorhombic.

The atomic arrangement is shown in Fig. 2.4 and point positions are:

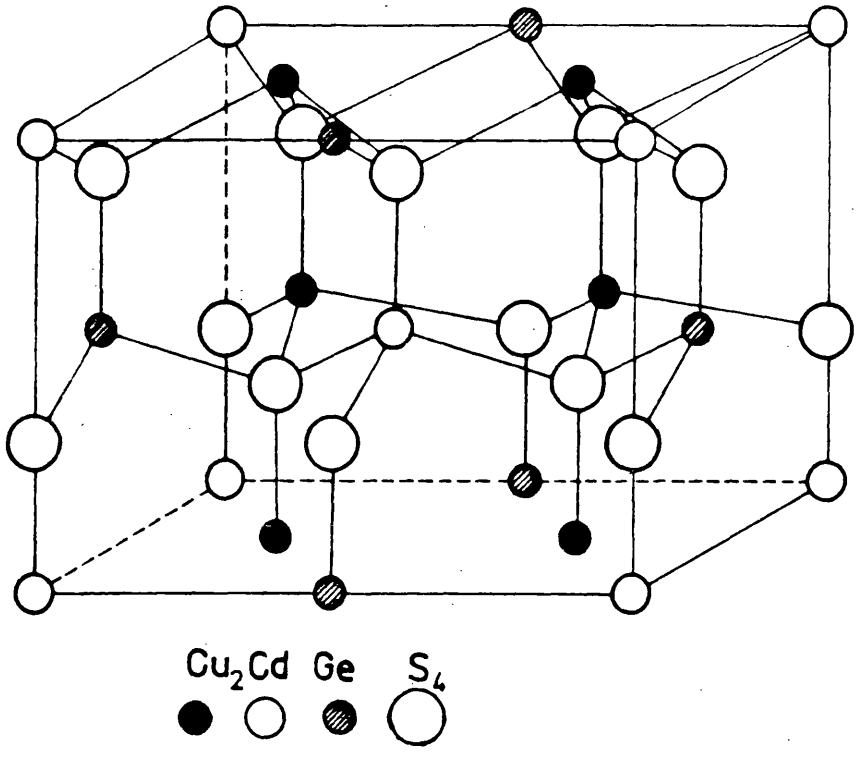

Fig. 2.3 Structure of Cu_2CdGeS_4

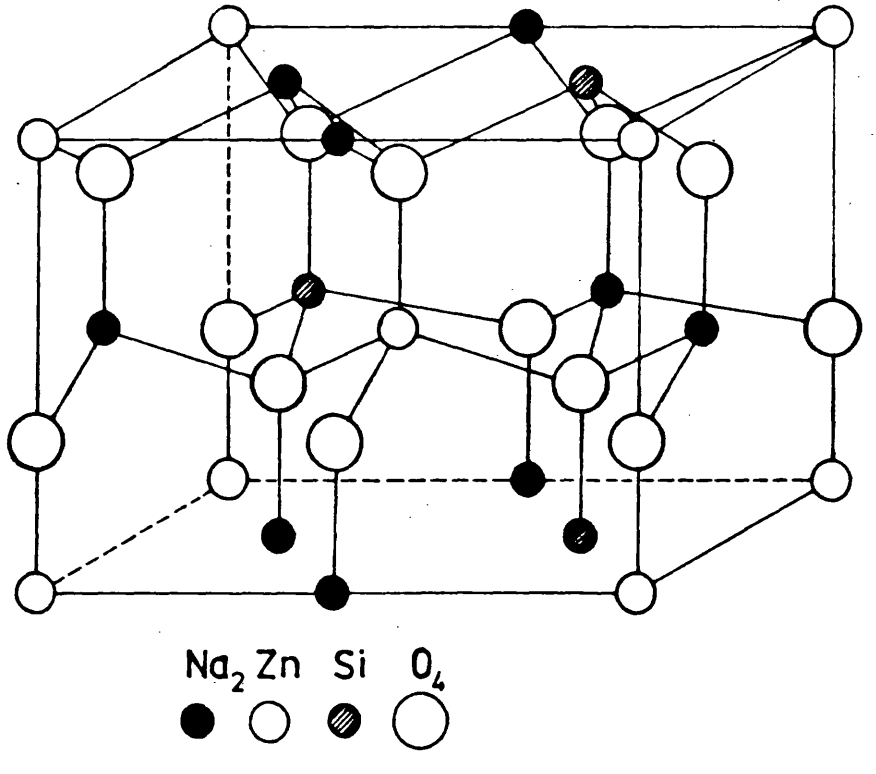

Fig. 2.4 Structure of Na_2ZnSiO_4

Na_2ZnZiO_4 - $Pn(C_5^2)$			
Atoms	x	y	z
2Na(1)	$\frac{3}{4}$	$\frac{2}{3}$	0
2Na(2)	$\frac{1}{2}$	$\frac{1}{6}$	0
2Zn	0	$\frac{1}{6}$	0
2Si	$\frac{1}{4}$	$\frac{2}{3}$	0
2O(1)	$\frac{3}{4}$	$\frac{2}{3}$	$\frac{3}{8}$
2O(2)	$\frac{1}{2}$	$\frac{1}{6}$	$\frac{3}{8}$
2O(3)	0	$\frac{1}{6}$	$\frac{3}{8}$
2O(4)	$\frac{1}{4}$	$\frac{2}{3}$	$\frac{3}{8}$

The compounds isotype to wurtz-stannite are listed in the Table (2.1)

2.4.3 Quaternary compounds of the type related to sphalerite deformation (s_{ph} - def)

Schäfer and Nitsche have reported (11) the absence of superstructure lines in conjunction with a deformation of the sphalerite cell in many of the Ni and Co containing quaternaries therefore indicates the occurrence of a third structure type, denoted Sph-def. It is assumed to consist of an ordered distribution of the four metal ions (Cu + Cu + II + IV) on the four metal sites of a sphalerite cell. The concurrent loss of symmetry leads to slight deformation but not (as in St and Wurtz-stan.) to a doubling of the cell.

It can be shown that alternative stacking of Cu_2 - II - IV metal nets (with the same atomic arrangement as in the corresponding metal nets of the Wurtz-stannite structure) and close-packed sulphur nets in the cubic sequence A-B-C leads to a structure of space group $P\bar{4}2m$. This structure has a (pseudo-cubic) tetragonal cell containing one formula unit Cu_2-II-IV-S_4, i.e. the same number of metal and sulphur atoms as the Sph-cell. The arrangement of the four metals

around the sulphur atoms is identical to that of Stn. and wurtz-stan. The compound $Cu_2NiGeSe_4$ could belong to this tetragonal version of the Sph-def type. Stronger deformations leading to orthorhombic or even monoclinic symmetries seem possible. (Cu_2NiGeS_4 and Cu_2NiSiS_4 Sph-def therefore denotes a variety of structures (all having cells of Sph-dimensions but of different symmetries) rather than a special structure type.

The x-ray analysis of Cu_2NiSnS_4, Cu_2NiSnS_4 and $Cu_2CoSnSe_4$ showed only the simple Sph. pattern without line splitting or superstructure reflections. Here it could be possible to postulate a purely statistical distribution of the four metals in a Sph-lattice. However, it is equally probable to assume an ordered distribution with a pseudocubic cell of the above-mentioned tetragonal space group $P\bar{4}2m$ having a c/a ratio so close to one that line splitting is not observable. This assumption is plausible in view of the fact that the tin containing quaternaries which crystallize in the stannite structure have also c/a values closely approaching the ideal value (in this case 2).

2.4.4 Crystal structure of the quaternary $Cu_4NiSi_2S_7$

W.Schäfer, et al reported the crystal structure and magnetic properties of this compound (23) and synthesized the isotypic $Cu_4NiGe_2S_7$. The structure of $Cu_4NiSi_2S_7$ can be described as slightly distorted, cubic close-packed sulphur sublattice in which one half of the tetrahedral voids are occupied in an ordered manner by Cu, Ni and Si. The structure is non-centro-symmetry and space group C2. The maximum deviation from the ideal tetrahedral angle is only 7.7^{o}. It is interesting to note that contrary to most sulphides the Ni atoms in the structure are tetrahedrally coordinated by s atoms. Fig 2.5 is a drawing of the contents of unit cell.

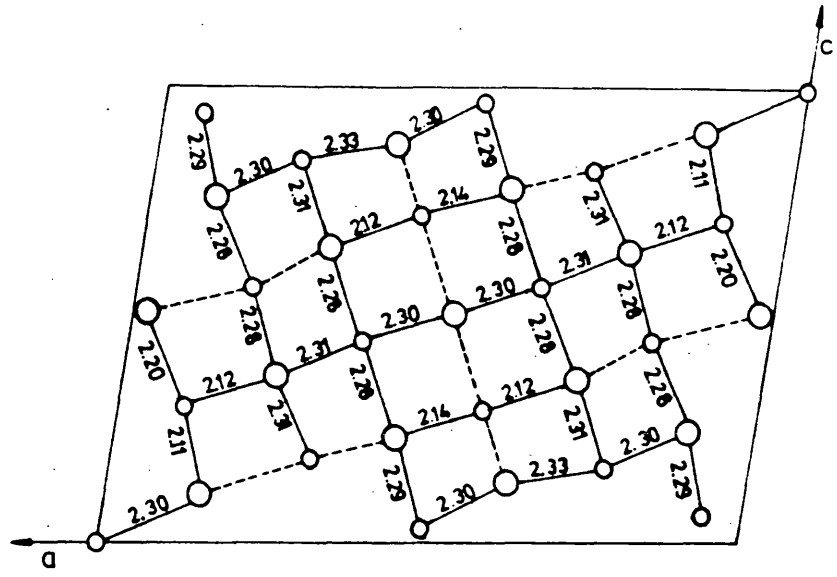

Fig. 2.5 Unit cell and bond lengths in $Cu_7NiSi_2S_7$ (Ref.23)

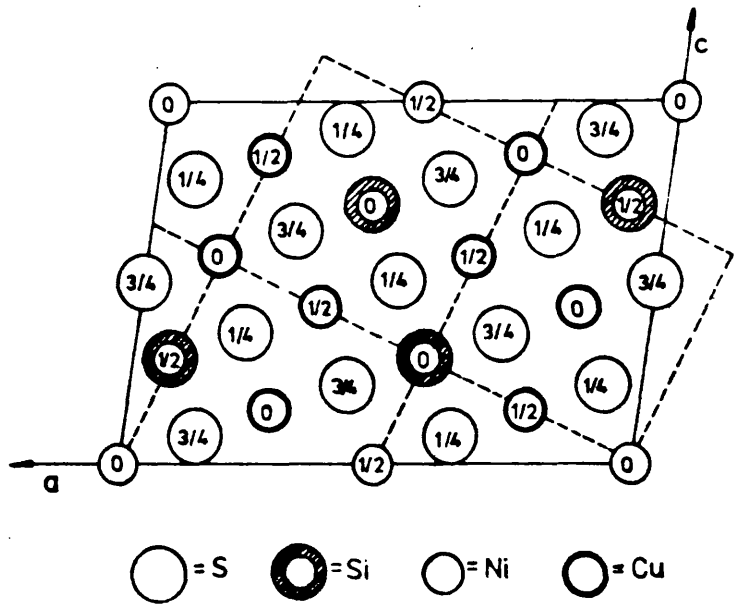

Fig. 2.6 Idealized projection of unit cell of Cu_7NiSiS_7 and relation to sphalerite cell (dotted lines). Number indicates heights of atoms above a-c plane. (Ref. 23)

Fig. 2.6 is an idealized projection along [0 1 0] and shows the relation between the monoclinic superlattice and a sphalerite cell. The approximate dimensional relations are : $a = 5\sqrt{a_{sph}}$; $b = a_{sph}$; $c = \sqrt{5/2}\ a_{sph}$; $\beta = \tan^{-1}3 + \tan^{-1}0.5 = 98.13^{o}$, $V = (7/2)\ V_{sph}$. The lattice parameters are given in table 2.1. The positional parameters are:

$Cu_2NiSi_2S_7$ - C2			
Atoms	x	y	z
Cu(1)	.1409	.0190	.4360
Cu(2)	.2100	.5060	.1395
Ni	0	0	0
Si	.4255	.9950	.2843
S(1)		.7210	.5
S(2)	.0627	.2630	.2174
S(3)	.2861	.7760	.3497
S(4)	.3630	.2430	.0893

We call this structure Sph-def-mono. in the Table 2.1. $Cu_4NiSi_2S_7$ becomes antiferromagnetic at low temperatures.

2.5 Quaternary defect adamantine structure compounds

We have seen in section (2.2) that the rules for adamantine family permit extend this family to a group of structures which are called "defect adamantine structures". We recognize defect adamantine structures as those with vacant coordination sites. The arrangement of the vacancies and with it, of the atoms, in the structure cannot be predicted.

There are the following possible groups of quaternary defect compounds:

Type	Group of quaternary defect compounds
$ABC\square X_4$	$I\text{-}II\text{-}V\text{-}\square\text{-}VI_4$, $I\text{-}III\text{-}IV\text{-}\square\text{-}VI_4$
$A_3BC_2\square_2X_8$	$I_3\text{-}III\text{-}V_2\text{-}\square_2\text{-}VI_8$, $II_3\text{-}IV\text{-}III_2\text{-}\square_2\text{-}VI_8$, $I_3\text{-}V\text{-}IV_2\text{-}\square_2\text{-}VI_8$
$AB_2\square X_3Y$	$I\text{-}III_2\text{-}\square\text{-}VI_3\text{-}VII$
$A_2B_3\square_2XY_6$	$I_2\text{-}II_3\text{-}\square_2\text{-}VI\text{-}VII_6$
$A_2B_2\square XY_4$	$I_2\text{-}II_2\text{-}\square\text{-}VI\text{-}VII_4$
$A_2B_2C_2\square_2X_8$	$I_2\text{-}III_2\text{-}IV_2\text{-}\square_2\text{-}VI_8$
$A_2B_2C\square_2X_8$	$I_2\text{-}IV_2\text{-}V\text{-}\square_2\text{-}VI_8$
$AB_3C_3\square X_8$	$I\text{-}II_3\text{-}III_3\text{-}\square\text{-}VI_8$

The structure data of the quaternary defect compounds synthesized up to the present are listed in table 2.2. The crystal structure of these compounds can be divided into four types, differing in symmetry and unit cell. 1. Partially ordered chalcopyrite structure. 2. The cubic structure type $HgGa_2Te_4$. 3. The phenacite structure (hexagonal). This structure is tetrahedral but non-adamantine and that is the reason it has not been included in the table 2.4), and the spinel structure. In this ideal structure the anions form a cubic close packing, in which the cations partly occupy the tetrahedral and octahedral interstices. The unit cell contains 32 anions forming 64 tetrahedral interstices and 32 octahedral interstices; of these 8 tetrahedral and 16 octahedral interstices are occupied by cations. Also this structure is non-adamantine and it has not been included in table 2.2. In the following sections of this chapter, we will discuss the quaternary defect adamantine compounds only.

2.5.1 Quaternary defect adamantine compounds of the type $I\text{-}III\text{-}IV\text{-}\square\text{-}VI_4$

Hahn and Strick (23) carried out an initial investigation of a number of the copper compounds of this type, determining lattice parameter values and showing that the compounds are tetragonal, but they did not establish the ordering condition in the compounds. Further preliminary work on both the copper and silver compounds has been reported by Pamplin et al (24,25). The present thesis reports an investigation of the properties of copper compounds together with the corresponding silver compounds including crystal structure, crystal growth, differential thermal analysis, optical properties of these compounds and lattice parameters of $CuGaSn\square Se_4$ as functions of temperature.

The Selenide compounds and three of sulphide compounds have the partially ordered chalcopyrite structure, as the related ternaries ($I\text{-}III\text{-}VI_2$). In the ternaries we have two metal atom sub-lattices each uniformly populated with atoms from groups I and III respectively. In the quaternaries the same two sub-lattices occur. One sub-lattice is populated randomly with equal number of atoms from two different groups while the other sub-lattice is populated randomly with equal numbers of vacancies and atoms from the third group. The group VI atoms occupy the same positions in both types of compounds. $AgGaGeS_4$ has a hitherto unknown structure type with orthorhombic symmetry. The atomic arrangement of $CuGaSn\square Se_4$ (see chapter III) is shown in Fig.2.7 space group $I\bar{4}2d$ and point positions are:

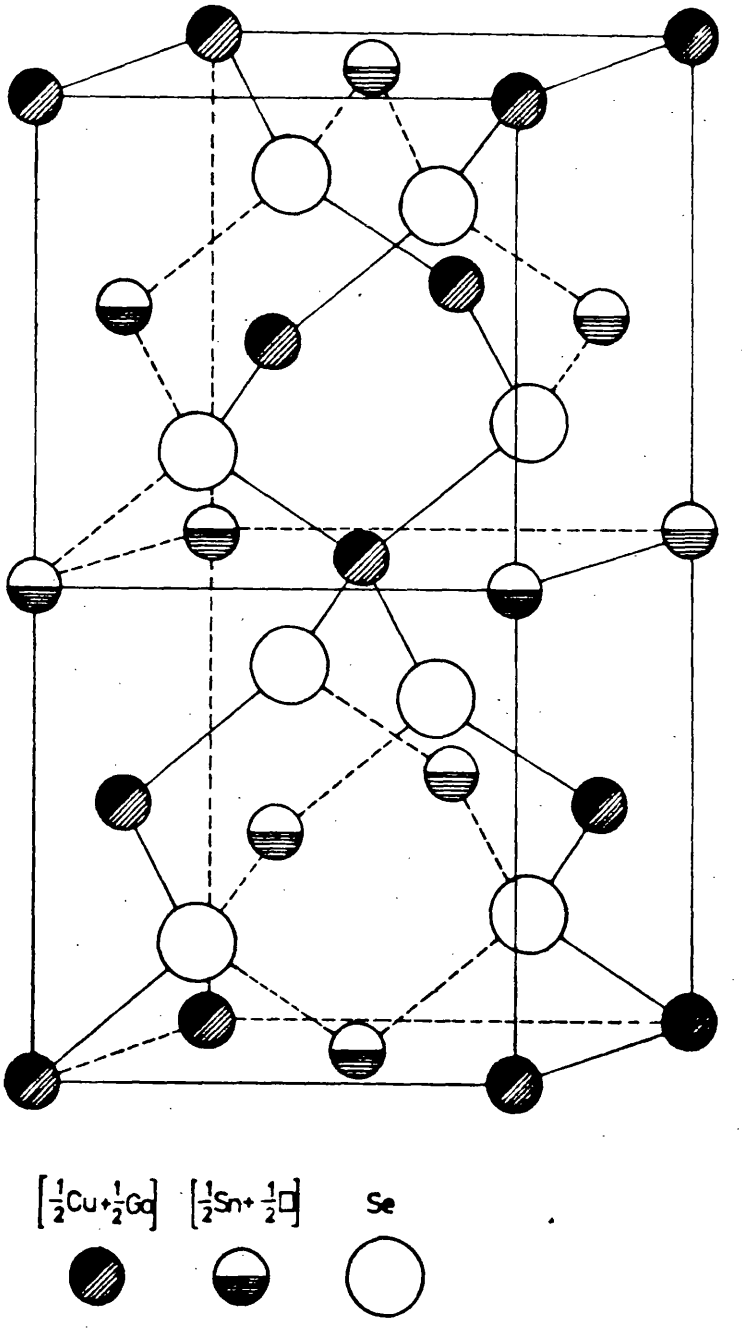

Fig. 2.7. Structure of $CuGaSn\square Se_4$

$CuGaSn\square Se_4$ - $I\bar{4}2d$	
Atoms	Coordinates
Cu and Ga statistically distributed in (a)	$0,0,0;0,\frac{1}{2},\frac{1}{4};\frac{1}{2},\frac{1}{2},\frac{1}{2};\frac{1}{2},0,\frac{3}{4}$
Sn and □ statistically distributed in (b)	$0,0,\frac{1}{2};0,\frac{1}{2},\frac{3}{4};\frac{1}{2},\frac{1}{2},0;\frac{1}{2},0,\frac{1}{4}$
Se in (d) with x=0.25708	$x,\frac{1}{4},\frac{1}{8};\bar{x},\frac{3}{4},\frac{1}{8};\frac{3}{4},x,\frac{7}{8};\frac{1}{4},\bar{x},\frac{7}{8}$

The structure data of these compounds and other quaternary compounds with defect adamantine structures are listed in Table 2.2

2.5.2 Quaternary defect adamantine compounds of the type $I\text{-}III_2\text{-}\square\text{-}VI_3\text{-}VII$

Only three compounds of this group have been synthesized up till now ($CuIn_2\square Se_3Br$, $CuIn_2\square Se_3I$, $AgIn_2\square Se_3I$). The structure is related to sphalerite. The structure is cubic $HgGa_2\ Te_4$ type. Space group $F\bar{4}3m$.

2.6 Conclusions

The quaternary adamantine compounds with their structure and lattice parameters are listed in the table. These tables in the future should be enlarged with hundreds of new compounds, but the most important work to be done in evaluating these compounds is, to study their physical properties (optical, electrical properties, etc)., because on these properties depends the potential future application in semiconductor devices.

The relationships between the various adamantine structures are shown in Fig. 2.8.

Fig. 2.8. THE ADAMANTINE FAMILY OF CRYSTAL STRUCTURES

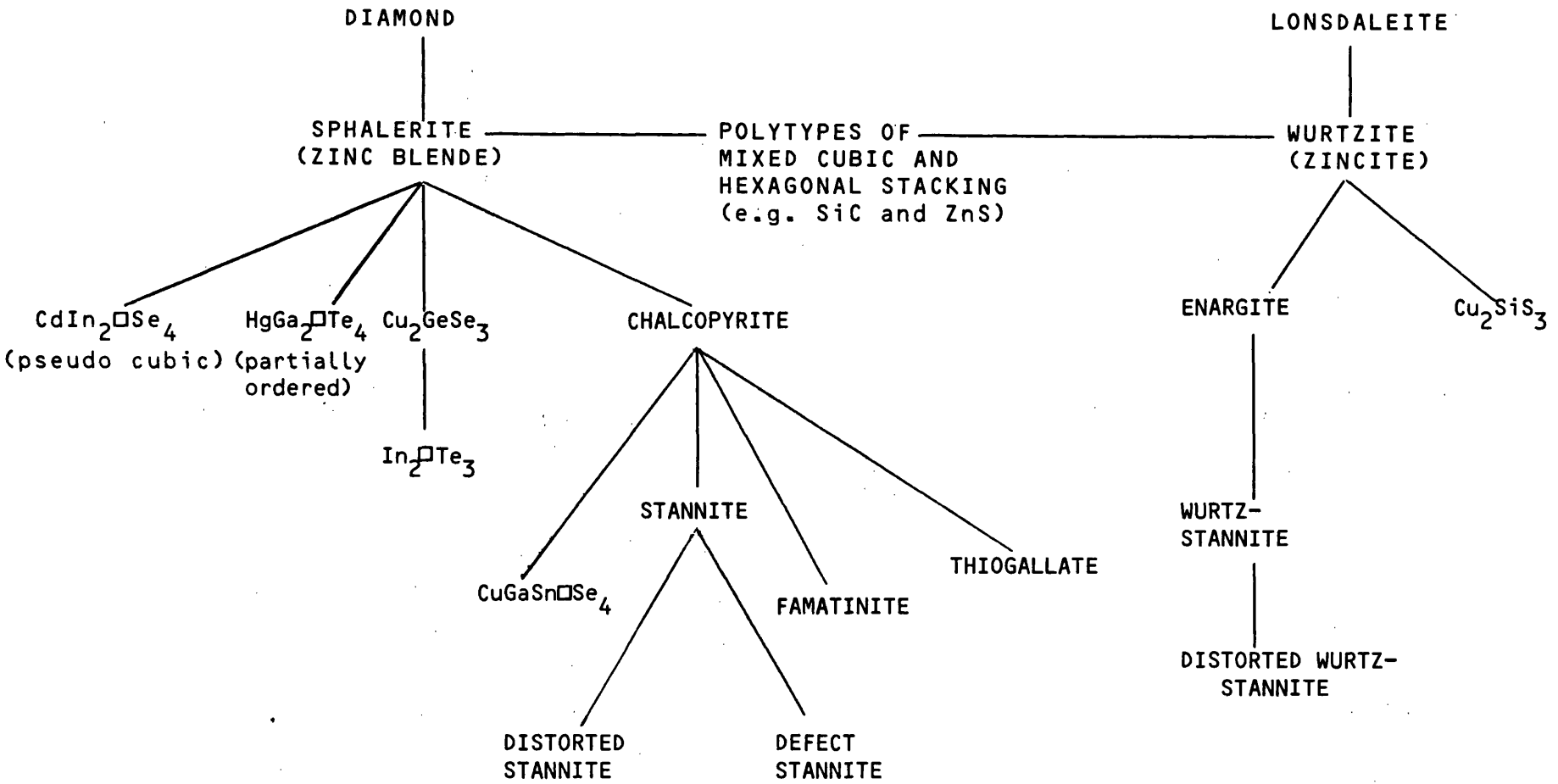

TABLE 2.1. QUATERNARY NORMAL ADAMANTINE COMPOUNDS

FORMULA	STRUCTURE	SPACE GROUP	LATTICE PARAMETERS a(Å)	b(Å)	c(Å)	c/A	β°	REF.
I_2 - II - IV - VI_4								
Cu_2FeSnS_4	Stannite	$I\bar{4}2m$	5.460		10.725	1.964		7
$Cu_2FeSnSe_4$	Stannite	$I\bar{4}2m$	5.664		11.330	2.000		8
Cu_2FeGeS_4	Stannite	$I\bar{4}2m$	5.330		10.528	1.975		9
$Cu_2FeGeSe_4$	Stannite	$I\bar{4}2m$	5.590		11.072	1.981		5,11
Cu_2FeSiS_4	Wurtz-stannite	$Pmn2_1$	7.404	6.411	6.140			9
$Cu_2FeSiSe_4$	Stannite	$I\bar{4}2m$	5.549		10.951	1.974		11
Cu_2MnSnS_4	Stannite	$I\bar{4}2m$	5.490		10.720	1.953		16
$Cu_2MnSnSe_4$	Stannite	$I\bar{4}2m$	5.744		11.423	1.989		11
Cu_2MnGeS_4	Wurtz-stannite	$Pmn2_1$	7.608	6.511	6.236			9
$Cu_2MnGeSe_4$	Wurtz-stannite	$Pmn2_1$	7.979	6.865	6.557			11
Cu_2MnSiS_4	Wurtz-stannite	$Pmn2_1$	7.533	6.435	5.179			11
$Cu_2MnSiSe_4$	Wurtz-stannite	$Pmn2_1$	7.912	6.774	6.501			11

CONTINUATION 1/

FORMULA	STRUCTURE	SPACE GROUP	LATTICE PARAMETERS a(Å)	b(Å)	c(Å)	c/A	β°	REF.
			$I_2 - II - IV - VI_4$					
Cu_2NiSnS_4	Sphalerite or pseudocubic	$P\bar{4}2m$?	5.425					11
Cu_2NiSnS_4	Sphal or pseudocubic	$P\bar{4}2m$?	5.705					11
Cu_2NiGeS_4	Sphal - def		5.332	5.263	5.227			9, 11
$Cu_2NiGeSe_4$	Sphal - def		5.581		5.500			5, 11
Cu_2NiSiS_4	Sphal - def		5.143	5.311	5.179			11
$Cu_2NiGeSe_4$?			Synthesis so far unsuccessfyl (may be it is necessary high pressure)					5, 11
Cu_2CoSnS_4	Stannite	$I\bar{4}2m$	5.402		10.805	2.000		11
Cu_2CoSnS_4	Sphal. or pseudocubic	$P\bar{4}2m$?	5.697					11
$Cu_2CoGeSe_4$	Stannite	$I\bar{4}2m$	5.300		10.480	1.977		16
Cu_2CoSiS_4	Sphal - def		5.601	5.561	5.500			11
Cu_2CoSiS_4	Stannite	$I\bar{4}2m$	5.270		10.327	1.960		11
$Cu_2CoSiSe_4$?			Synthesis so far unsuccessful					11

CONTINUATION 2/

FORMULA	STRUCTURE	SPACE GROUP	LATTICE PARAMETERS a(Å)	b(Å)	c(Å)	c/A	β°	REF.
$I_2 - II - IV - VI_4$								
Cu_2ZnSnS_4	Stannite	$I\bar{4}2m$	5.427		10.848	1.999		9,11
$Cu_2ZnSnSe_4$	Stannite	$I\bar{4}2m$	5.681		11.340	1.996		8
Cu_2ZnGeS_4	Wurtz-stannite	$Pmn2_1$	7.504	6.474	6.185			9,11
$Cu_2Z_nGeSe_4$	Stannite	$I\bar{4}2m$	5.622		11.060	1.967		8
Cu_2ZnSiS_4	Wurtz-stannite	$Pmn2_1$	7.435	6.396	6.135			9,11
$Cu_2ZnSiSe_4$	Wurtz-stannite	$Pmn2_1$	7.823	6.720	6.440			9,11
Cu_2CdSnS_4	Stannite	$I\bar{4}2m$	5.586		10.834	1.939		9,11
$Cu_2CdSnSe_4$	Stannite	$I\bar{4}2m$	5.814		11.470	1.973		8
Cu_2CdGeS_4	Wurtz-stannite	$Pmn2_1$	7.692	6.555	6.299			10
$Cu_2CdGeSe_4$	Stannite	$I\bar{4}2m$	5.657		10.988	1.942		10
Cu_2CdSiS_4	Wurtz-stannite	$Pmn2_1$	7.614	6.489	6.254			9,11
$Cu_2CdSiSe_4$	Wurtz-stannite	$Pmn2_1$	7.990	6.824	6.564			11

CONTINUATION 3/

FORMULA	STRUCTURE	SPACE GROUP	LATTICE PARAMETERS a(Å)	b(Å)	c(Å)	c/A	β°	REF.
I_2 - II - IV - VI_4								
Cu_2HgSnS_4	Stannite	$I\bar{4}2m$	5.566		10.880	1.955		8
$Cu_2HgSnSe_4$	Stannite	$I\bar{4}2m$	5.818		11.480	1.973		8
Cu_2HgGeS_4	Stannite	$I\bar{4}2m$	5.490		10.550	1.922		11
$Cu_2HgGeSe_4$	Stannite	$I\bar{4}2m$	5.694		11.020	1.935		8
Cu_2HgSiS_4	Wurtz-stannite	$Pmn2_1$	7.592	6.484	6.269			11
Cu_2HgSiS_4	Wurtz-stannite	$Pmn2_1$	7.962	6.823	6.569			11
Ag_2FeSnS_4	Stannite	$I\bar{4}2m$	5.740		10.909	1.901		17
$Ag_2ZnGeSe_4$	Sphal. related structure	$P\bar{4}m2$	4.269		5.659	1.326		10
Ag_2CdSnS_4	Wurt.related struc.	$Cmc2_1$	4.111	7.038	6.685			10
$Ag_2CdSnSe_4$	Wurt.related struc.	$Cmc2_1$	4.262	7.314	6.979			10
Ag_2CdGeS_4	Wurt.related struc.	$Pmn2_1$	8.044	6.849	6.593			10

CONTINUATION 4/

FORMULA	STRUCTURE	SPACE GROUP	LATTICE PARAMETERS a(Å)	b(Å)	c(Å)	c/A	β°	REF.
		I_2 - II - IV - VI_4						
Li_2FeGeO_4	Wurtz-stannite	$Pmn2_1$	6.410	5.440	5.010			18
Li_2FeSiO_4	Wurtz-stannite	$Pmn2_1$	6.260	5.320	5.010			18
Li_2MnGeO_4	Wurtz-stannite	$Pmn2_1$	6.450	5.480	5.050			18
Li_2MnSiO_4?								18
Li_2CoGeO_4	Wurtz-stannite	$Pmn2_1$	6.370	5.460	5.010			18
Li_2CoSiO_4	Wurtz-stannite	$Pmn2_1$	6.170	5.360	4.930			18
Li_2MgGeO_4	Wurtz-stannite	$Pmn2_1$	6.390	5.480	4.990			18
Li_2MgSiO_4?								18
Li_2ZnGeO_4	Wurtz-stannite	$Pmn2_1$	6.360	5.430	5.020			18
Li_2ZnSiO_4	Wurtz-stannite	$Pmn2_1$	6.130	5.370	4.940			18
Li_2CdGeO_4	Wurtz-stannite	$Pmn2_1$	6.640	5.470	5.130			18
Li_2CdSiO_4	Wurtz-stannite	$Pmn2_1$	6.470	5.350	5.100			18
Na_2MgGeO_4	Wurtz-stannite p.o.	Pn	7.150	5.600	5.350		90°	19
Na_2ZnGeO_4	Wurtz-stannite p.o.	Pn	7.170	5.560	5.320		90°	19
Na_2ZnSiO_4	Wurtz-stannite orthor	Pn	7.020	5.440	5.330		90°20'	19
	Wurtz-stan. p.o.	Pn	7.020	5.480	5.320		90°	1

CONTINUATION 5/

FORMULA	STRUCTURE	SPACE GROUP	LATTICE PARAMETERS a(Å)	b(Å)	c(Å)	c/A	β°	REF.
			$I - II_2 - III - VI_4$					
$CuZn_2AlSe_4$	Sphal-disorder	$F\bar{4}3m$	5.624					10
$CuZn_2AlTe_4$	Sphal-disorder	$F\bar{4}3m$	6.043					10
$CuZn_2GaS_4$?								20
$CuZn_2GaSe_4$	Sphal-disorder	$F\bar{4}3m$	5.653(5.642)					10,21
$CuZn_2GaTe_4$	Sphal-disorder	$F\bar{4}3m$	6.057					10,21
$CuZn_2InS_4$	Sphal-disorder	$F\bar{4}3m$	5.475					10
$CuZn_2InSe_4$	Sphal-disorder	$F\bar{4}3m$	5.733(5.720)					10,21
$CuZn_2InTe_4$	Sphal-disorder	$F\bar{4}3m$	6.153(6.130)					10,21
$CuCd_2AlSe_4$	Wurtz-disorder	$P6_3mc$	4.106		6.752			10
$CuCd_2InS_4$	Wurtz-disorder	$P6_3mc$	4.047		6.617			10
$CuCd_2InSe_4$	Sphal-disorder	$F\bar{4}3m$	5.934(5.936)					10,21
$CuCd_2InTe_4$	Sphal-disorder	$F\bar{4}3m$	6.335(6.372)					10,21
$CuCd_2GaTe_4$	Sphal-disorder	$F\bar{4}3m$	6.250					22
$CuCd_2GaSe_4$	Sphal-disorder	$F\bar{4}3m$	5.830					22

CONTINUATION 6/

FORMULA	STRUCTURE	SPACE GROUP	LATTICE PARAMETERS a(Å)	b(Å)	c(Å)	c/A	β°	REF.
			$I - II_2 - III - VI_4$					
$AgZn_2AlS_4$	Wurtz-disorder	$P6_3mc$	3.846		6.313			10
$AgZn_2InS_4$	Wurtz-disorder	$P6_3mc$	3.944		6.459			10
$AgZn_2InTe_4$	Sphal-disorder	$F\bar{4}3m$	6.253					10
$AgZn_2GaS_4$?								20
$AgCd_2AlS_4$	Wurtz-disorder	$P6_3mc$	4.134		6.723			10
$AgCd_2GaSe_4$	Wurtz-disorder	$P6_3mc$	4.251		6.956			10
$AgCd_2GaTe_4$	Sphal-disorder	$F\bar{4}3m$	6.375					10
$AgCd_2InS_4$	Wurtz-disorder	$P6_3mc$	4.112		6.709			10
$AgCd_2InSe_4$	Wurtz-disorder	$P6_3mc$	4.277		6.988			10
$AgCd_2InTe_4$	Sphal-disorder	$F\bar{4}3m$	6.438(6.457)					10,21
			$I_4 - II - IV_2 - VI_7$					
$Cu_4NiSi_2S_7$	Sphal-def-mon	C2	11.551	5.313	8.165		98.72	23
$Cu_4NiGe_2S_7$	Sphal-def-mon	C2	11.703	5.333	8.311		98.37	23

TABLE 2.2 QUATERNARY DEFECT ADAMANTINE COMPOUNDS

FORMULA	STRUCTURE	SPACE GROUP	LATTICE PARAMETERS a(Å)	b(A)	c(A)	C/A	β°	REF.
I - III - IV-□- VI_4								
$CuBGe\square S_4$	Type thiogallate quad.		5.343		5.217	0.976		24
$CuBGe\square Se_4$	Type thiogallate quad.		5.596		5.476	0.979		24
$CuAlSn\square Se_4$	Part. ord. chalcop.	$I\bar{4}2d$	5.604		10.950	1.954		26
$CuAlSi\square S_4$	Type thiogallate quad.		5.347		10.310	1.928		24
$CuAlSi\square Se_4$	Type thiogallate quad.		5.604		10.860	1.939		24
$CuAlSi\square Te_4$	Type thiogallate quad.		6.014		5.937	0.987		24
$CuAlGe\square S_4$	Type thiogallate quad.		5.320		10.050	1.888		24
$CuAlGe\square Se_4$	Type thiogallate quad.		5.566		5.389	0.968		24
	Part. ord. chalcop.	$I\bar{4}2d$	5.575		10.682	1.916		26
$CuGaSi\square S_4$	Type thiogallate quad.		5.347		5.158	0.965		24
$CuGaSi\square Se_4$	Type thiogallate quad.		5.590		5.380	0.963		24
$CuGaSi\square Te_4$	Type thiogallate quad.		5.995		5.909	0.986		24
$CuGaGe\square S_4$	Type thiogallate quad.		5.334		10.050	1.883		24
	Part.Ord.Chalcop.	$I\bar{4}2d$	5.302		10.212	1.926		27
$CuGaGe\square S_4$	Type thiogallate quad.		5.566		5.389	0.968		24
	Part. Ord. Chalcop.	$I\bar{4}2d$	5.568		10.841	1.947		26

CONTINUATION 1.

Table 2.2

FORMULA	STRUCTURE	SPACE GROUP	LATTICE PARAMETERS a(Å)	b(Å)	c(Å)	c/a	β°	REF.
I - III - IV - □ - VI_4								
$CuGaSn\square Se_4$	Type thiogallate quad.		5.622		5.503	0.979		24
	Part. Ord. Chalcop.	$I\bar{4}2d$	5.611		10.986	1.958		26
$CuGaSn\square S_4$	Part. Ord. Chalcop.	$I\bar{4}2d$	5.358		10.480	1.956		26
$CuInGe\square S_4$	Type thiogallate quad.		5.539		10.040	1.813		24
$CuInGe\square Se_4$	Type thiogallate quad.		5.595		11.070	1.979		24
	Part. Ord. Chalcop	$I\bar{4}2d$	5.640		11.167	1.980		26
$CuInSn\square Se_4$	Type thiogallate quad.		5.670		11.340	2.000		24
	Part. Ord. Chalcop	$I\bar{4}2d$	5.700		11.400	2.000		26
$AgAlSn\square Se_4$	Part. Ord. Chalcop	$I\bar{4}2d$	5.882		10.711	1.821		26
$AgAlGe\square Se_4$	Part. Ord. Chalcop.	$I\bar{4}2d$	5.871		10.304	1.755		26
$AgGaSn\square S_4$	Part. Ord. Chalcop.	$I\bar{4}2d$	5.757		10.616	1.844		27
$AgGaSn\square Se_4$	Part. Ord. Chalcop.	$I\bar{4}2d$	5.869		10.817	1.843		26
$AgGaGe\square Se_4$	Part. Ord. Chalcop.	$I\bar{4}2d$	5.826		10.382	1.782		26
$AgGaGe\square S_4$	Unknown orthorhom.		8.310	5.775	5.950			27
$AgInSn\square Se_4$	Part.Ord. Chalcop.	$I\bar{4}2d$	5.877		11.284	1.920		26
$AgInGe\square Se_4$	Part.Ord. Chalcop.	$I\bar{4}2d$	5.759		10.810	1.877		26

CONTINUATION 2/ Table 2.2

FORMULA	STRUCTURE	SPACE GROUP	LATTICE PARAMETERS a(Å)	b(Å)	c(Å)	c/a	β°	REF.
$I - III_2 - \square - VI_3 - VII$								
$CuIn_2\square Se_3Br$	Type $HgGa_2\square Te_4$ cubic	$F\bar{4}3m$	5.765					28
$CuIn_2\square Se_3I$	Type $HgGa_2\square Te_4$ cubic	$F\bar{4}3m$	5.768					28
$AgIn_2\square Se_3I$	Type $HgGa_2\square Te_4$ cubic	$F\bar{4}3m$	5.893					28

CHAPTER 3

QUATERNARY DEFECT ADAMANTINE COMPOUNDS, SYNTHESIS, GROWTH AND CHARACTERIZATION

3.1 Introduction

A survey of all known quaternary compounds is shown in chapter 2. Table 2.2 gives a list of new quaternary defect adamantine compounds that have been prepared for the first time in this work. The method of synthesis of these compounds is given in this chapter.

The x-ray study was carried out following the Debye-Scherrer procedure, since all the samples were finely crystalline. For all photographs Cu Kα-radiation was used. The relationship between structure and lattice parameters for the quaternary and ternary related compounds are examined. A systematic variation of both $\Delta V = V_t - V_q$ (difference between the ternary and quaternary unit cell volumes) and $\Delta(c/a) = (c/a)_t - (c/a)_q$ was found.

Differential-thermal-analysis (DTA) was used to find the melting point and transition temperatures of some of these compounds (specially the materials we were interested to grow). These parameters are very important because they give some indication of the experimental conditions for growth of these materials. In these DTA curves, the peaks can arise from both physical and chemical changes. The former include melting, boiling and solid-solid structural transitions; sometimes a solid reaction product will form a low melting eutectic with a sample which would not itself have melted. In the latter case, peaks can result not only from reaction of the sample itself, but also from secondary reactions of evolved decomposition products.

A modification of Pendölofen vapour transport is introduced to grow good single crystals of $CuGaSn\square Se_4$, $AgGaSn\square Se_4$, $AgGaGe\square Se_4$ and $CuGaGe\square Se_4$. We have been able to show that for growing single crystals it is particularly advantageous to reverse direction of the temperature gradient periodically instead of keeping it constant, which is the usual practice. This interesting technique introduced for the first time by Scholz (38) proved that it is possible to transport simultaneously three non-volatile metals in the closed tube.

3.2 Tetrahedral composition diagram for quaternary compounds

Ohachi and Pamplin (29) reported that quaternary compounds, in which a group VI chalcogenide element is included, can be discussed with pseudoternary systems of four binary compounds, I_2-VI, II-VI, III_2-VI_3 and IV-VI_2. Fig. 3.1 shows a tetrahedral composition diagram of the possible quaternary compounds. Quaternary compounds are shown on its surfaces and ternary compounds on its edges, quinary compounds could be shown in its inside area.

In this fig. 3.1 we can draw the line of the I-III-VI_2, IV-VI_2 pseudobinary systems. From the systematic study of this pseudobinary systems several interesting new compounds were found of composition I-III-IV-VI_4. Three different structures have been found in these groups of compounds. One is the partially ordered defect chalcopyrite structure, the list of compounds with this structure is given in Table 2.2. Hahn and Strick (24, 30, 31) have earlier prepared 29 of these compounds, 13 of these, particularly chromium compounds, were spinel. Chromium does not occur in adamantine compounds preferring octahedral co-ordination. The other 16 were adamantine and they are discussed in the chapter 2. Ohachi and Pamplin (29) reported that $CuInSnS_4$ and $AgInSnS_4$ were superionic spinel structure $AgGaGeS_4$ has

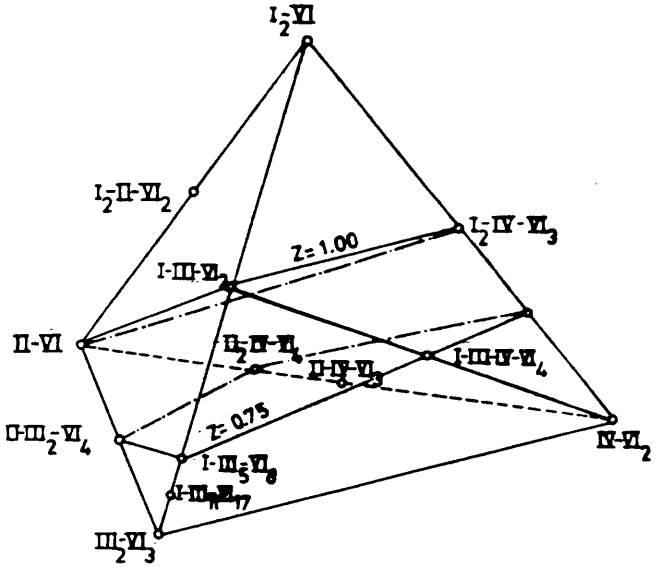

Fig. 3.1 A tetrahedral composition diagram of group VI compounds (Ref. 29).

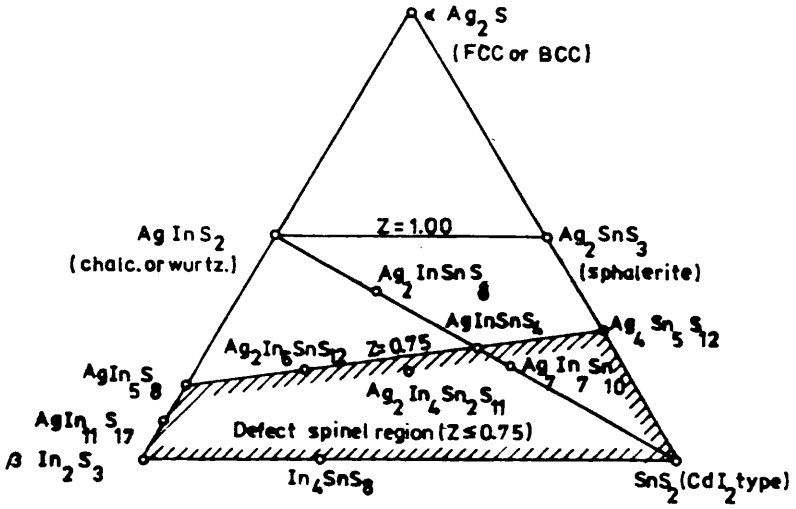

Fig. 3.2 Spinel compounds on the system of Ag_2S - I_2S_3 - SnS_2 (Ref. 29).

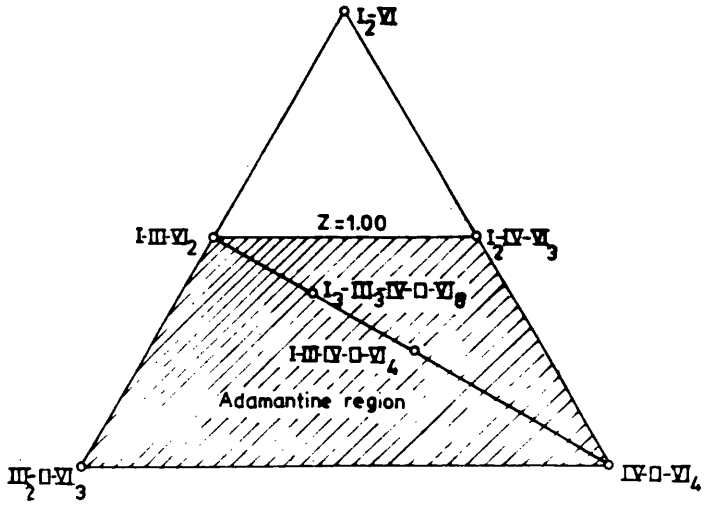

Fig. 3.3 Ternary diagrams showing adamantine regions.

a hitherto unknown structure type, with orthorhombic symmetry (Table 2.2). Many tellurides do not appear to be single phase at this composition (32). Figures 3.2 and 3.3 show two interesting ternary diagrams in which these two different structures were found.

3.3 Preparation of polycrystalline materials

In general, raw materials were of high purity. Copper, silver, gallium, tin, germanium, aluminium, selenium and sulphur were of 99.999% purity. Copper and tin were in the form of wire, sulphur was in irregular chunks, silver, gallium and selenium were in beads or shot. For this work, Ga, S, Se, and Ag were used as received. Copper was etched to remove the oxide coating.

Because of the high vapour pressure of the group VI elements at elevated temperatures, preparation of these compounds is not straightforward and the usual precautions must be taken. Stoichiometric quantities of the raw materials were packed and sealed into quartz ampoules under a vacuum of 10^{-5} torr. Each ampoule was sealed inside a bigger ampoule as a safety precaution against the bursting of a tube.

The sample was heated quite rapidly to 200-400^{o}C and kept at that temperature overnight. Subsequent heating to 1000 - 1100^{o}C was very slow. We used 10^{o}C/hour for the selenides and 2^{o}C/hour for the sulphides. Samples were kept at the high temperature for at least a day. The heating was carried out in a rocking furnace and during the heating up and also during the reaction at high temperatures, the sample was rocked to ensure good mixing of the components. Finally the specimens were cooled slowly to room temperature. The resulting ingot was cut up to provide specimens for powder x-ray photographs and for optical work.

Some specimens on x-ray analysis showed the presence to a greater or lesser extent, of the ternary I-III-VI_2 and IV-VI_2. In some cases however the dichalcoganide was barely discernible and the ternary was undetectable. These samples were powdered, compressed and annealed just below their melting points for two to three weeks. They were then found to be single phase. Samples of all compounds given in table 3.1 were prepared in this way.

The method of reacting from the elements was used for two reasons: (a) purity of the final produce would be higher because, in general, the elements were available in higher purities than were the simple chalcogenides, and (b) it was felt that stoichiometry could be more carefully controlled.

3.4 X-ray analysis

The x-ray study was carried out following the Debye-Scherrer procedure. A Phillips 114.6 mm diameter diffraction camera was used with Straumanis film configuration. Copper K_α radiation was used to irradiate the finely powdered sample.

The distance, d, between planes with Miller indices (h, k, l) for the tetragonal space group, $I\bar{4}2d$, is, given by,

$$\frac{1}{d^2} = \frac{h^2+k^2}{a^2} + \frac{l^2}{d^2} = \frac{4\sin^2\theta}{\lambda^2} \qquad (3.1)$$

In the selenide compounds and three of the sulphur compounds, the structure was found to be tetragonal. On account of the large number of compounds and for reasons of economising on space, a tabular presentation of the x-ray data for all the compounds has been omitted. The x-ray data of a few characteristic diagrams are shown in tables 3.2, 3.3 and 3.4. The lattice constants of all the compounds are summarised in table 3.1.

Table 3.1 The lattice parameter values and unit cell volumes of the ternary compounds and their related quaternary compounds

SELENIDE COMPOUNDS							
Ternary	a(nm)	c/a	V(x $10^{-28}m^3$)	Quaternary	a(nm)	c/a	V(x $10^{-28}m^3$)
$CuGaSe_2$	0.5616	1.962	348	$CuGaGe\square Se_4$	0.5568	1.947	336
				$CuGaSn\square Se_4$	0.5611	1.958	346
$AgGaSe_2$	0.5992	1.817	391	$AgGaGe\square Se_4$	0.5820	1.784	352
				$AgGaSn\square Se_4$	0.5849	1.849	370
$CuInSe_2$	0.5782	2.000	387	$CuInGe\square Se_4$	0.5640	1.980	355
				$CuInSn\square Se_4$	0.5700	2.000	370
$AgInSe_2$	0.6102	1.910	434	$AgInGe\square Se_4$	0.5759	1.877	359
				$AgInSn\square Se_4$	0.5877	1.920	390
$CuAlSe_2$	0.5617	1.940	344	$CuAlGe\square Se_4$	0.5575	1.916	332
				$CuAlSn\square Se_4$	0.5604	1.954	344
$AgAlSe_2$	0.5968	1.800	355	$AgAlGe\square Se_4$	0.5871	1.755	355
				$AgAlSn\square Se_4$	0.5882	1.821	371
SULPHIDE COMPOUNDS							
$CuGaS_2$	0.5349	1.959	299	$CuGaGe\square S_4$	0.5302	1.926	287
				$CuGaSn\square S_4$	0.5358	1.956	301
$AgGaS_2$	0.5757	1.790	341	$AgGaGeS_4$	Orthorhombic a = 0.8310 b = 0.5775 c = 0.5950		285
				$AgGaSn\square S_4$	0.5757	1.844	351

Table 3.2 X-ray powder data of $CuGaSn\square Se_4$

h k l	$\sin^2\theta_{obs}$	$\sin^2\theta_{cal}$	d(Å)	I/I_o
101	0.0236	0.0237	5.0163	9.60
112	0.0573	0.0573	3.2182	100.00
103	0.0634	0.0630	3.06	7.50
200	0.0758	0.0753	2.7998	4.20
211	0.0994	0.0991	2.4449	9.60
213	0.1385	0.1383	2.0713	5.00
105	0.1421	0.1414	2.0446	5.00
220	0.1508	0.1507	1.9852	63.30
204	0.1545	0.1540	1.9609	87.50
301	0.1745	0.1744	1.8450	4.20
312	0.2085	0.2080	1.6882	75.80
116	0.2145	0.2142	1.6643	37.50
323	0.2897	0.2890	1.4323	6.70
400	0.3016	0.3013	1.4036	24.20
008	0.3141	0.3140	1.3755	10.80
332	0.3589	0.3586	1.2866	17.50
316	0.3652	0.3650	1.2755	30.80
424	0.4556	0.4551	1.1421	35.80
228	0.4643	0.4645	1.1314	16.70
512	0.5096	0.5093	1.0799	15.80
336	0.5110	0.5155	1.0785	10.00
11 $\underline{10}$	0.5283	0.5281	1.0606	6.70
440	0.6022	0.6026	0.9935	5.00
408	0.6153	0.6152	0.9828	10.00
532	0.6597	0.6599	0.9491	9.20
516	0.6663	0.6662	0.9444	8.80
13 $\underline{10}$	0.6789	0.6787	0.9355	9.20
620	0.7531	0.7533	0.8883	10.90
604	0.7562	0.7564	0.8865	10.90
02 $\underline{12}$	0.7822	0.7816	0.8716	5.00
536	0.8167	0.8168	0.8530	8.30
33 $\underline{10}$	0.8300	0.8295	0.8461	4.20
448	0.9161	0.9165	0.8054	8.30
712	0.9612	0.9612	0.7863	9.20
15 $\underline{10}$	0.9802	0.9801	0.7786	6.70

Table 3.3 X-ray powder data of $AgGaSn\square Se_4$

h k l	$\sin^2\theta_{obs}$	$\sin^2\theta_{cal}$	d(Å)	I/I_o
101	0.0225	0.0225	5.087	15.4
112	0.0557	0.0551	3.264	100
103	0.0638	0.0631	3.051	7.7
211	0.0926	0.0920	2.531	9.2
213	0.1334	0.1330	2.110	7.7
220	0.1406	0.1401	2.055	69.2
204	0.1520	0.1510	1.975	93.8
312	0.1945	0.1941	1.745	76.9
116	0.2181	0.2180	1.650	38.5
400	0.2790	0.2781	1.458	24.6
008	0.3250	0.3250	1.353	10.8
332	0.3340	0.3332	1.333	21.5
316	0.3567	0.3566	1.290	27.7
424	0.4295	0.4290	1.176	47.7
228	0.4642	0.4641	1.131	15.4
512	0.4728	0.4721	1.121	20.0
336	0.4964	0.4960	1.094	15.4
11 $\underline{10}$	0.5426	0.5426	1.047	7.7
440	0.5561	0.5560	1.0340	7.7
408	0.6026	0.6028	0.993	10.8
532	0.6110	0.6110	0.986	13.8
516	0.6340	0.6343	0.968	10.8
13 $\underline{10}$	0.6812	0.6815	0.934	12.3
620	0.6948	0.6948	0.925	13.8
604	0.7061	0.7065	0.918	10.8
536	0.7730	0.7733	0.877	15.4
20 $\underline{12}$	0.8000	0.8000	0.862	10.8
33 $\underline{10}$	0.8200	0.8200	0.852	9.2
448	0.8800	o.8800	0.822	12.3
712	0.8880	0.8880	0.818	12.3
15 $\underline{10}$	0.9580	0.9592	0.787	10.8

Table 3.4 X-ray powder data of $AgGaGe\square Se_4$

h k l	$\sin^2\theta_{obs}$	$\sin^2\theta_{cal}$	d(A)	I/I_o
101	0.0232	0.0231	5.040	9.8
112	0.0575	0.0572	3.204	100.0
200	0.0700	0.0701	2.979	6.1
211	0.936	0.0933	2.516	7.3
220	0.1410	0.1405	2.047	72.0
204	0.1590	0.1585	1.928	95.1
312	0.1980	0.1976	1.728	87.8
303	0.2077	0.2076	1.691	9.8
116	0.2350	0.2342	1.588	36.6
400	0.2820	0.2810	1.450	28.0
402	0.3054	0.3050	1.394	6.1
332	0.3389	0.3380	1.324	18.3
008	0.3540	0.3530	1.295	9.8
316	0.3750	0.3740	1.257	25.6
424	0.4403	0.4400	1.161	45.1
512	0.4804	0.4800	1.112	19.5
228	0.4944	0.4940	1.096	18.3
336	0.5150	0.5150	1.074	12.2
440	0.5624	0.5620	1.028	11.0
11 $\underline{10}$	0.5910	0.5900	1.002	5.0
532	0.6202	0.6200	0.979	14.6
408	0.6353	0.6345	0.966	9.8
516	0.6557	0.6551	0.952	11.0
620	0.7023	0.7021	0.920	11.0
604	0.7207	0.7200	0.908	9.8
13 $\underline{10}$	0.7273	0.7270	0.903	9.8
536	0.7956	0.7952	0.864	8.5
33 $\underline{10}$	0.8670	0.8670	0.828	6.1
712	0.8991	0.8992	0.813	8.5
448	0.9145	0.9145	0.806	8.5

An inspection of the subscripts showed, as can be seen from tables 3.2, 3.3 and 3.4, the following interference rules:

h k l	only existing where	h + k + l	= 2n
o k l	only existing where	k + l	= 2n
h h l	only existing where	2h + l	= 4n and l = 2n
h o o	only existing where	h	= 2n
o o l	only existing where	l	= 4n
h h o	only existing where	h	= 2n

These interference rules can be brought into agreement upon inspection of a zinc-blende like lattice with interference laws of the space group of the chalcopyrite (D_{2d}^{12}) $I\bar{4}2d$.

A computer programme was used to calculate d and θ for copper k_{α_1}, k_{α_2} radiation and the weighted mean. The films are shown in fig 3.4 & 3.5. In fig 3.5 the comparison of the x-ray patterns between the ternary and analogue quaternary compounds are shown. The comparison of the x-ray patterns of the quaternary $CuGaSn\square Se_4$ polycrystalline (before growth) and the single crystal of the same compound (after growth) are shown in fig. 3.4. Resolution of the k_{α_1} and k_{α_2} doublets are clearly observed at high θ values. The films were measured accurately using a vernierruler and film shrinkage errors corrected.

If the camera constants are known accurately, there are two main sources of systematic error. Absorption of the x-rays tends to shift the lines to higher θ values. Eccentricity of the sample in the direction of the x-ray beam will increase or decrease θ depending on the sense of the displacement. Both of these effects become zero for backscattering ($\theta=90^{o}$), so that a least squares fit to a correction function θ which extrapolates the calculated values of the lattice parameters from the various lines to $\theta = 90^{o}$ gives an accurate determination of the lattice constants. Various correction functions including the Nelson-Riley formula for absorption (33) were tried in a computer programme written by Y.L.Lee (34).

(a)

(b)

Fig. 3.4 Comparison of the powder diffraction patterns of $CuGaSn\square Se_4$ polycrystalline (a) and single crystal (b)

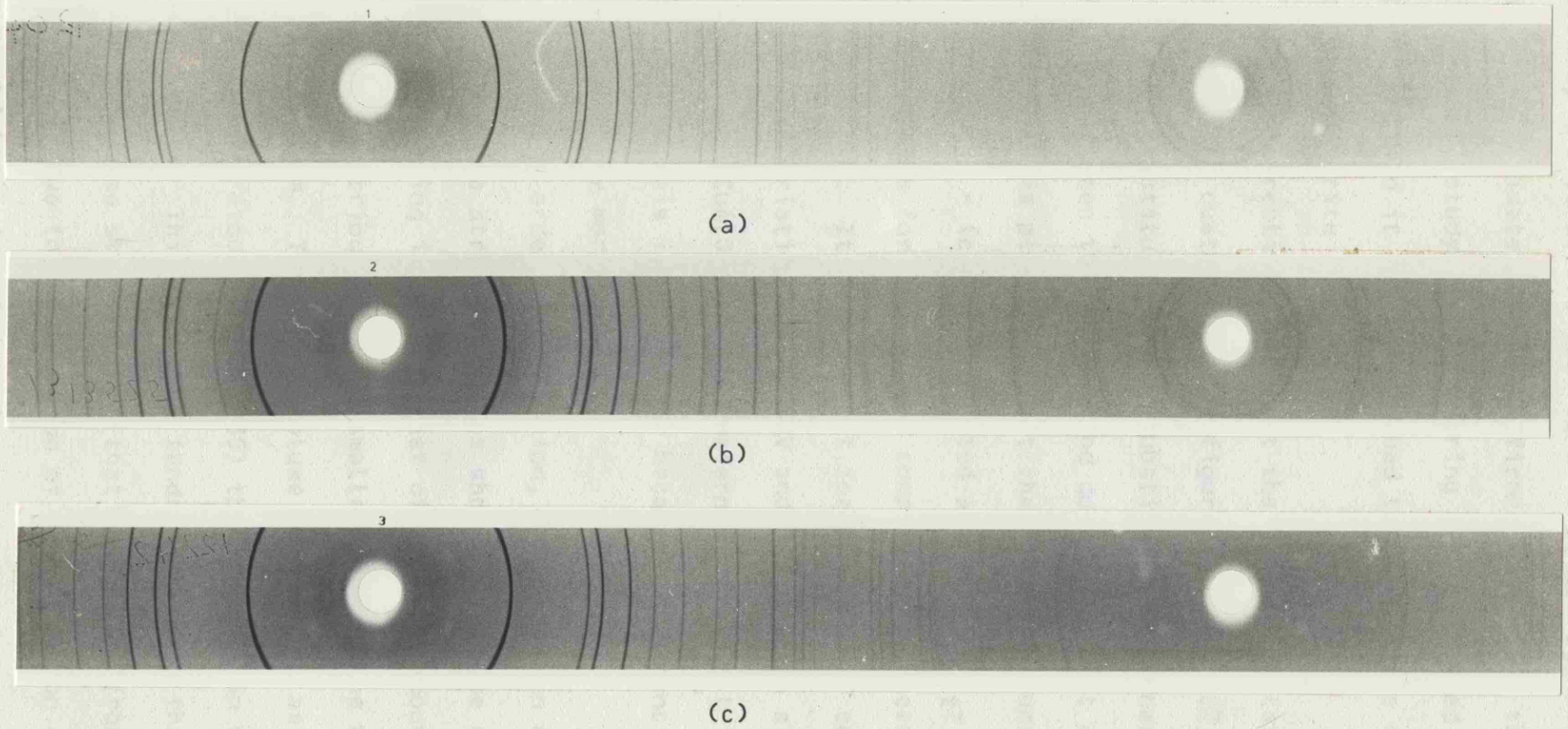

Fig. 3.5 Comparison of the powder diffraction patterns of $AgGaSn\square Se_4$ (a), $AgGaSe_2$ (b) and $AgGaGe\square Se_4$ (c)

For all twelve selenide compounds and three of the sulphur compounds, the structure was found to be tetragonal (26). The (c/a) ratio of approximately 2 was confirmed for all of the tetragonal compounds by a study of the ordering lines observed in the powder photographs, and it was established that all these compounds showed a defect chalcopyrite structure.

It is interesting to look at the changes in lattice parameter from ternary to quaternary. In figures 3.6 and 3.7, for the set of both the Ge substituted and Sn substituted quaternary compounds, the difference between the ternary and quaternary unit cell volumes ($\Delta V = V_t - V_q$) is plotted against the ternary volume V_t, and similarly $\Delta(c/a) = (c/a)_t - (c/a)_q$ is plotted against $(c/a)_t$. The lattice parameter values for the ternary compounds have been taken from the literature (39). It is seen that for each set of compounds there is a systematic variation of both ΔV and $\Delta(c/a)$. In all cases except $CuGaSn\square Se_4$ and $CuAlSn\square Se_4$ the quaternary unit cell is smaller than the ternary one. This is presumably because the vacancies allow the atoms to pack slightly more closely.

To a first order approximation, the variation of ΔV with V_t can be represented as a straight line as shown, the slope of the line for the Ge compounds being 1.47 times that of the Sn compounds. This larger slope can be attributed to the smaller size of the Ge atom compared with the Sn atom. Taking the volume of the atom as proportional to the cube of the atomic radius (35) the ratio of Sn volume to Ge volume is 1.50. This agreement tends to confirm that the compounds all have the same structure and that the change from ternary to quaternary is due to substitution of a combination of atom and lattice vacancy which requires less volume.

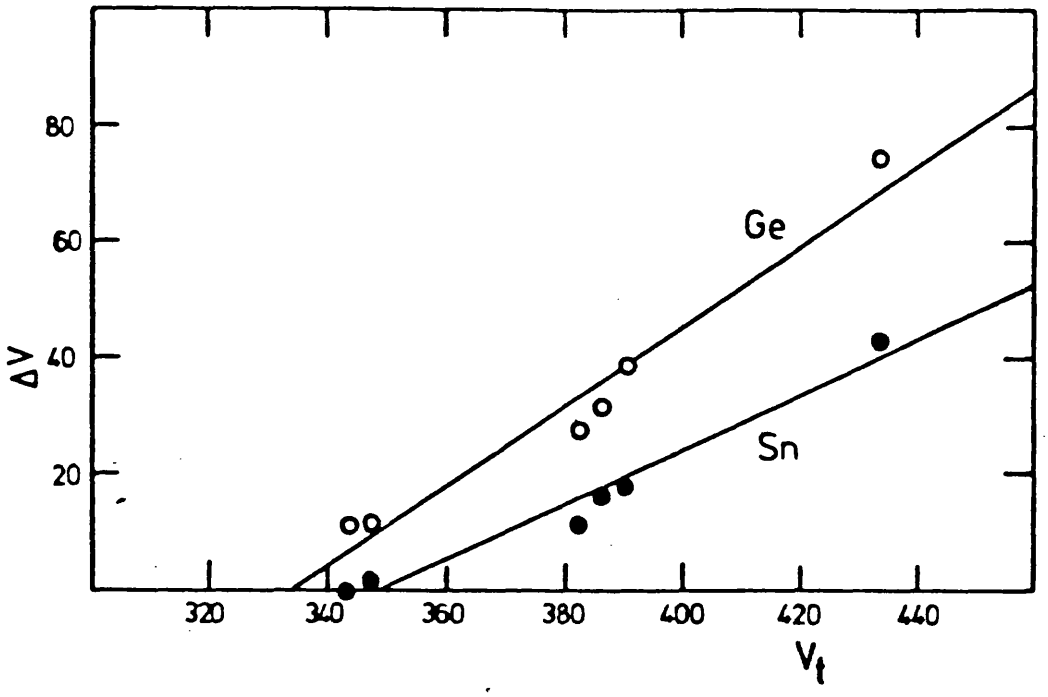

Fig. 3.6 The variation of $V = V_T - V_Q$ with V_T for Ge and Sn substituted quaternary compounds.

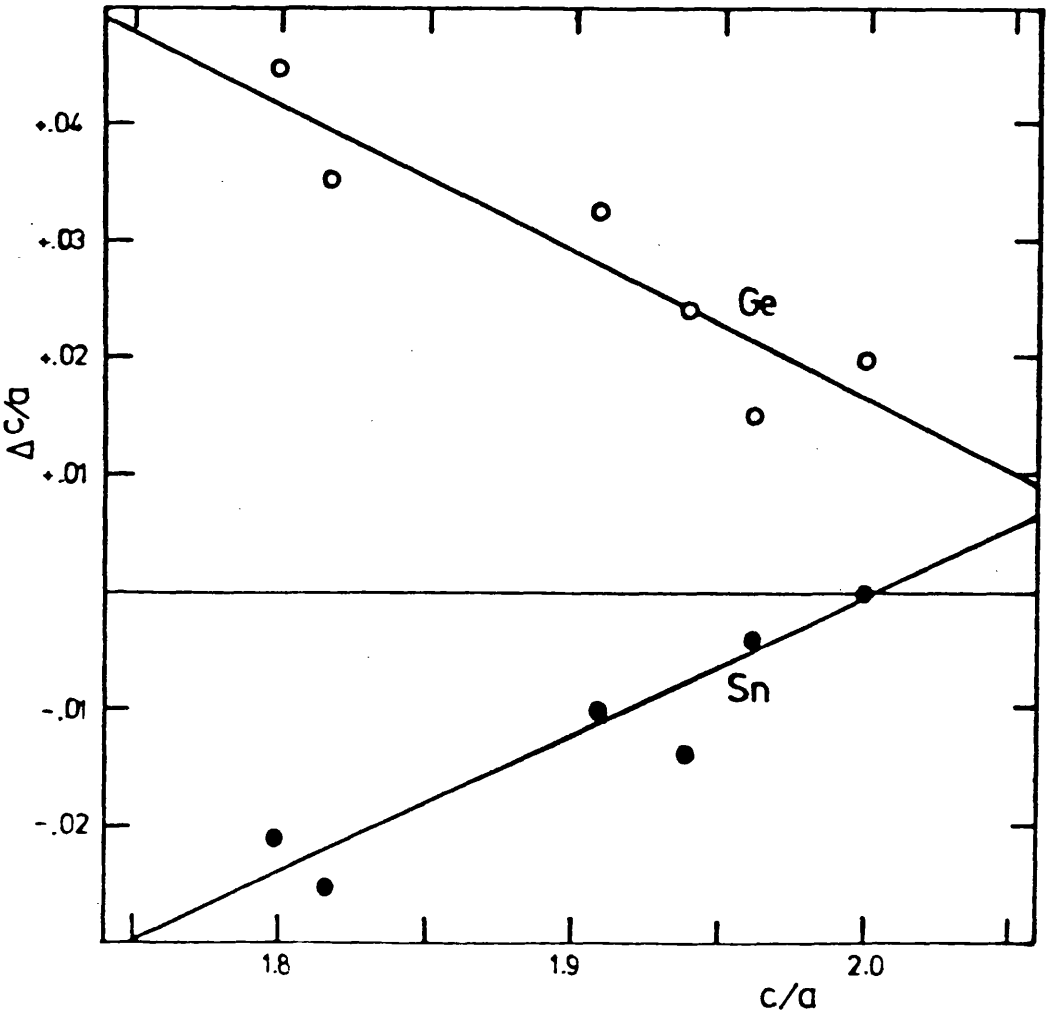

Fig. 3.7 The variation of $c/a = (c/a)_T - (c/a)_Q$ with $(c/a)_T$ for Ge and Sn substituted quaternary compounds.

In the case of $\Delta(c/a)$, $\Delta(c/a)$ is positive for the Ge compounds (the ternary c/a is larger than the quaternary) but is negative for the Sn compounds. The value of $\Delta(c/a)$ are relatively small and hence less accurate, but again a straight line. The line having positive slope for the Sn compounds and negative slope for the Ge compounds. The magnitude of the two slopes is, within the limits of experimental error, equal.

A very similar effect was observed by W.Schäfer and R.Nitsche (11) in the normal quaternary adamantine compounds reported in the table 3.5. This table contains the reduced cell volumes V_r, i.e. the volumes of one unit of Cu_2-II-IV-S_4 (Se_4). An increase of V_r in the sequence Si-Ge-Sn is observed in each column. On passing from $Cu_2CdSiSe_4$ to $Cu_2CdGeSe_4$ an exception is noted, but it should be taken into consideration that a change in structure from wurtz-stannite to stannite is occurring, too. Within each row (variation of the II-element), V_r tends to decrease in the sequence II = Mn-Fe-Co-Ni. The differences in V_r between neighbouring compounds are smallest in the rows where IV = Sn. In the sequence II = Zn-Cd-Hg, on the other hand, Vr increases, the major increments lying between the Zn and the Cd compounds.

It is interesting to point out that the c/a ratio for the normal quaternary compounds is bigger than the defect quaternary compounds (tables 2.1 and 2.2). This is the indication that the structure of the defect quaternary compounds is more distorted than the structure of the normal quaternary compounds, and bigger non-linear effects should be expected in the defect quaternary compounds.

Table 3.5 The reduced cell volumes V_r and structure of the normal quaternary compounds

Formula	Cu_2MnSiS_4	Cu_2FeSiS_4	Cu_2CoSiS_4	Cu_2NiSiS_4	Cu_2SnSiS_4	Cu_2CdSiS_4	Cu_2HgSiS_4
Lattice	O.rh.	O.rh.	tetr.	monic.	O.rh.	O.rh.	O.rh.
Vr[Å^3]	149.8	145.8	143.4	141.5	145.9	154.5	154.3
Structure	WSt	WSt	St	Sph(def)	WSt	WSt	WSt
Formula	Cu_2MnGeS_4	Cu_2FeGeS_4	Cu_2CoGeS_4	Cu_2NiGeS_4	Cu_2ZnGeS_4	Cu_2CdGeS_4	Cu_2HgGeS_4
Lattice	O.rh.	tetr.	tetr.	O.rh.	O.rh.	O.rh.	tetr.
Vr[Å^3]	154.5	149.5	147.2	146.7	150.3	158.8	159.0
Structure	WSt	St	St	Sph(def)	WSt	WSt	St
Formula	Cu_2MnSnS_4	Cu_2FeSnS_4	Cu_2CoSnS_4	Cu_2NiSnS_4	Cu_2ZnSnS_4	Cu_2CdSnS_4	Cu_2HgSnS_4
Lattice	tetr.	tetr.	tetr.	Cubic	tetr.	tetr.	tetr.
Vr[Å^3]	161.6	159.9	157.7	159.7	159.8	169.0	168.6
Structure	St	St	St	Sph	St	St	St
Formula	$Cu_2MnSiSe_4$	$Cu_2FeSiSe_4$	$Cu_2CoSiSe_4$	$Cu_2NiSiSe_4$	$Cu_2ZnSiSe_4$	$Cu_2CdSiSe_4$	$Cu_2HgSiSe_4$
Lattice	O.rh.	tetr	Synthesis so far unsuccessful		O.rh.	O.rh.	O.rh.
Vr[Å^3]	174.2	168.6			169.3	179.0	178.5
Structure	WSt	St			WSt	WSt	WSt
Formula	$Cu_2MnGeSe_4$	$Cu_2FeGeSe_4$	$Cu_2CoGeSe_4$	$Cu_2NiGeSe_4$	$Cu_2ZnGeSe_4$	$Cu_2CdGeSe_4$	$Cu_2HgGeSe_4$
Lattice	O.rh.	tetr	O.rh.	tetr.	tetr.	tetr.	tetr.
Vr[Å^3]	179.6	173.0	171.3	171.3	174.8	175.8	178.7
Structure	WST	St	Sph	Sph(def)	St	St	St

Table 3.5 continued/

Formula	$Cu_2MnSnSe_4$	$Cu_2FeSnSe_4$	$Cu_2CoSnSe_4$	$Cu_2NiSnSe_4$	$Cu_2ZnSnSe_4$	$Cu_2CdSnSe_4$	$Cu_2HgSnSe_4$
Lattice	tetr.	tetr.	Cubic	Cubic	tetr.	tetr.	tetr.
Vr[Å^3]	188.5	181.8	184.9	185.7	183.0	193.9	194.3
Structure	St	St	Sph	Sph	St	St	St

3.5 Differential thermal analysis (DTA)

DTA measurements were carried out with a Dupont Thermoanalyzer unit. The starting materials for each DTA run were the polycrystalline compounds prepared in the way reported in section 3.2, and subjected to x-ray diffraction analysis, before being sealed into evacuated quartz ampoules containing thermocouples as shown in fig 3.8. The thermocouples were in intimate contact with the vessels containing the samples and reference substance, detected differences in temperature between the sample and the reference as they were both heated and cooled. The variable, ΔT, is plotted against either actual sample temperature, as detected in the centre of the sample, or against time.

In DTA a reference material is required to balance the thermal diffusivity of the sample. It is imperative, that the reference material has no thermal activity (phase transitions, chemical reactions, etc.) in the temperature range being studied. Silver was the reference material used in our measurements.

Some of the thermograms obtained are shown in figures 3.9, 3.10 and 3.11. The melting points and transition temperatures of some of the defect quaternary adamantine compounds are summarised in table 3.6.

The letters in fig. 3.9 are shown to illustrate the analysis of the thermograms. On raising the temperature of the furnace, a small but steady temperature difference develops between the test and reference materials. This is because, although the temperature at the centres of both materials will lag behind that of the furnace, the magnitude of the lag depends primarily on the thermal conductivity and heat capacity of each substance. The DTA curve continues in an approximately rectilinear manner, until the test material undergoes some physical or chemical change (AB). At point B, the curves begin

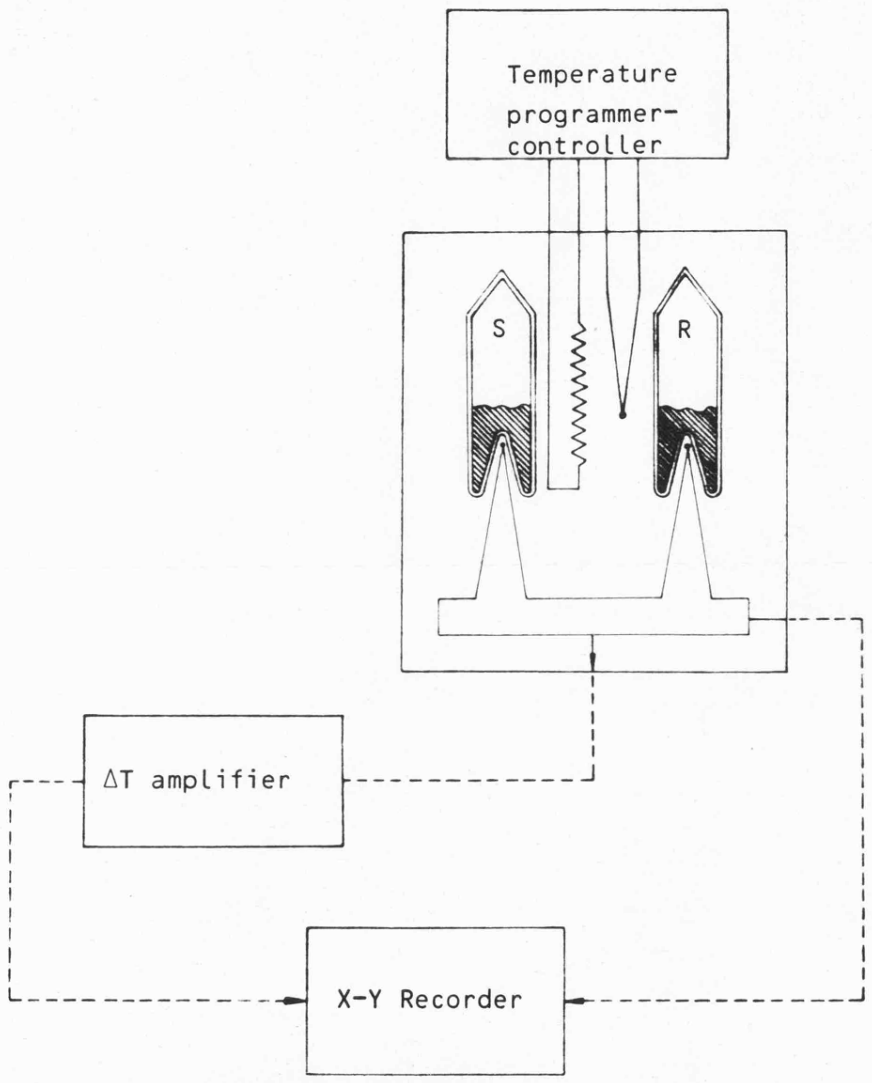

Fig. 3.8 Block diagram of DTA apparatus

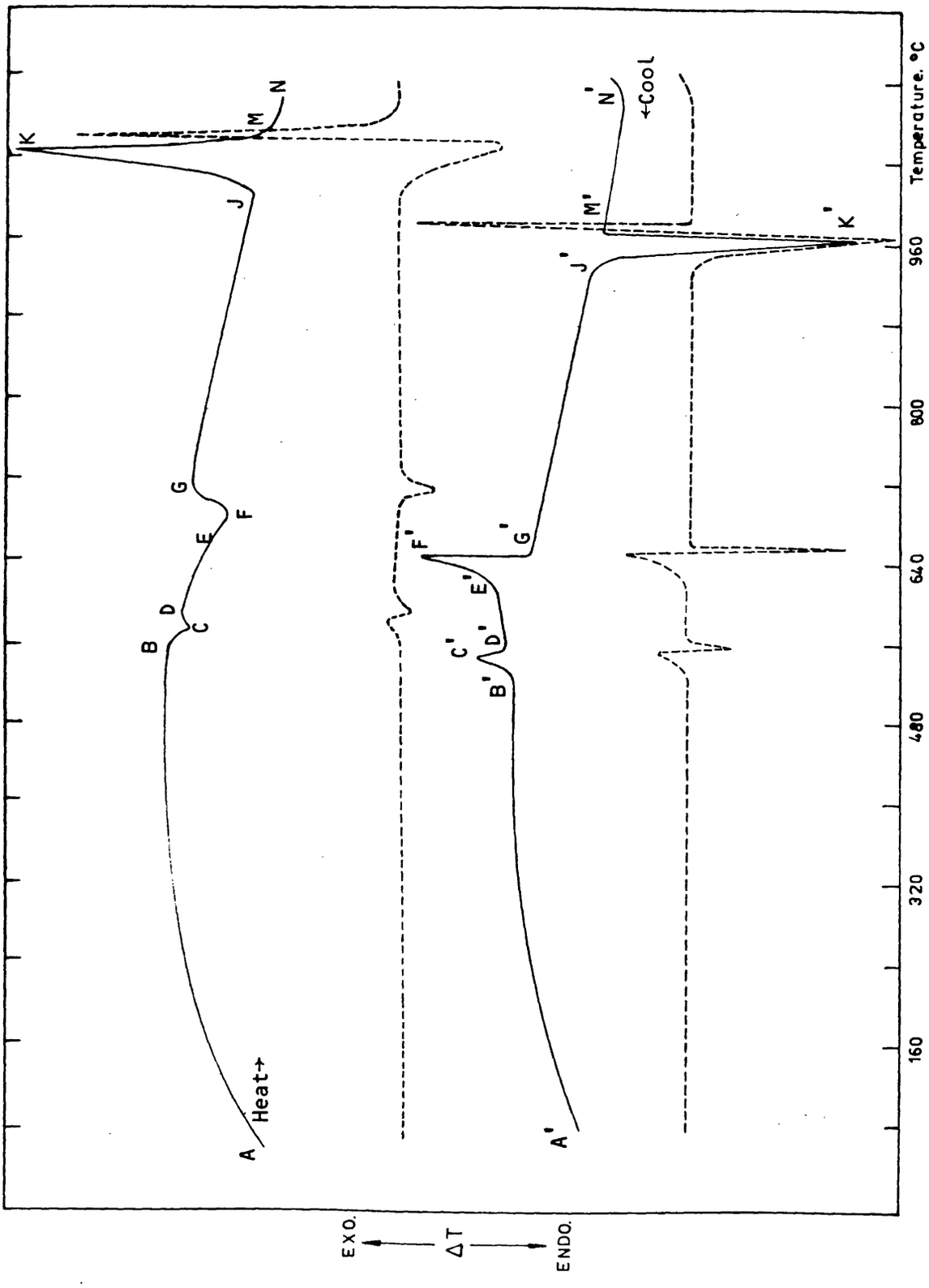

Fig. 3.9 DTA curves of heating, cooling of $AgGaSnSe_4$ (solid line) and the first derivatives $d(\Delta T)/dT$ (dashed line).

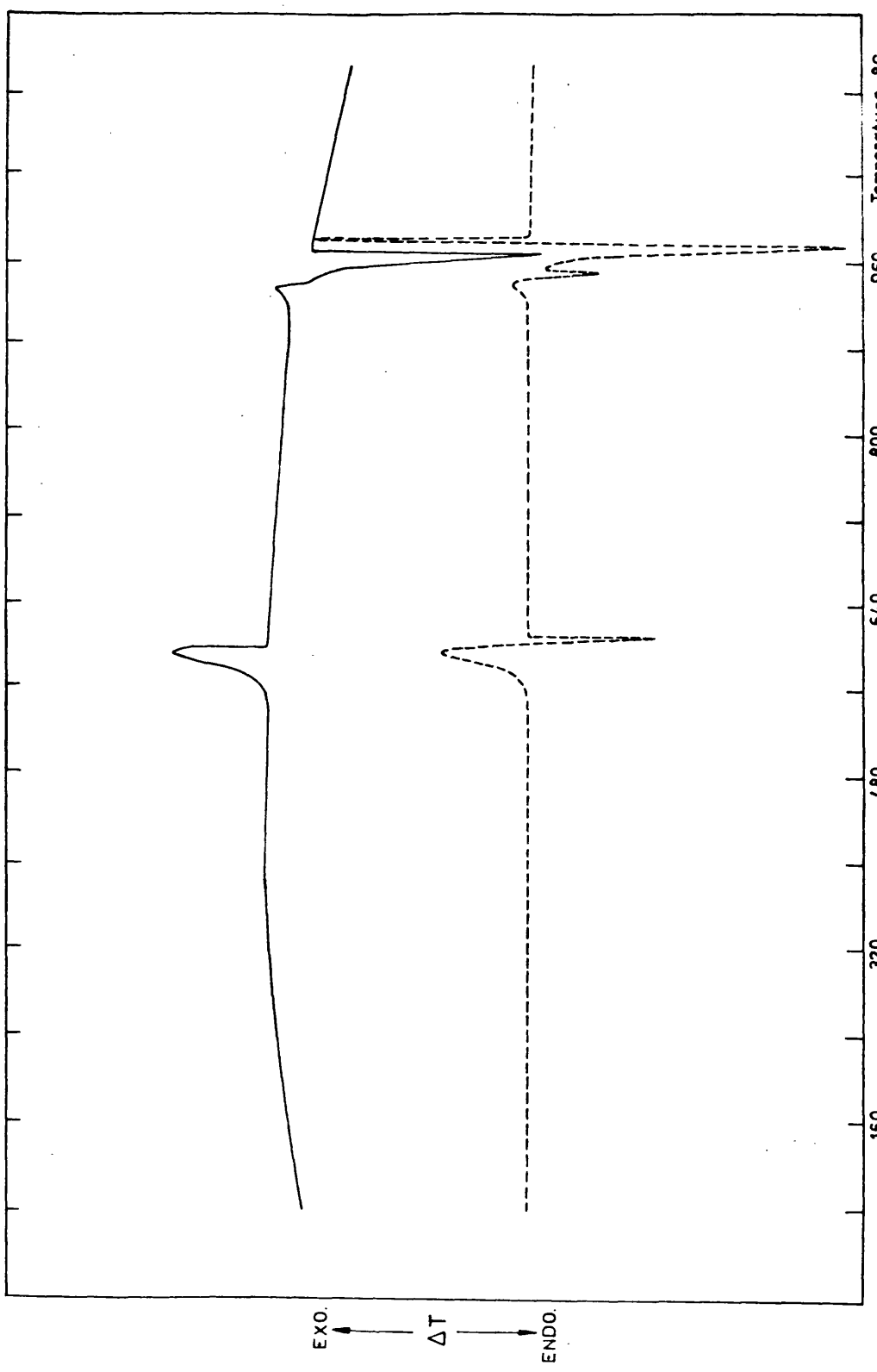

Fig. 3.10 DTA curve of cooling $CuGaSnOSe_4$ (solid line) and the first derivative d(ΔT)dT (dashed line).

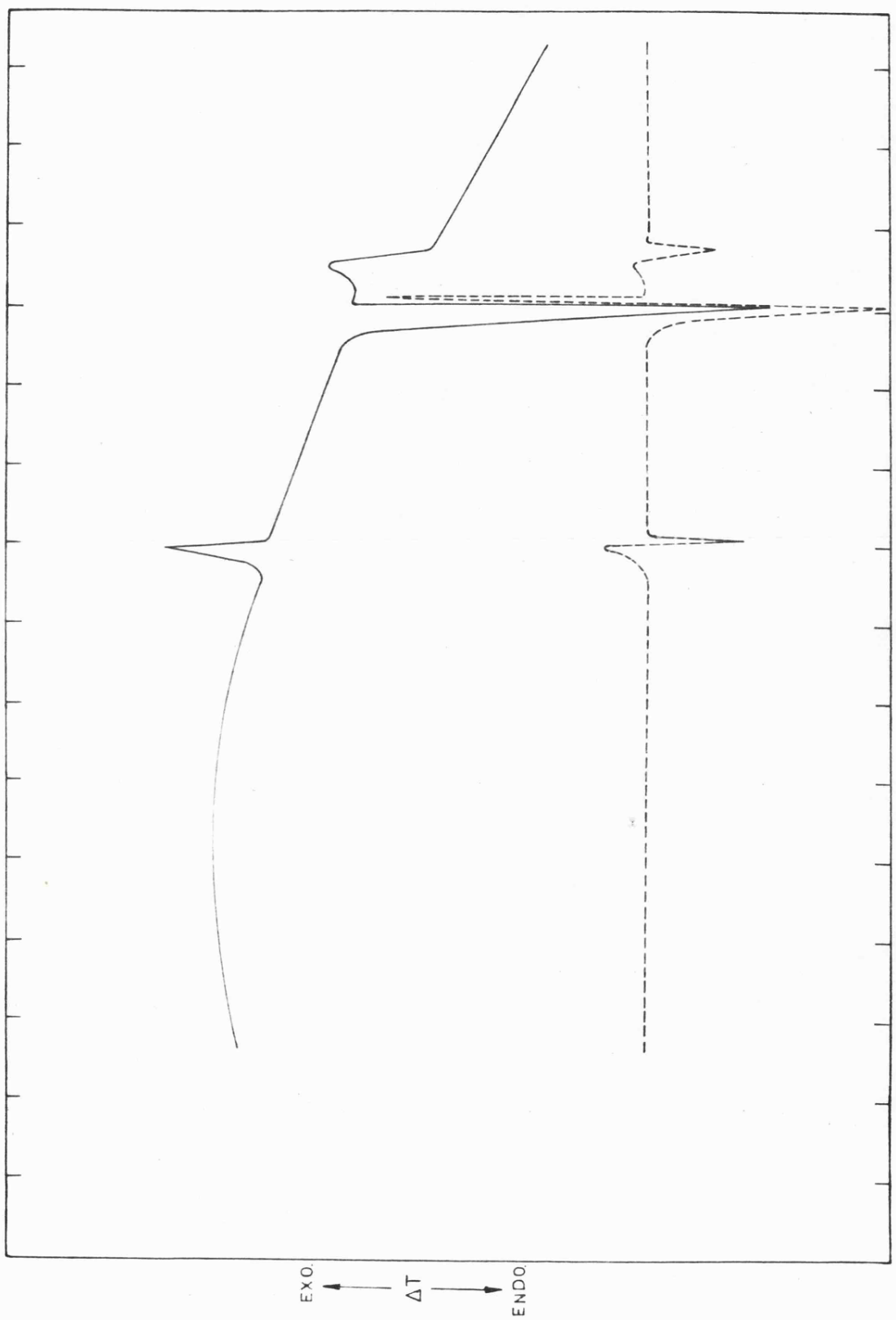

Fig. 3.11 DTA curve of cooling $CuGaGe\square Se_4$ (solid line) and the first derivative $d(\Delta T)/dT$ (dashed line)

to deviate from the base line, due to an endothermic process occurring within the test sample. This point, B, will be referred to as the onset temperature of the reaction, or phase transition. A high temperature x-ray camera was employed to determine the change at this temperature in $CuGaSn\square Se_4$. At 590°C. $CuGaSn\square Se_4$ decomposed into phases probably $CuGaSe_2$ and $SnSe_2$. Detail of this analysis is given in chapter 4. The transition temperature given by high temperature x-ray analysis is the same as for the DTA measurements (see fig. 3.10). The endothermic peak temperature, C, corresponds to the maximum rate of heat consumption detected by the differential thermocouples. It does not necessarily correspond to the maximum rate of reaction, nor to completion of the endothermic process. Generally, the peak temperature tends to show a much greater variation with heating rate. It is interesting to point out that there are small shifts in the peaks in the heating process than the cooling process (see fig. 3.9).

The endothermic process giving rise to the peak BCD becomes complete at some temperature between the points C and D, so the curve returns to a new base line DE. At point, E, a new deviation from the base line is observed and the peak EFG becomes complete when all the test sample is melted.

The onset of an exothermic process is indicated by the upwards deflection of the base line at J, giving rise to the exothermic peak JKM. This peak becomes complete when the reference sample is melted. Completion of this process and the formation of a new, thermally stable phase, is confirmed by the horizontal portion of the curve, MN.

The cooling process starts on the point N'. An endothermic peak M' K' J' indicates that the reference material (Ag) is frozen. An exothermic peak during lowering of the temperature indicates freezing of the sample, and the exothermic peak D' C' B', shows the transition temperature more accurately than the heating process. The onset

temperature gave the best measure of transition, or reaction temperature, and this could be most accurately obtained from the first derivative of a DTA curve as shown by dashed lines in figures 3.9, 3.10 and 3.11.

TABLE 3.6. RESULTS OF THE PEAKS OBSERVED IN DTA

Sample	Melting Points (^{o}C)	Transition Temperatures (^{o}C)
$CuGaSn\square Se_4$	936	590
$CuGaGe\square Se_4$	1000	710
$CuGaSn\square S_4$	792	648
$AgGaSn\square Se_4$	650	550
$AgGaSn\square S_4$	632	592,512

3.6 Crystal growth by modified Pendölofen vapour transport

For growing crystals silica ampoules are normally used with tapered tips and thin silica rods attached to the tip of the ampoule. A special treatment is necessary to decrease the number of active sites on the silica wall. The silica tubes are vigorously washed with de-ionized water, scrubbed with a clean brush and washed with acetone. They are then put in a mixture of HF - HNO_3 (1:1) for two hours and washed with deionised water. During glass blowing and after shaping, a systematic flame polishing is given from the one end of the ampoule to the other. The ampoules are then washed with deionized water, dried, evacuated to 10^{-5} torr, and heated overnight at 1000^{o}C to remove traces of HF and H_2O.

The flame polishing is of great importance because it closes any micropores or striations on the surface of silica. Its great importance has been shown by Kaldis (36) Fray and Nielsen (37), comparison of the critical undercooling of the same substance in treated and untreated

silica. In several cases the critical undercooling on treated silica is appreciably increased.

Another source of nucleation sites is the charge material itself. During charging of the ampoule the walls often come in contact with the powder of the starting material. These undesirable nucleation sites can be avoided by taking the two following precautions. The first is to fill the ampoule with a funnel, and the second is to subject the ampoule to a reverse-transport situation after sealing and before growth.

A chemical transport reaction is brought about by means of a temperature gradient in a system consisting of a solid phase and a transporting gaseous phase; the reaction is based on the temperature dependence of the equilibrium constant of the system. If the transport reaction is endothermic the transport takes place from the hot to the cold zone, the transporting phase being unsaturated in the hot zone and supersaturated in the cold zone, with a saturation boundary in between. If the reaction is exothermic the transport goes in the opposite direction. The method involves sealing the reacted material with small amounts (5mg/cc) of iodide in a evacuated fused silica. The iodide serves as a carrier as a volatile iodide according to reactions such as

$$CuGaSnSe_4 + 4I_2 \rightleftarrows CuI\uparrow + GaI_3\uparrow + SnI_4\uparrow + 2Se_2\uparrow \quad (3.2)$$

$$AgGaSnSe_4 + 4I_2 \rightleftarrows AgI\uparrow + GaI_3\uparrow + SnI_4\uparrow + 2SE_2\uparrow \quad (3.3)$$

$$AgGaGeSe_4 + 4I_2 \rightleftarrows AgI\uparrow + GaI_3\uparrow + GeI_4\uparrow + 2Se_2\uparrow \quad (3.4)$$

The right side of the equation of the equation is generally in the hot zone and the left side in the cooler zone. In order to obtain better nucleation control and growth few bigger single crystals of $CuGaSn\square Se_4$, $AgGaSn\square Se_4$, $AgGaGe\square Se_4$ and $CuGaGe\square Se_4$, we used a modified temperature oscillation method in a two zone furnace.

A schematic of the two-zone furnace is shown in Fig. 3.12 (b). The left and right heaters are constructed of Kantal A-1 heating elements (ca. 30 oh ms) wound on alumina ceramic tubes. The tubes are 60 cm long x 40 mm diameter. The windings are secured by alumina cement. Wound round the furnace tube are several layers of ceramic fibre insulation blanket, which reduces radial heat losses. The air gap between the two zones is created by using four support spacers at the outside corners of the primary furnace insulation. The effect of the air gap can be seen in the static furnace profile of fig. 3.12(a). Radiation loss increases the gradient and substantially affects the temperature profiles of the two zones.

The deposition zone was subjected to a periodic increase of $30^{o}C$ in temperature during growth. This was designed to cause small newly-nucleated crystals to re-evaporate leaving only a few seeds to grow to maturity. The fluctuation was generated by a microprocessor programmed in five steps. The source zone was separately controlled and heated up in two stages.

During stage one, both zones were heated up quite fast, but the deposition zone was kept the hotter. This reverse temperature gradient keeps the deposition zone clean. Then, stage two, the heating rate of the source is made very slow so that the deposition zone overtakes it. This is the primary nucleation period. Finally the source zone is held constant at the chosen temperature of about $60^{o}C$ above that of the deposition zone. Figure 3.13 shows the temperature programmes of the two zones in the case of $CuGaSn\square Se_4$.

The growth period follows for two to three weeks during which time the periodic temperature fluctuations of the deposition zone are maintained.

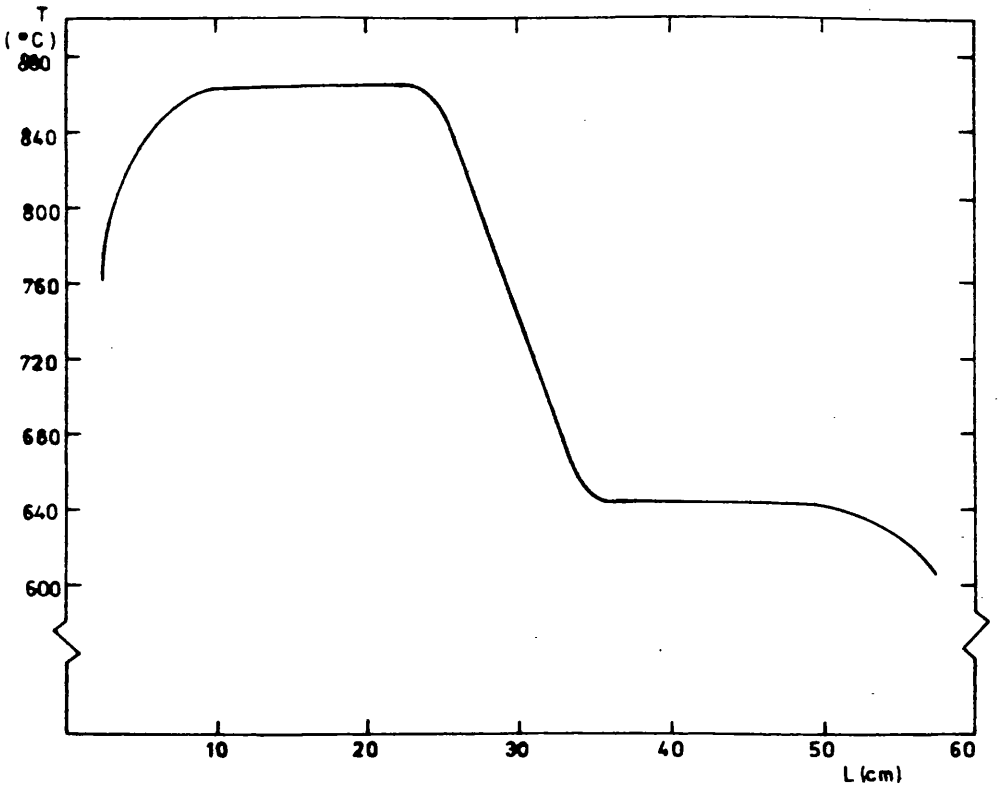

Fig. 3.12(a) Temperature profile of the two zone furnace.

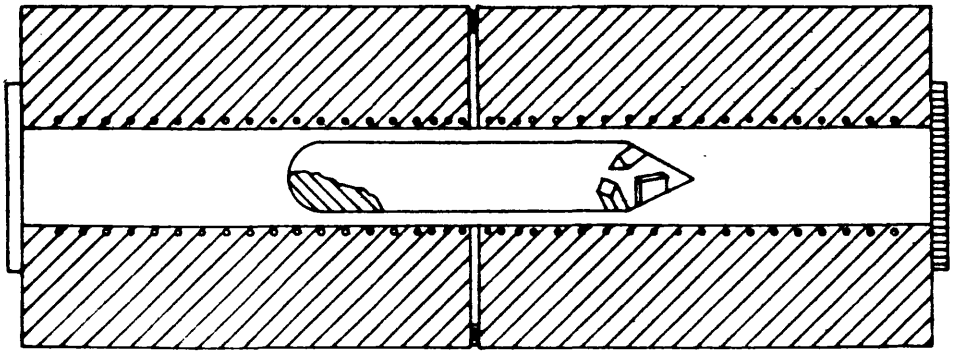

Fig. 3.12(b) Schematic drawing of the crystal growth furnace in cross section.

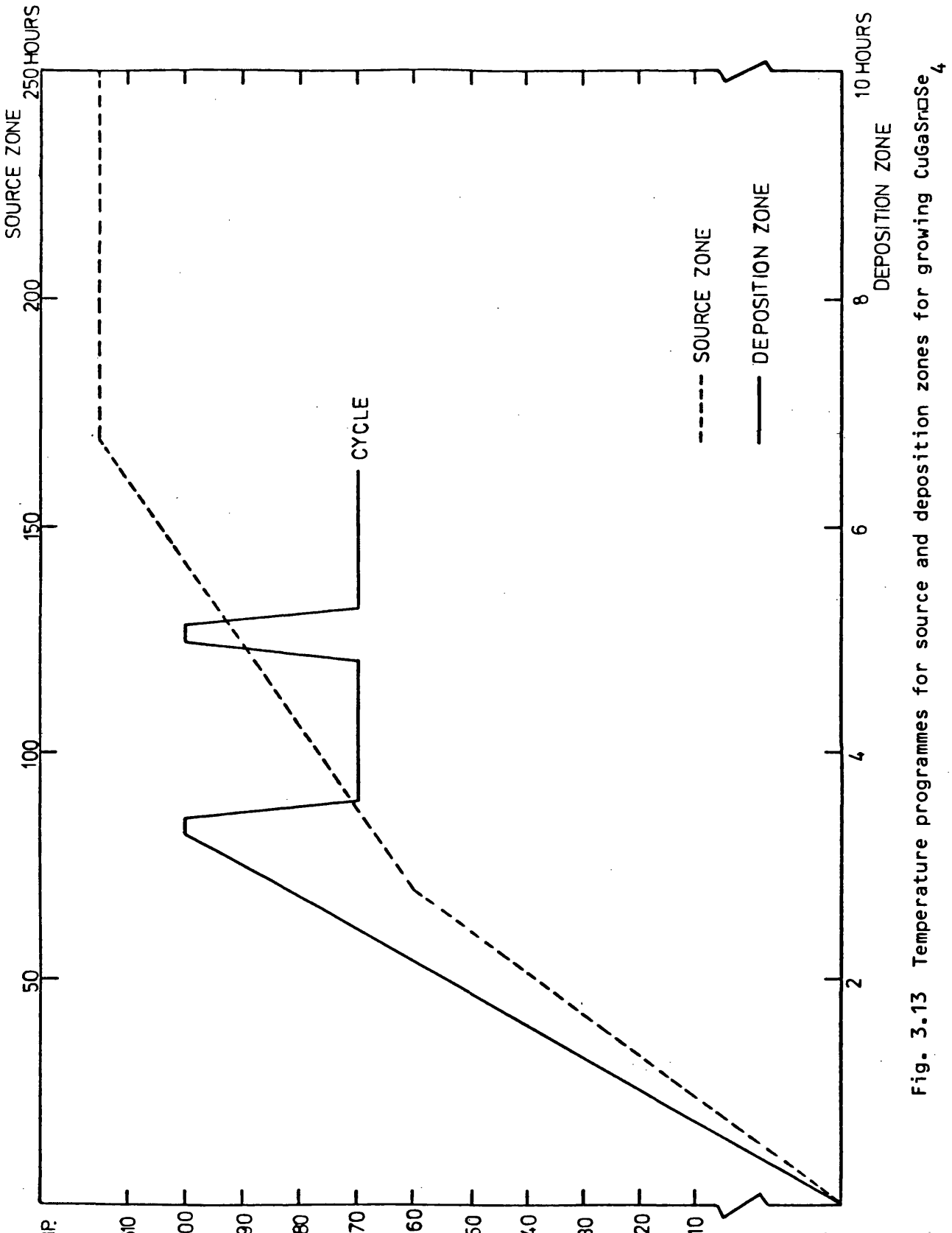

Fig. 3.13 Temperature programmes for source and deposition zones for growing $CuGaSr_2Se_4$

The primary nucleation period allows the conditions for nucleation of crystals to be met automatically, because the system will pass through the ideal set of conditions while still heating up. The temperature fluctuations of the growth period are designed to cause any secondary nuclei to die by re-evaporation, before they have a chance to complete with the primary nuclei.

The two theoretical factors that made this technique possible are (a) not all nuclei are formed simultaneously (the ones on the most active wall centres appearing first) and (b) the growth and dissolution velocity of each individual nucleus depends on its size, the smaller having higher vapour pressure, and therefore evaporating more rapidly. This effect can be described by the well known Gibbs-Thomson equation:

$$P_r = P_s \exp \frac{2\sigma M}{RT\rho r} \qquad (3.5)$$

where σ is the surface tension, M is the molecular mass, R is the gas constant, T is the absolute temperature, ρ is the density and r is the particle radius.

Well facetted prismatic and plate-like crystals of $CuGa\square Sn\ Se_4$ grew in the deposition zone. Their faces were {112} (i.e. {111} pseudo-cubic) and of several mm in dimension. Figure 3.14 shows a typical batch of crystals obtained by this method. Figure 3.15 shows the crystal $AgGaSn\square Se_4$ with pyramidal habit growth. $AgGaGe\square Se_4$ grew with pyramidol habit also.

Fig. 3.16 shows typical well developed facets of $AgGaSn\square Se_4$ and fig. 3.17 shows typical deposition-lamellae around the emergence points of single dislocation in one of the crystal $AgGaSn\square Se_4$. This crystal growth by modified Pendölofen vapour transport proved that it is possible to transport simultaneous three non-volatile metals in the closed tube.

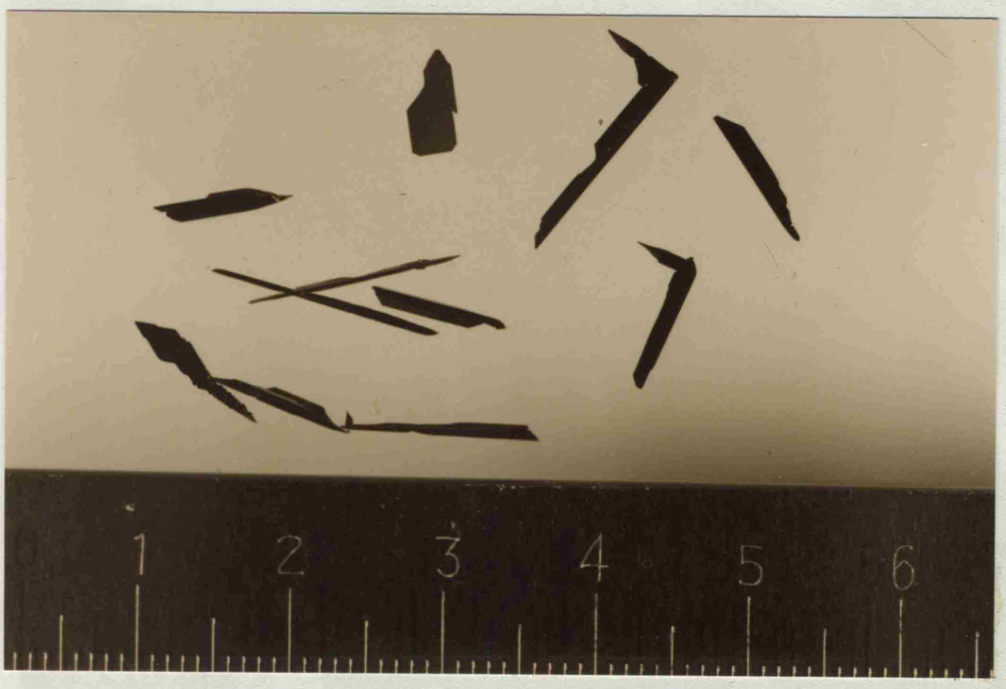

Fig. 3.14 Single crystals of $CuGaSn\square Se_4$

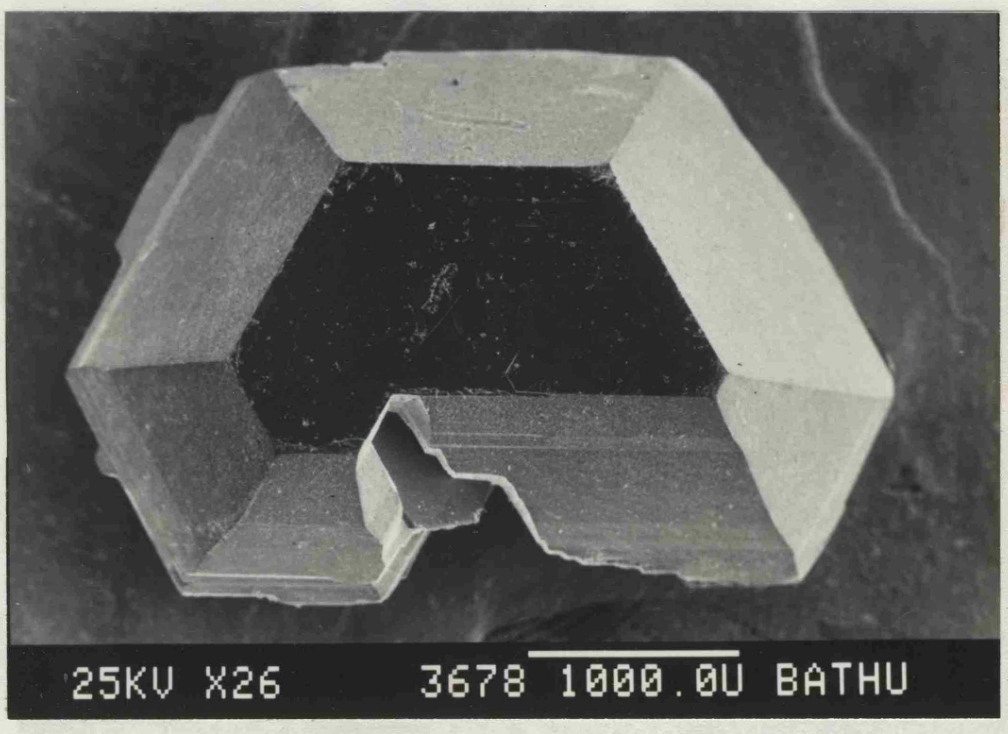

Fig. 3.15 Single crystals of $AgGaSn\square Se_4$

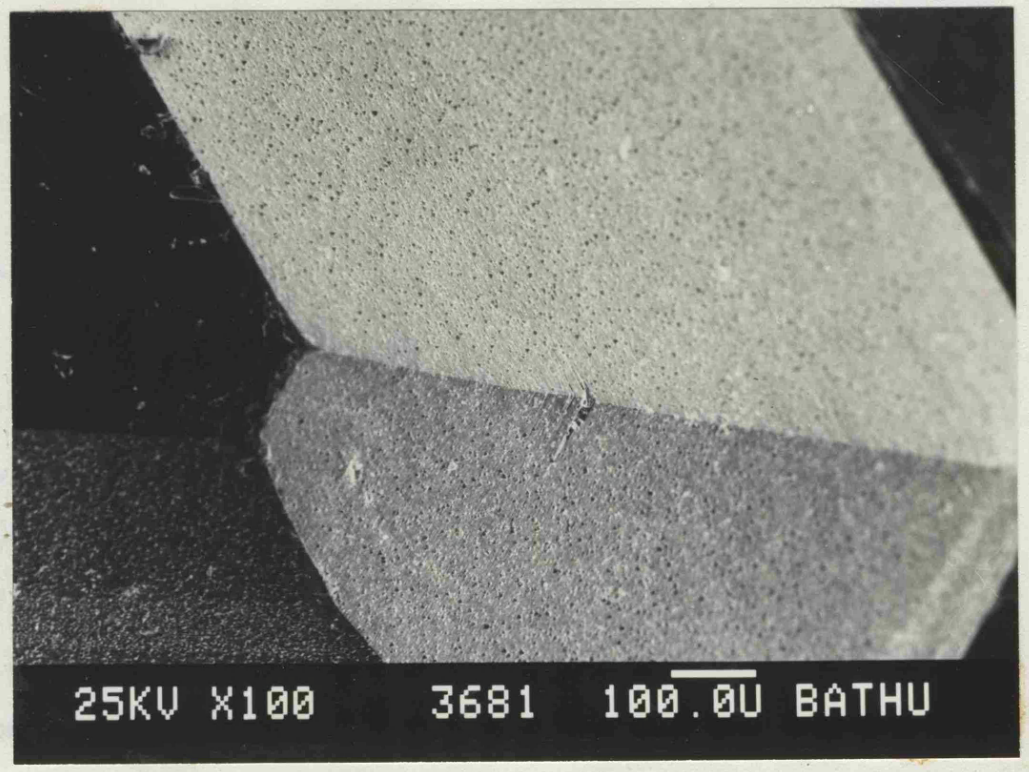

Fig. 3.16 Photograph showing typical well-developed facets of $AgGaSn\square Se_4$.

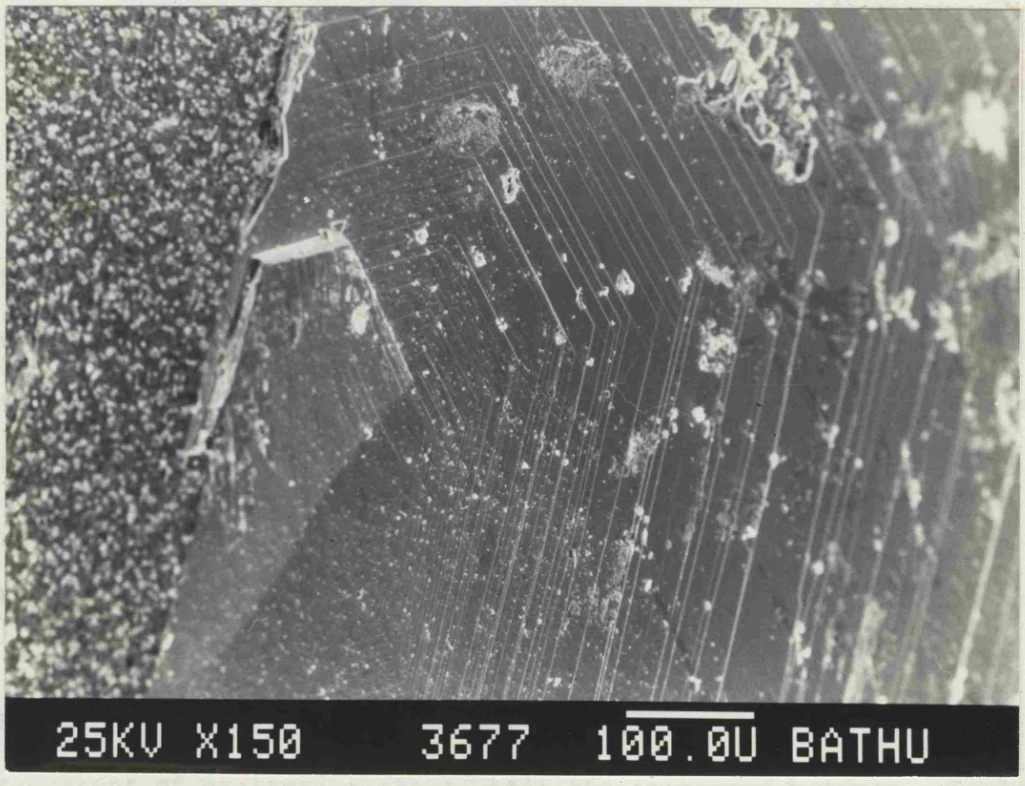

Fig. 3.17 Typical deposition-lamellae around the emergence points of a single dislocation of $AgGaSn\square Se_4$.

CHAPTER 4

CRYSTAL STRUCTURE ANALYSIS, TEMPERATURE DEPENDENCE OF LATTICE PARAMETERS AND THERMAL EXPANSION OF $CuGaSn\square Se_4$

4.1 Introduction

The object of this chapter is to study the chemical composition, crystal structure, temperature dependence of lattice parameters and evaluate the coefficients of thermal expansions α_a and α_c of $CuGaSn\square Se_4$. This material was chosen as the archetypal compound of the family of the defect quaternary adamantine compounds. Electron probe microanalysis was used to study the chemical composition of the crystal, the result of the composition within experimental error was consistent with the x-ray measurements of the chapter 3.

Single crystal diffraction methods have been used to solve the crystal structure of $CuGaSn\square Se_4$; space group $I\bar{4}2d$ (D_{2d}^{12}), a = 5.611Å, c = 10.988Å, Cu and Ga at random in (a): 0, 0, 0; Sn and □ at random in (b) 0, 0, $\frac{1}{2}$; Se in (d) 0.2571, $\frac{1}{4}$, $\frac{1}{8}$. The analysis of the crystal structure was studied in three stages. The first stage was the experimental measurement of the unit-cell dimensions, the space group and the intensities of the diffracted beams from the crystal. These intensities depend only on the nature of the atoms present and their relative positions within the unit cell. The second stage was the deduction by some method of a suggested atomic arrangement (a trial structure). The intensities of the diffraction maxima corresponding to this arrangement can then be calculated and compared with those observed. The third stage was the refinement of this suggested arrangement of scattering atoms until the agreement between calculated and observed intensities is within the limits of error of the observations.

Accurate lattice parameters of the chalcopyrite semiconductor $CuGaSn\square Se_4$ have been determined as a function of temperature by the x-ray powder diffraction method in the temperature range $18^{o}C$ -$867^{o}C$. The data has been used to evaluate the coefficients of thermal expansion α_a and α_c, at various temperatures by a graphical method. An attempt is made to explain the temperature dependence of the anisotropic thermal expansion and the tetragonal distortion of this compound, in terms of the thermal expansion of the bonds. A good correlation between DTA results (chapter 3) structure and the anisotropy of the thermal expansion behaviour of $CuGaSn\square Se_4$ was obtained.

4.2 Electron probe microanalysis (EPMA)

The EPMA results for the composition analysis of $CuGaSn\square Se_4$ single crystal are listed in table 4.1, which show the composition is $CuGaSn\square Se_4$ within experimental error. The result is consistent with the single-phase products from stoichiometric starting composition as proved by x-ray measurements.

TABLE 4.1

EPMA results for stoichiometric $CuGaSn\square Se_4$ in at %

Elements	Concentration observed	Concentration calculated
Cu	14.7	11.2
Ga	12.9	12.4
Sn	18.7	20.8
4Se	53.7	55.6
Total	100.0	100.0

4.3 Single crystal methods for crystal analysis of $CuGaSn\square Se_4$

Powder methods, reduce the three-dimensional variation of intensity of diffraction in reciprocal space to a one-dimensional variation with Bragg angle, and if the structure is at all complex this leads to great overlapping of the reflections, and non-observance of the weak ones.

In the simplest-crystal devices (rotation cameras and oscillation cameras) only the crystal is moved, and the three-dimensional variation of intensity in reciprocal space is represented two-dimensionally on the film. This gives a better resolution of the reflections than does the one-dimensional representation achieved by powder methods. In the Weissenberg and precision cameras both the crystal and the film (or detector) are moved. These achieve a three-dimensional representation of the three-dimensional variation of intensity of reflection in reciprocal space, and can thus be interpreted unambiguously.

In order to explain the basis of single-crystal methods, the concept of reciprocal lattice must be used. The reciprocal lattice is a representation of the crystal in which a family of parallel planes with indices, h k l, and interplanar spacing, d, is represented by a single point located at the end of a vector whose magnitude is a reciprocal function of the interplanar spacing i.e. $r^* = 1/d$ and whose direction is determined by the normal to the planes from the unit cell origin (40).

Ewald showed that a simple geometrical construction in reciprocal space gives the condition for reinforcement of the scattered waves in a way that expresses the condition for diffraction in terms of a sphere in reciprocal space, the reflection sphere, or Ewald's sphere. The sphere is drawn with a radius parallel to the incident beam, of

length λ^{-1}, where λ is the wavelength employed, and with the radius terminated at the origin 0 0 0 in the reciprocal lattice. The sphere is indicated in Fig 4.1, which represents a set of crystal planes at O having its reciprocal lattice point for first-order reflection at P, and an incident beam along QO. As reference to the figure will show:

$$\sin \theta = r^* \lambda/2 = \lambda/2d \qquad (4.1)$$

which is Bragg's law. The reflected ray lies in the plane containing Q, O, P and leaves the crystal at an angle of 2θ from the incident beam (41). A review of these single crystal methods is given by R. Rudman (40).

4.4 Rotation-crystal photograph

If the crystal is rotated about any axis, the reciprocal lattice accompanies it, and those reciprocal lattices within range pass through the reflecting sphere. Each time a reciprocal point cuts the sphere, a diffracted beam is developed in the radial direction. The sum total of all directions of reflection from a crystal with known reciprocal lattice, rotated about a given axis, can thus be visualized and calculated. The diffracted beams lie on the surfaces of co-axial cones. If the crystal is surrounded by a cylindrical film, the reflections will be recorded on circles which appear as straight lines when the film is laid out flat (fig. 4.2). Slight misorientation causes the spots to split up, the effect becoming more pronounced with increasing diffraction angle. This is a consequence of the fact that different quadrants of a reciprocal-lattice layer intersect the sphere of reflection at slightly different heights if the layer is not truly horizontal.

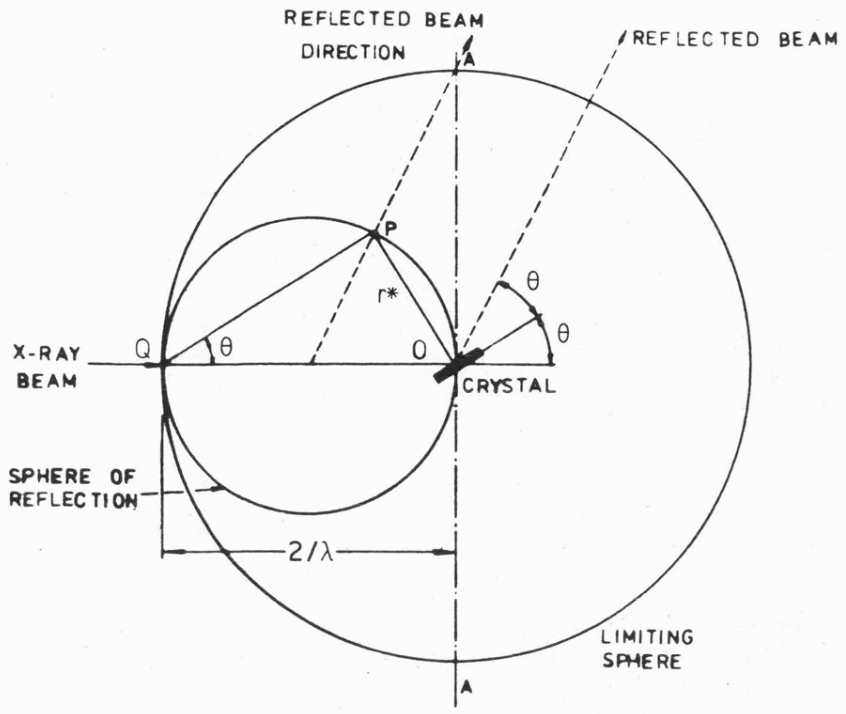

Fig. 4.1 Reflection sphere (Ewald's sphere) in a reciprocal lattice.

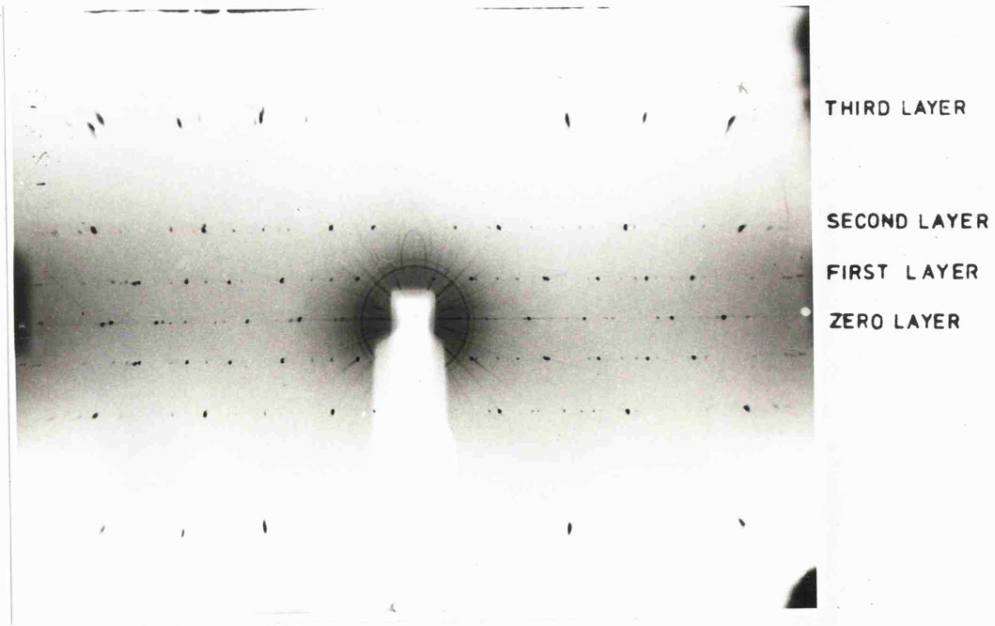

Fig. 4.2 Rotation photograph of $CuGaSn\square Se_4$.

Once the crystal is aligned, the repeat distance of the crystallographic direction along which the crystal is aligned can be calculated from the spacings between the rows of reflection. These rows of spots are known as layer lines, with the line through which the direct beam passes designated as the zero-layer line, fig. 4.2.

Suppose the crystal is rotated about the a-crystallographic-axis. The distance between the reciprocal-lattice planes is 1/a, and the radius of the sphere of reflection is λ^{-1}, the latitude of a layer line is (42)

$$\phi = \text{arc sin } (n\lambda/a) \qquad (4.2)$$

and hence the separation of this line from the equatorial line is given by

$$z = r \tan \phi = r\left(\frac{a^2}{n^2\lambda^2} - 1\right)^{-\frac{1}{2}} \qquad (4.3)$$

where r is the camera radius (28.65mm), n is the number of the level. The separation of layer lines on a rotation photograph, provides a ready means of determining the lengths of the crystal axes a, b, c. Greater accuracy is obtained by measuring the distance between the layer lines corresponding to +n and -n, rather than the separation between the equator and one of these lines.

The Bernal chart was used to measure the film. The results for $CuGaSn\square Se_4$ of the rotation photograph are:

First level (n=1) sin ϕ_1 = 0.275, thus give us a = 5.608 ^{o}A

Second level (n=2) sin ϕ_2 = 0.55, thus give us a = 5.608 ^{o}A

Third level (n=3) sin ϕ_3 = 0.825, thus give us a = 5.608 ^{o}A

This value is in very good agreement with that obtained in the powder photograph a = b = 5.611 ^{o}A.)See table 3.1).

4.5 Weissenberg photographs

The oscillation method is particularly suitable for determination of cell size. But this method has a limitation that loss of information caused by the projection of planes of reciprocal-lattice (points onto lines). In a Weissenberg method only a particular set of reflections, such as 0 k l, or 1 k l, etc., are allowed to fall on the film, and these are spread out over the film in such a way that to each point on the photograph there corresponds a single value of k and a single value of l.

The instrument consists of a mechanism for translating the film cassette which is coupled to the oscillation mechanism such that a given section of the film is in the same position each time a given reflection occurs. A layer line screen (i.e. a slotted cylinder which fits over the goniometer head and crystal, but inside the film cassette) is adjusted so that the reflections from only one plane of reciprocal-lattice points (corresponding to a single layer line on the rotation photograph) can pass through the slot. In this manner a distorted reciprocal-lattice plane is recorded on the film.

The intensity of any reflection obtained from a given crystal is usually not evenly distributed over the entire spot as it appears on the film. However, in order to obtain reliable intensity data one must determine the intensity of the complete spot (integrated intensity), not just that of the darkest portion of the spot (peak height). This integrated intensity is achieved with an integrating Weissenberg goniometer. The film cassette is translated in a direction normal to the beam. When it reaches the end of its translation it trips a lever which causes the film cassette to change its position on the support. The mechanism is arranged so

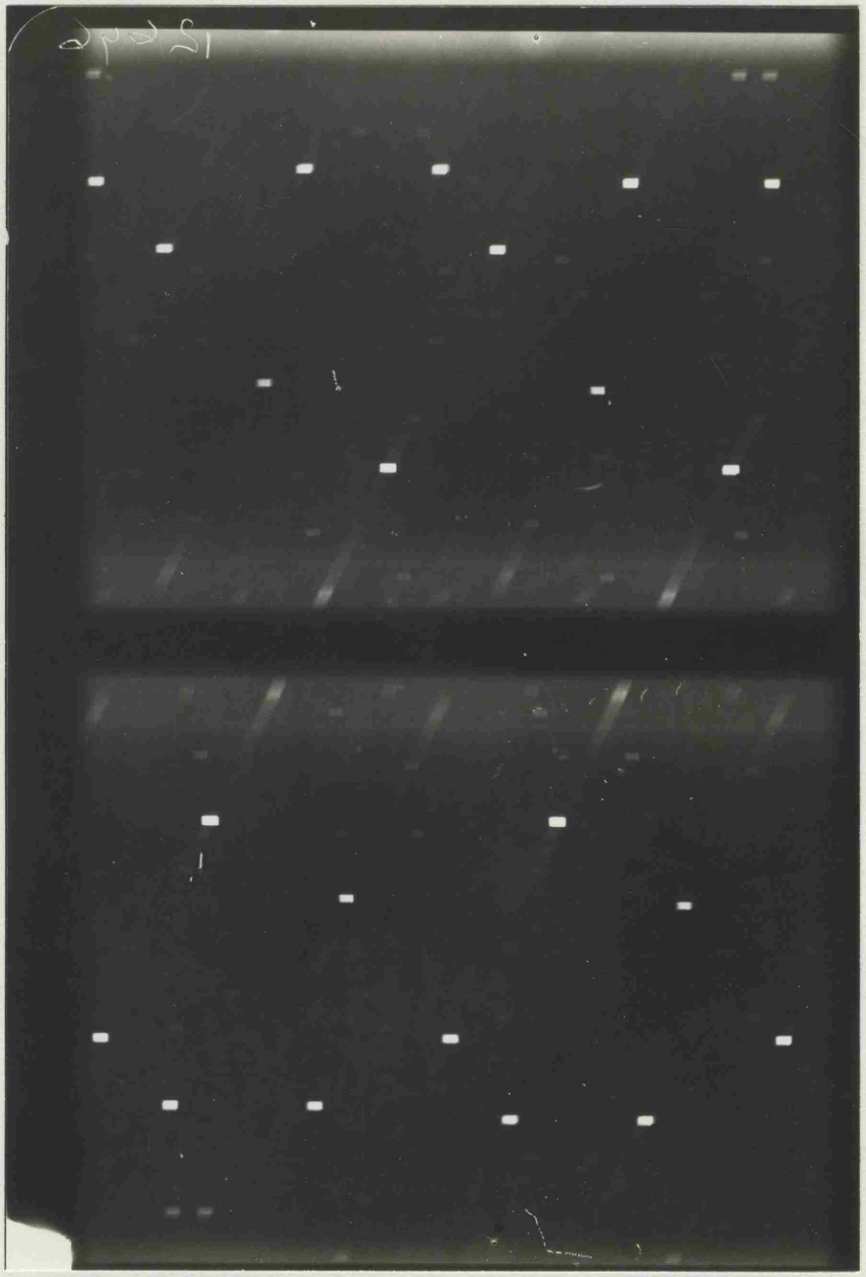

Figure 4.3 Zero-level Weissenberg photograph of $CuGaSn\square Se_4$

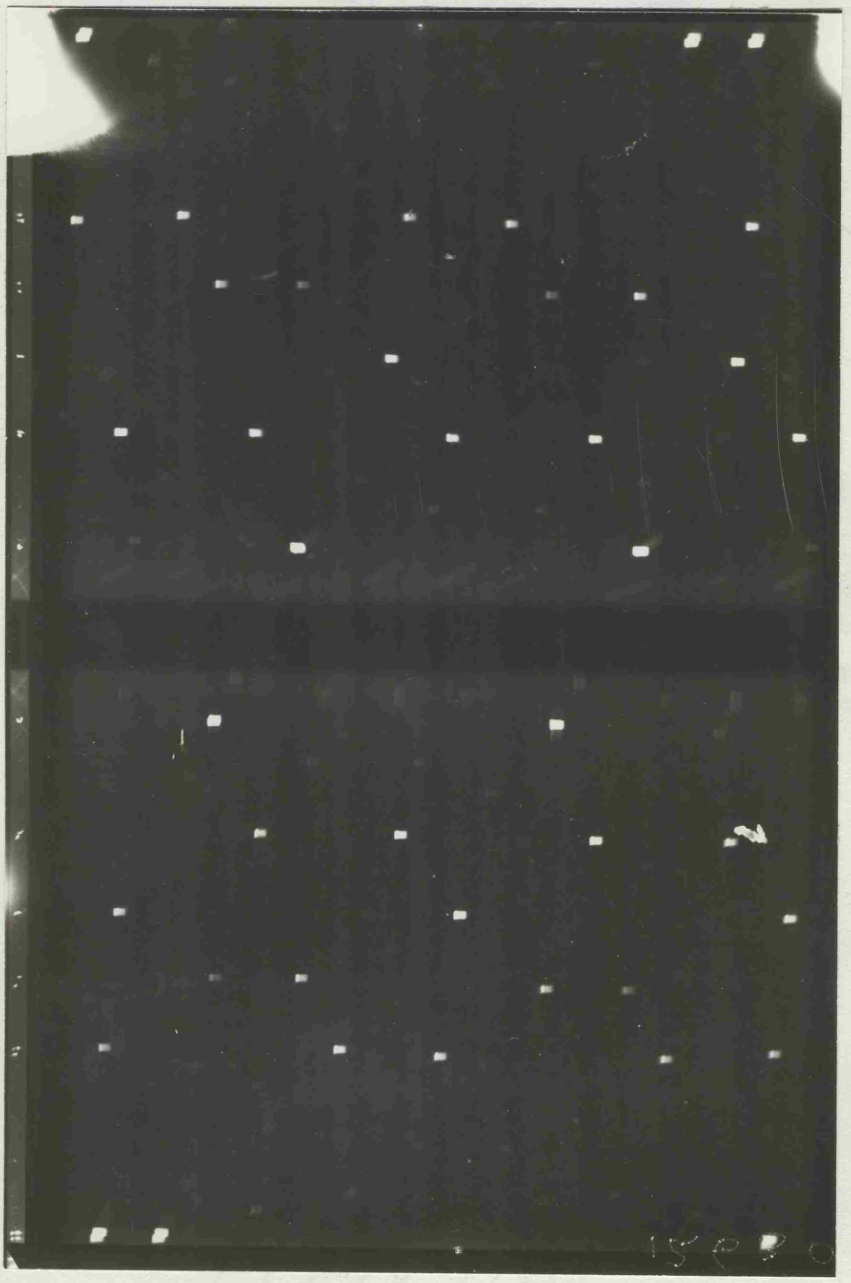

Figure 4.4 First-level Weissenberg photograph of $CuGaSn\square Se_4$

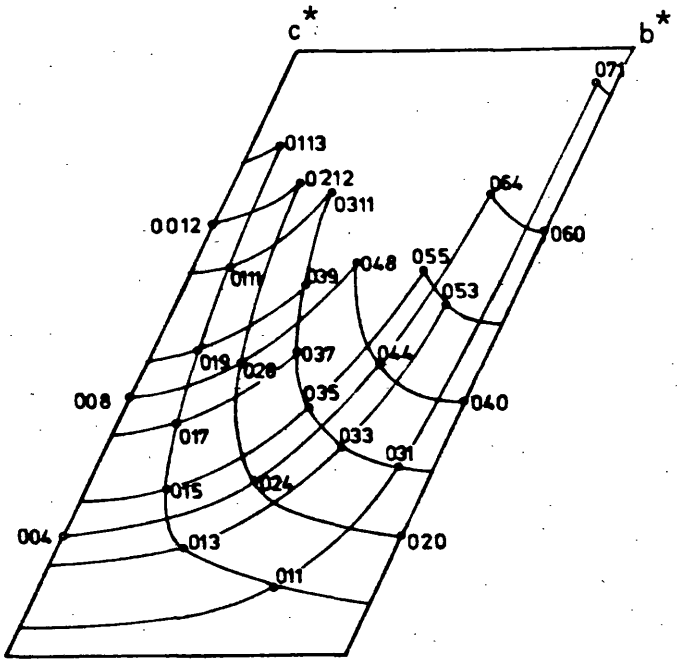

Fig. 4.5 Indexed pattern of the Weissenberg photograph of $CuGaSn\square Se_4$ (zero-level).

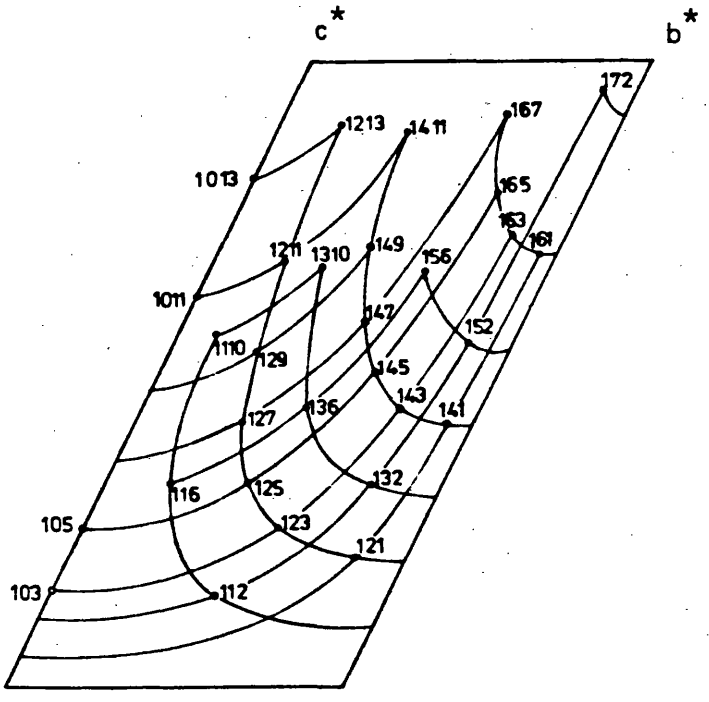

Fig. 4.6 Indexed pattern of the Weissenberg photograph of $CuGaSn\square Se_4$ (First-level)

that all the portions of a reflection are superimposed on one small section of the film. This section contains the integrated intensity and by measuring the optical density of this spot one determines the integrated intensity of the reflection. Figure 4.3 shows the zero-level photograph and figure 4.4 the first-level photograph of a $CuGaSn\square Se_4$ crystal rotated about its 'a' axis. Both photographs were prepared using Cu K_α radiation (λ = 1.5418 Å). Figure 4.5 and 4.6 show the indexed patterns of the zero and first-level Weissenberg photographs.

Measuring the distance between the spots for the b^* and c^* axes and given that the cylindrical camera is of diameter 57.3mm, the lattice parameters are calculated to be b = 5.607Å and c = 10.989Å which are in very good agreement with the values obtained with the powder method (b = 5.611Å and c = 10.988Å, see table 3.2). These Weissenberg photographs give a distorted map of a reciprocal lattice layer which can be translated back to the actual reciprocal lattice layer. This operation presents little difficulty, but when the unit cell has one long axis, this process can lead to errors. If a number of adjacent spots are too weak to be seen in an otherwise highly populated row corresponding to a line of reciprocal lattice points, then it is possible to mixindex the higher-order reflections. This can be caused by very slight mispositioning of the Weissenberg chart on the photograph. In order to detect any possible error in the indexing of the Weissenberg photographs, the precision camera was used.

4.6 Precession photographs

The precession method provided a simple and direct way of establishing the space group and unit cell of the crystal.

The precession camera is an instrument designed to photograph the reciprocal lattice of a single crystal directly and without distortion. The principle of operation was developed by M.J.Buerger, who built the first instrument, it is described in his monograph (43) and in more detail in his book (44). It combines two oscillation motions, one about a vertical axis and the other about a horizontal axis. When a zero level reciprocal lattice plane is photographed, this plane is first oriented so that it is perpendicular to the x-ray beam when the crystal is in an untilted position. To cause diffractions in this net plane, the crystal is oscillated as in the oscillation method so that it will penetrate the sphere of reflection an equal amount on both sides of the origin, a second oscillation is added at right angles to the first of equal magnitude and 90^{o} out of plane. Two oscillations so combined result in the fact that the plane being photographed, always maintains a constant angle ($\bar{\mu}$), with the x-ray beam, (see fig. 4.7). This normal thus travels in a circular manner about the x-ray beam, sweeping out a cone, a motion described as precession.

The lattice plane by this arrangement always has a constant tilt with respect to the x-ray beam, and therefore always intersects the sphere of reflection in a circle of constant diameter. Diffraction beams from points in this plane thus follow elements of a right circular cone whose apex is in the crystal. Other upper

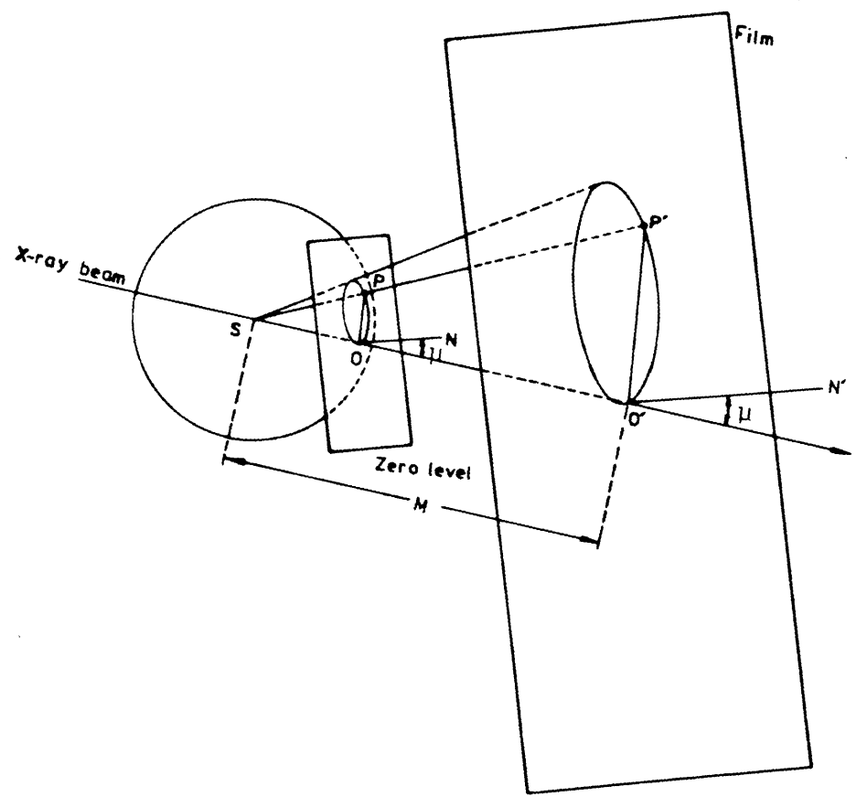

Fig. 4.7 Diffraction by a point P in a zero-level plane of the reciprocal lattice (Ref. 44).

level planes will produce cones of larger angle, coaxial with this zero level cone. A screen containing an annular opening is placed behind the crystal in such a way that only one of these cones will pass through and reach the film. Depending upon $\bar{\mu}$ and the level being photographed the screen-to-crystal distance will be varied and annuli of different radius will be used.

A flat photographic film placed behind the layer screen is tilted so that it is exactly parallel to the reciprocal plane being photographed, and then caused to pass through exactly the same motions as the crystal. The centre of this motion lies on the x-ray beam axis, a certain fixed distance behind the crystal. The cone of diffraction then forms continuously a circular trace on the film exactly similar to the circle in the reciprocal plane cut by the reflection sphere. In photographing various planes, a three-dimensional reciprocal lattice may be imagined constructed in space according to the orientation of the crystal, but with the centre of precession of the film as origin, and with a scale proportional to the film-to-crystal distance M.

Figure 4.8 shows the zero-level of CuGaSn□Se_4 crystal, photographed with filtered Mo K_α radiation with precession angle $\bar{\mu} = 30^\circ$, screen distance 26mm and the crystal-to-film distance 60mm and screen radius 15mm. Figure 4.9 shows the first-level, recorded with $\bar{\mu} = 30^\circ$, screen distance 27.4mm, screen radius 25mm, fig. 4.10 the second-level, recorded with $\bar{\mu} = 30^\circ$, screen distance 19.4 and screen radius 25mm and the figure 4.11 shows the superposition of the zero, first and second-levels of the spots in the precession photographs. The symmetry of the plane (b*c*) of the reciprocal lattice is shown very clearly in this figure.

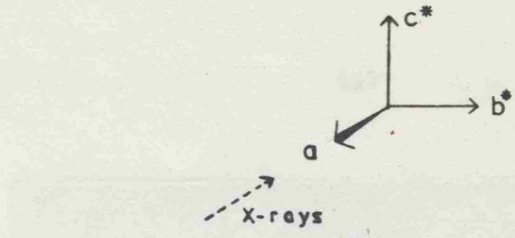

(a)

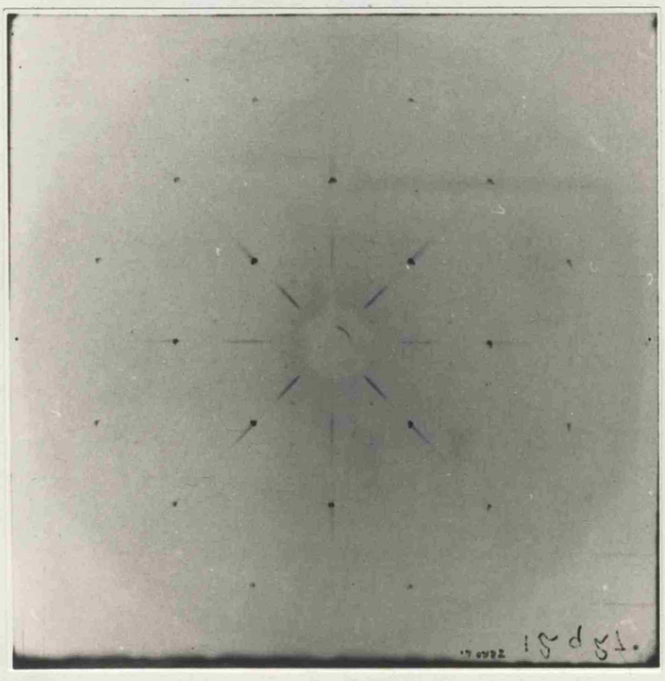

(b)

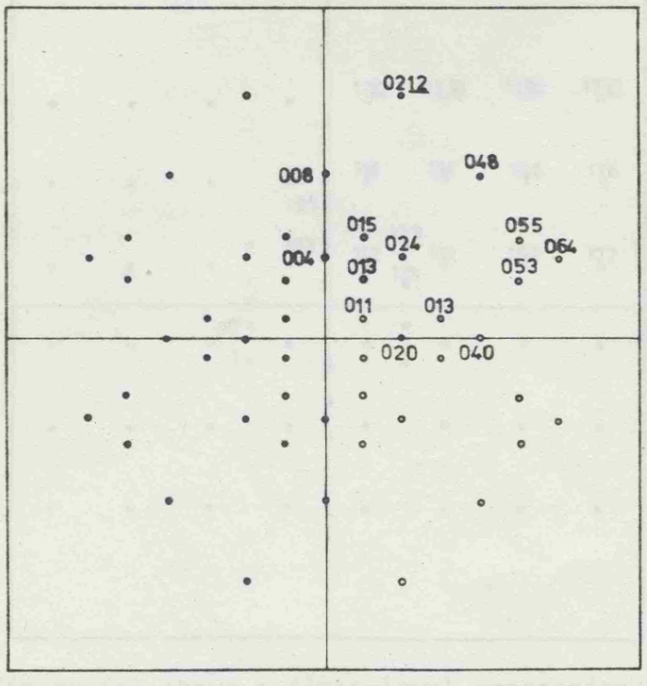

Fig. 4.8 Figure (a) shows a zero-level precession photograph of $CuGaSn\square Se_4$ and figure (b) a partially indexed pattern of this photograph (two-thirds natural size).

(a)

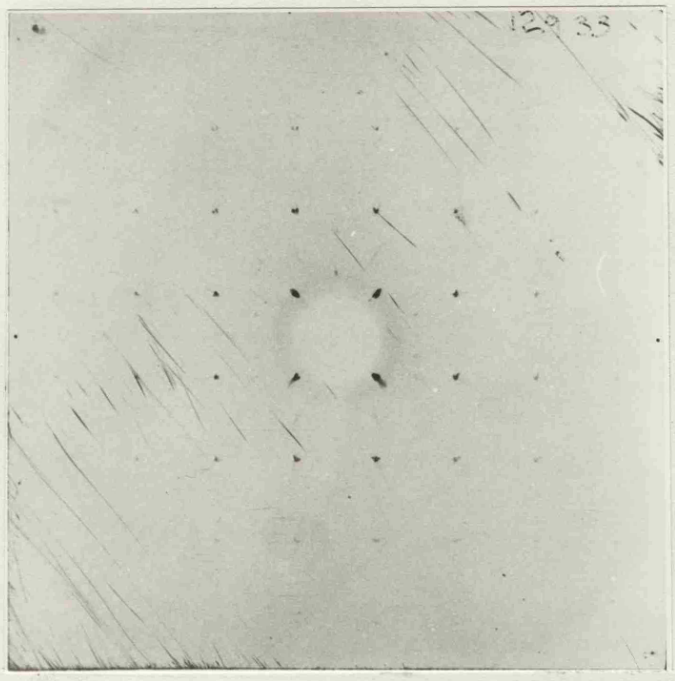

(b)

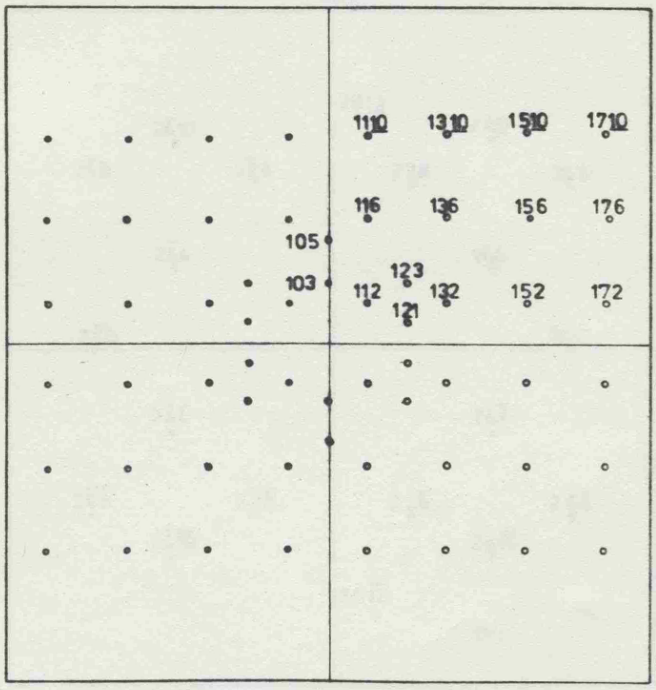

Fig. 4.9 Figure (a) shows a first-level precession photograph of $CuGaSn\square Se_4$ and figure (b) a partially indexed pattern of this photograph. (Two-thirds natural size).

(a)

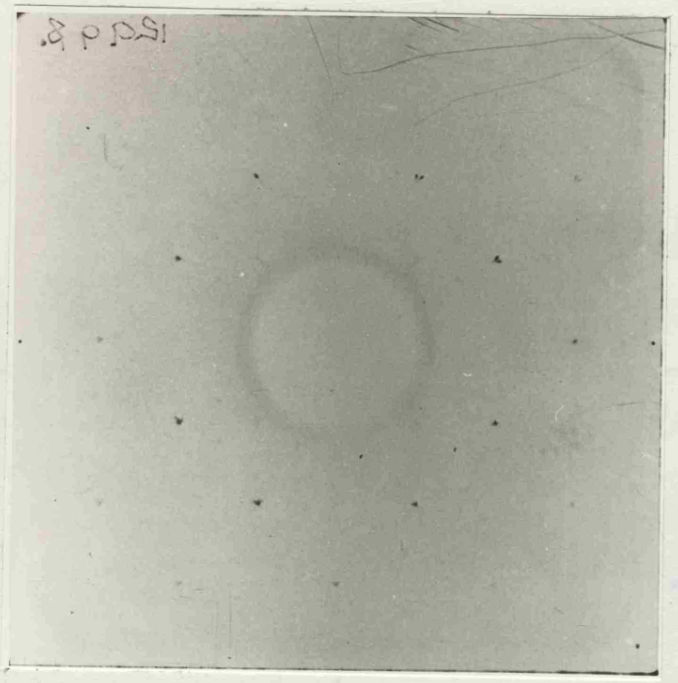

(b)

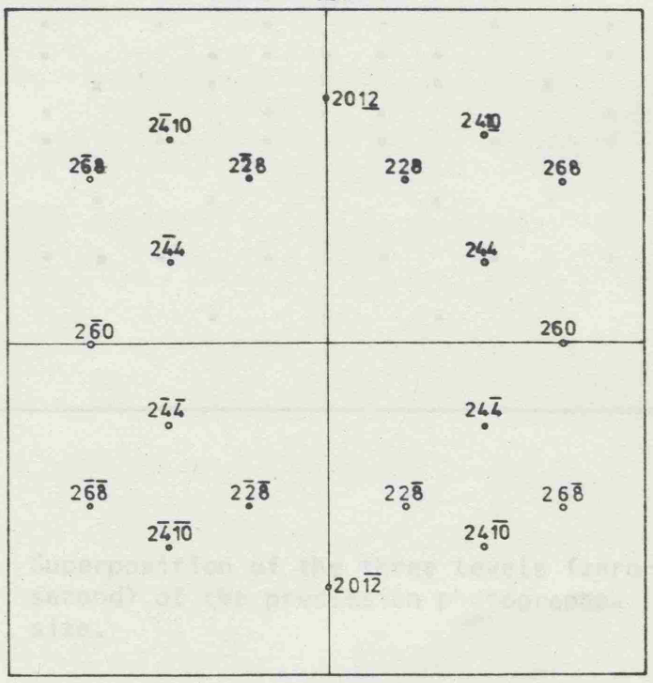

Fig. 4.10 Figure (a) shows a second-level photograph of $CuGaSn\square Se_4$ and figure (b) an indexed pattern of this photograph (two thirds natural size).

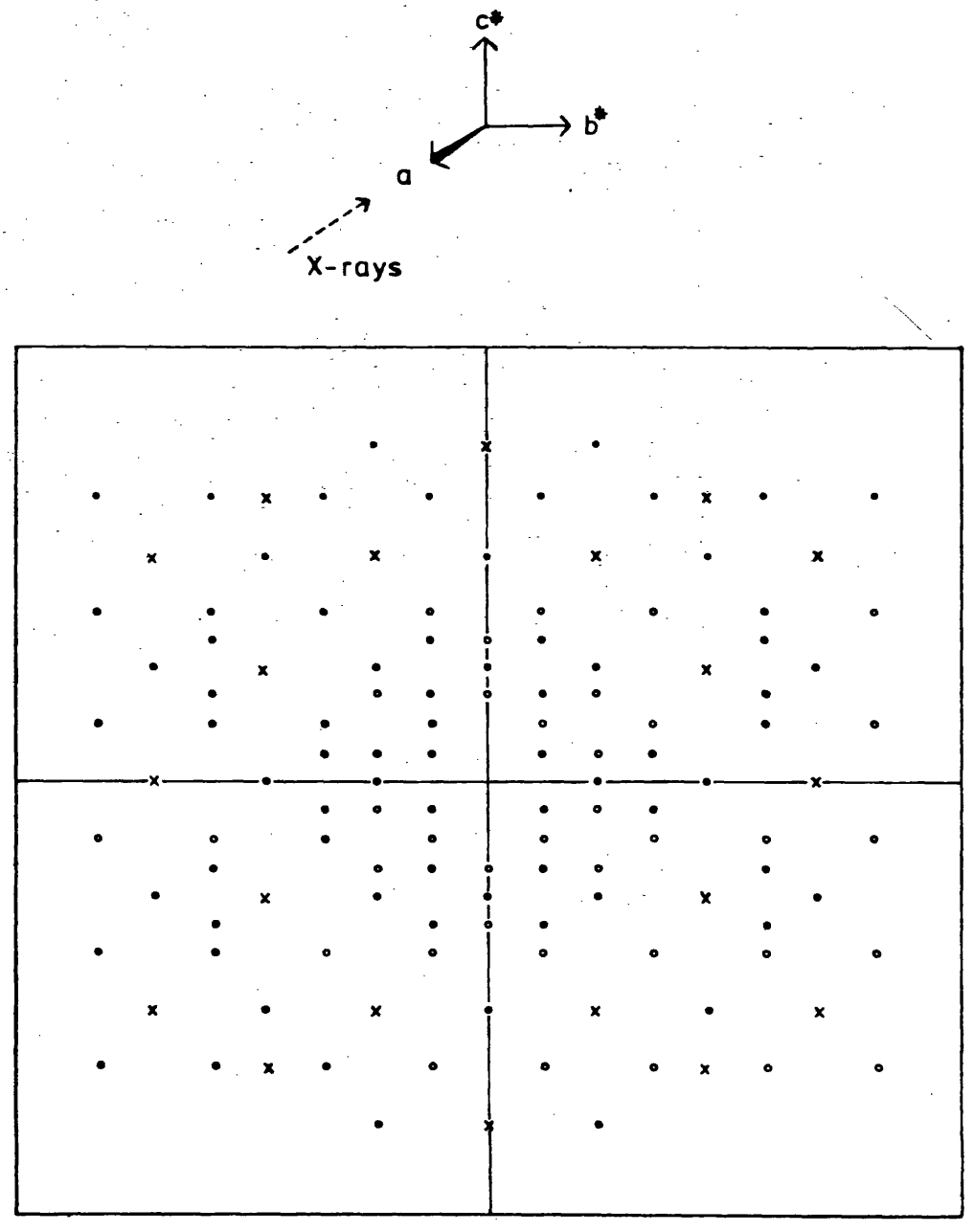

Fig. 4.11 Superposition of the three levels (zero-first and second) of the precession photographs. Natural size.

All the translational and angular dimensions of the reciprocal lattice can be made directly on the precession films. These measurements are converted to reciprocal lattice units from the fundamental reciprocity relations.

$$b^* = \frac{x}{M\lambda} \qquad (4.4)$$

$$c^* = \frac{y}{M\lambda} \qquad (4.5)$$

where x is the horizontal distance, y is the vertical distance measured on the film, M is the film-to-crystal distance (60mm) and λ is the wavelength of the M_o K_α radiation (0.7107 Å). The lattice parameters are calculated to be b = 5.6108 Å (x = 7.60mm) and c = 11.004 Å (y = 3.875mm). These values are in very good agreement with the measurement obtained by the other methods within experimental error. The best accuracy that can be expected, limited mainly by film shrinkage, is about 3 parts in 1000. Cross comparison between the Weissenberg and precession photographs gave the same results of indexed and intensity of the distorted and undistorted reciprocal lattice obtained by these two methods.

4.7 Structure analysis of $CuGaSn\square Se_4$

X-rays are scattered solely by electrons. This means that the data derived from x-ray diffraction patterns (Weissenberg and precession photographs) can only relate to these electron density distributions in the crystal. Crystal structure analysis consists in finding a structure whose diffraction spectra and calculated intensity match the observed set and observed intensity. The angular positions at which scattered x-rays are observed depends only on the dimensions of the crystal lattice, while the intensities of the different diffracted beams depend on the nature and arrangement of the atoms within each cell and possible corrections (geometric factors,

thermal vibration, absorption) (45).

The Weissenberg and precession photographs could be indexed with a tetragonal unit cell. Reflections only for h k l with h+k+l = 2n and for h h l with 2h+l = 4n, consistent with the chalcopyrite structure space group assignment of $I\bar{4}2d$ (D_{2d}^{12}) (this result is in agreement with powder x-ray analysis section (3.3).

The lattice constants of this tetragonal crystal determined by x-ray powder, rotation, Weissenberg and precession methods as a = 5.611(Å) and c = 10.984(Å). The volume of the unit cell is 345.690(Å^3). The density of the material is 5.42 gm-cm^{-3} the formula-units per unit cell can be calculated to be 2. The different ways of ordering the Cu, Ga and Sn atoms with the vacancy in the defect chalcopyrite structure was investigated. Intensity measurements were made on 43 different diffraction spots, h k l, and compared with calculations of the x-ray 76 computer programme (46) for the three possible defect chalcopyrite structures. The integrated intensities were corrected for Lorentz, and absorption factors.

The procedure used to refine the structure model for $CuGaSn\square Se_4$, in which the A stom (Cu and Ga at random) is placed at 0 0 0, the B atom (Sn and □ at random) at 0 0 $\frac{1}{2}$, and Se atom at x $\frac{1}{4}$ $\frac{1}{8}$, with x given by the regular tetrahedral B atom condition (48).

$$x_{calc} = \frac{1}{2} - (1/4\sqrt{2})(c^2/a^2 - 2)^{\frac{1}{2}} \qquad (4.6)$$

was used, resulting in an initial value of x = 0.2606. the function minimized was

$$R_1 = \Sigma w(|F_{obs}| - |F_{calc}|)^2 \qquad (4.7)$$

where Σ is over all the non-equivalent observed reflections listed with each test, and w is the weight. The weighting factor of all

the reflections was given unity. The anisotropic temperature coefficients are given in table 4.2 and the resulting value of x is given in table 4.3

TABLE 4.2

Anisotropic temperature coefficients in $CuGaSn\square Se_4$ at room temperature

Atom	β_{11}	β_{22}	β_{33}	β_{12}	β_{12}	β_{12}
$\frac{1}{2}$(Cu+Ga)	0.02381	0.02381	0.00620	0	0	0
$\frac{1}{2}$(Sn+□)	0.02381	0.02381	0.00620	0	0	0
Se	0.01984	0.01984	0.00517	0	0	0

TABLE 4.3

Atomic position coordinates of $CuGaSn\square Se_4$ (ABX_2) at room temperature

Atom	x	y	z
A=Cu and Ga at random in (a)	0	0	0
B=Sn and □ at random in (b)	0	0	$\frac{1}{2}$
C=Se in (d)	x	$\frac{1}{4}$	$\frac{1}{8}$
x(Se) = 0.2571			

In table 4.4 are compared the observed F values with the |F| values calculated for the final structure proposal. The discrepancy index is defined as

$$R = \frac{\Sigma[|F_{obs}| - |F_{calc}|]}{\Sigma|F_{obs}|} \qquad (4.8)$$

Using the values of table 4.4 the R value was found to be 0.04 after 7 cycles. It is important to point out that this value should be decreased if the multiple film technique is used and calibrated by comparison with calibrated film strip.

4.8 High temperature lattice parameters and thermal expansion of $CuGaSn\square Se_4$

As mentioned in section 3.4, DTA measurements have shown a peak at 590°C which has been associated with decomposition of the quaternary into two phases. A high temperature x-ray camera was employed to determine the change of the structure at this temperature.

The camera was a 19cm Unicam 5150 high temperature powder camera with Van Arkel film mounting. With this arrangement the film is in two sections, one on each side of the x-ray beam, the θ values of the images of pins located in front of the films were calibrated first of all by four measurments of α-Al_2O_3 at room temperature. Powdered $CuGaSn\square Se_4$ was then sealed in a silica tube of 0.3mm in diameter which was mounted in the centre of the camera. Heating was by radiation from heated elements surrounding the cavity, and a thermocouple placed near the sample recorded the temperature. Exposures were made at 100°C intervals up to 863°C, that is, 73°C below the melting point. At the temperature of 590°C extra lines appeared at θ values of 15.3133°, 18.8235°, 21.0230°, 24.5633°, 26.3712°, and 34.7926°. These new extralines (second phase) are

TABLE 4.4

COMPARISON OF OBSERVED AND CALCULATED RELATIVE WEISSENBERG X-RAY INTENSITIES FOR $CuGaSn\square Se_4$

h k l	Observed Intensity	Calculated Intensity	h k l	Observed Intensity	Calculated Intensity
0 0 8	245.1	276.6	1 1 10	137.4	156.8
0 1 1	10.2	7.6	1 2 1	22.8	18.6
0 1 3	20.9	17.2	1 2 3	17.2	11.3
0 1 5	17.7	15.7	1 2 5	10.3	8.9
0 1 7	> 8.7	6.3	1 2 7	19.7	13.6
0 1 9	>11.1	4.3	1 2 9	15.6	11.2
0 1 11	10.2	8.0	1 2 13	3.1	3.2
0 1 13	12.3	7.6	1 3 2	201.7	236.7
0 2 4	423.1	350.7	1 3 6	262.8	194.6
0 2 12	245.8	184.7	1 3 10	153.6	140.7
0 3 1	16.8	22.5	1 4 3	14.4	17.7
0 3 7	27.7	25.3	1 4 5	18.9	15.0
0 4 0	287.1	304.2	1 4 7	15.0	13.0
0 5 3	25.3	18.9	1 4 9	7.9	8.0
0 5 5	27.8	19.8	1 4 11	9.3	11.1
0 6 4	300.8	209.8	1 5 2	135.9	179.9
1 0 3	17.5	17.2	1 5 6	157.2	154.0
1 0 5	16.4	15.8	1 6 1	13.5	16.4
1 0 11	7.5	8.0	1 6 3	9.2	16.0
1 0 13	8.8	7.1	1 6 5	7.6	12.5
1 1 2	245.6	294.1	1 7 2	118.5	113.8
1 1 6	207.5	225.7			

probably from $SnSe_2$.

The lattice parameters were calculated as described in section 3.3 and the results are shown as a function of temperature in figure 4.12. Agreement with room temperature results of section 3.3, were within ± 0.002 Å for the values of the lattice parameters. The 'a' and 'c' parameter increases linearly with temperature within experimental error. In figure 4.13, axial ratio c/a and unit-cell volume (V), derived from the lattice parameters versus temperature data are plotted against temperature.

In table 4.5, the thermal expansion coefficients are given, these values were obtained by the best straight linefits to the data. These are thus average coefficients for the temperature ranges covered and are normalised by dividing by the room temperature values.

TABLE 4.5

Average thermal expansion coefficients

Material	$\frac{1}{a_o}\frac{da}{dT} = \alpha_a$	$\frac{1}{c_o}\frac{dc}{dT} = \alpha_c$	$\frac{1}{(c/a)_o}\frac{d(c/a)}{dT}$	$\frac{1}{V_o}\frac{dV}{dT}$
$CuGaSn\square Se_4$	$1.74\times10^{-5}(^oC^{-1})$	$8.79\times10^{-6}(^oC^{-1})$	$8.58\times10^{-6}(^oC^{-1})$	$4.33\times10^{-5}(^oC^{-1})$
$CuGaSe_2$	$1.31\times10^{-5}(^oC^{-1})$	$5.2\times10^{-6}(^oC^{-1})$		
Thermal expansion coefficients are defined by, $\alpha_i = \frac{1}{\xi_o}\cdot\frac{d\xi_i}{dT}$ where ξ_o is the room temperature value.				

Since the variation of 'a' and 'c' parameter with temperature is linear, the coefficient of thermal expansion, α_a and α_c, remains constant throughout the range of temperature studied. The values for $CuGaSe_2$ (47), the ternary analogue of $CuGaSn\square Se_4$, are listed for

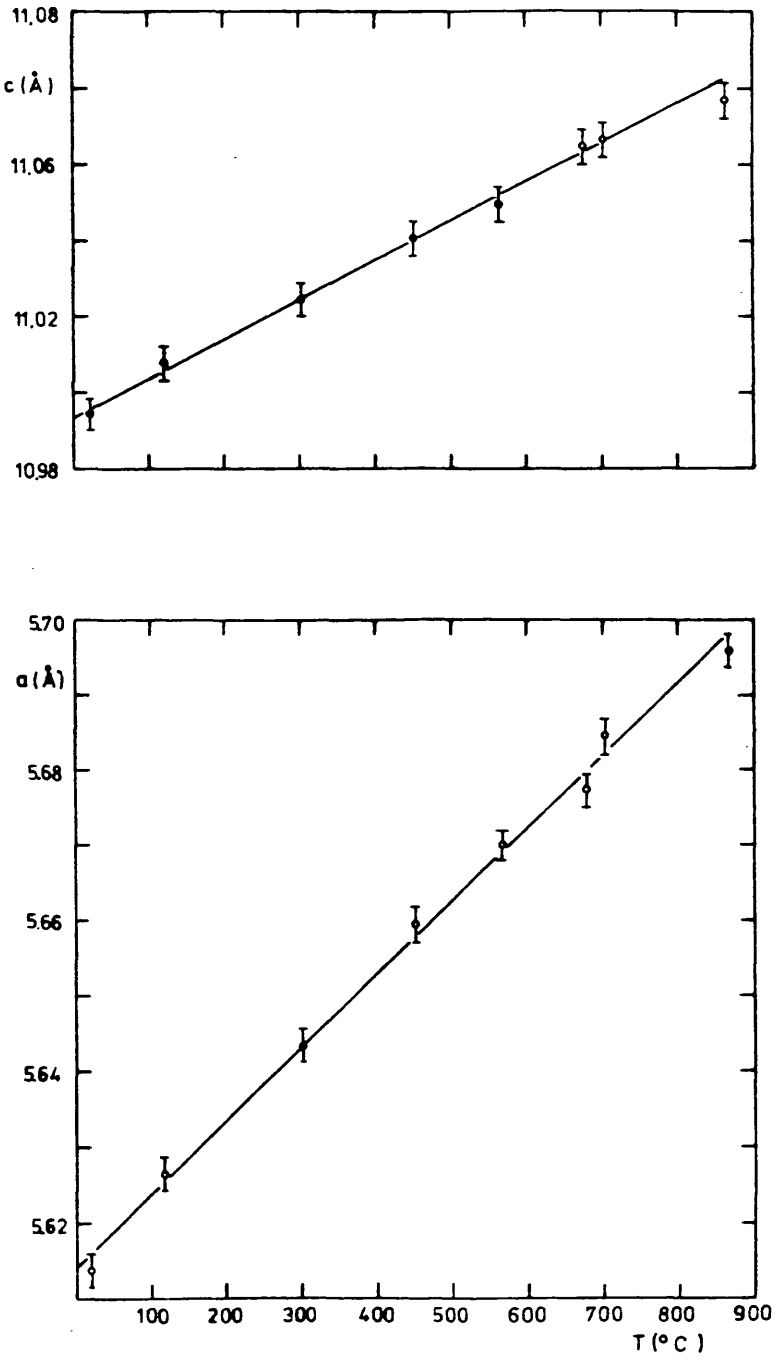

Figure 4.12. Temperature dependence of the lattice parameters of $CuGaSn\square Se_4$.

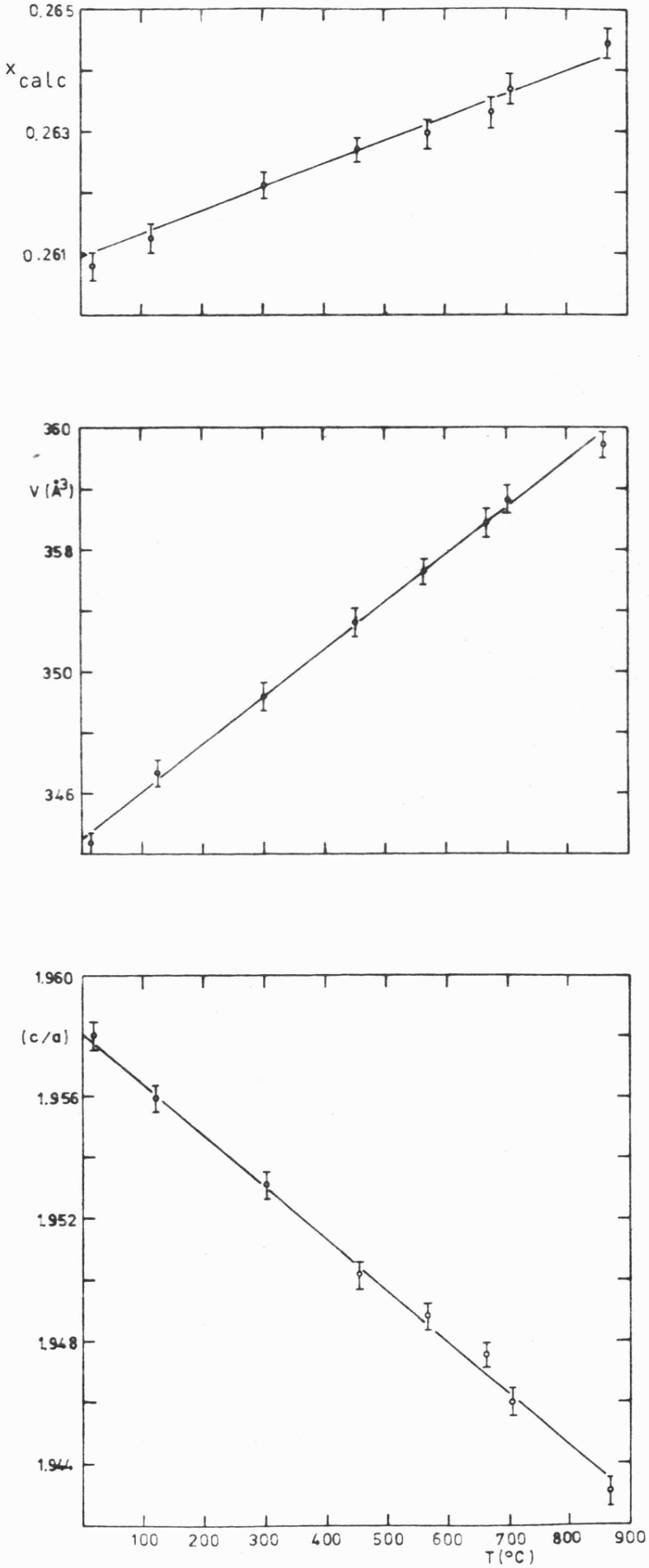

Fig. 4.13 Variation of calculated x parameters, unit-cell volume (V), and axial ratio (c/a) of $CuGaSn\square Se_4$ with temperature.

comparison and are seen to be significantly smaller.

The x parameter was calculated from 'a' and 'c' values, equation 4.6. The variation of the calculated x parameter with temperature is shown in figure 4.13. In section 4.7 the x parameter was given from the crystal structure analysis as 0.2571 at room temperature, which is to be compared to the calculated room temperature value of 0.2606.

The anisotropy in the thermal expansion of $CuGaSn\square Se_4$ is marked by having a larger coefficient of expansion along a-axis (α_a) than that along c-axis (α_c). In order to explain this anisotropy of the thermal expansion coefficients of this compound, we have attempted to estimate the bond distances and bond expansion coefficients for A-Se (where A is Cu and Ga randomly distributed) bonds and B-Se (where B is Sn and □ randomly distributed) bonds by applying the Abrahams and Bernstein relations (48) to our results, as described by Miller et al (49) on $II\text{-}IV\text{-}V_2$ group of compounds. The bond lengths from geometry are:

$$A - S_e = \left[a^2x^2 + \frac{4a^2+c^2}{64}\right]^{\frac{1}{2}} \qquad (4.9)$$

$$B - S_e = \left[a^2(\tfrac{1}{2}-x)^2 + \frac{4a^2+c^2}{64}\right]^{\frac{1}{2}} \qquad (4.10)$$

The bond lengths given by this approximation are shown in figure 4.14 plotted as functions of temperature. The coefficients of thermal expansion of the A-Se bond was calculated to be $2.08 \times 10^{-5}\ {}^{o}C^{-1}$ and that of the B-Se bond $8.74 \times 10^{-6}\ {}^{o}C^{-1}$. It is interesting to compare this last value of α_{B-Se} coefficient of thermal expansion with $\alpha_{B-Se} = 5.2 \times 10^{-6}\ {}^{o}C^{-1}$ in the ternary analogue $CuGaSe_2$ (47) this value is nearly half of α_{B-Se} of $CuGaSn\square Se_4$. This effect may be

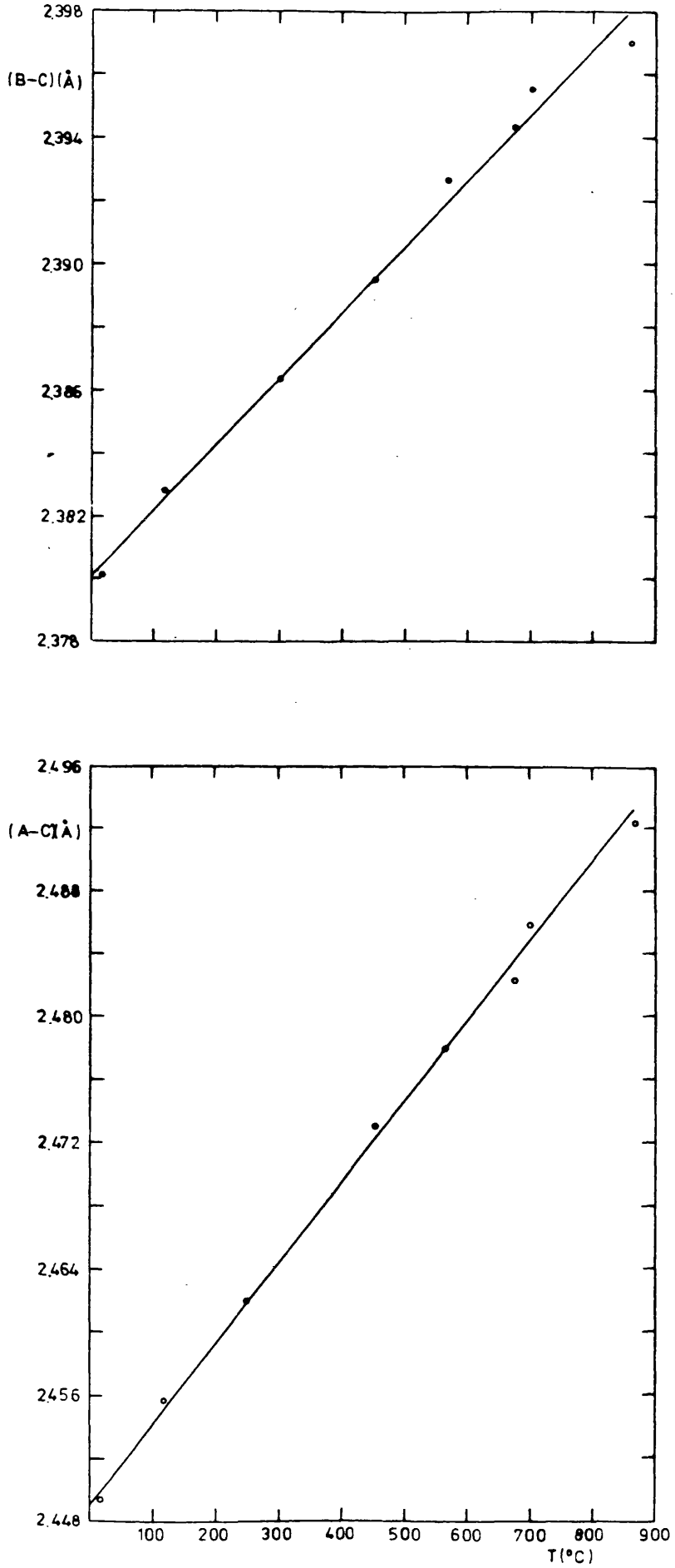

Figure 4.14. Calculated thermal expansions of the B-C and A-C bonds. (C is Se atom).

due to the weak bonding between B and Se in the quaternary compound, because the site B in this defect structure is populated randomly with equal numbers of atom of tin and vacancy: (B = $\frac{1}{2}$ (Sn+□)).

Covalent bonds are strong short range forces which characteristically have low coefficients of thermal expansion, whereas ionic bonds have much longer range. For example, the mean coefficient of thermal expansion of Si between 0 and 600°C is $2.0 \times 10^{-6}\ ^{o}C^{-1}$ (50) while that of NaCl is about $50 \times 10^{-6}\ ^{o}C^{-1}$ (51).

The tetragonal distortion in the chalcopyrite structure is defined as

$$\Delta = 2 - c/a \qquad (4.11)$$

From the equation 4.11 it follows that the change of Δ with temperature T should follow the relation

$$\frac{d\Delta}{dT} = \frac{c}{a}\left(\frac{1}{a}\frac{da}{dT} - \frac{1}{c}\frac{dc}{dT}\right) \qquad (4.12)$$

From equation (4.12) it follows that the temperature coefficient $d\Delta/dT$ of the tetragonal distortion Δ can be calculated from the linear expansion coefficients α_a and α_c as

$$\frac{d\Delta}{dT} = \frac{c}{a}(\alpha_a - \alpha_c) \qquad (4.13)$$

Replacing the experimental values of α_a, α_c and c/a in equation 4.13, a value of $d\Delta/dT = 1.69 \times 10^{-5}\ ^{o}C^{-1}$ is expected for $CuGaSn\square Se_4$.

These results confirm the close correlation between structure DTA and the anisotropy of the thermal expansion behaviour of $CuGaSn\square Se_4$.

CHAPTER 5

OPTICAL PROPERTIES OF I-III-IV-□-VI_4 SEMICONDUCTORS

5.1 Introduction

One of the most powerful tools for studying the properties of solids is the measurement and analysis of their optical properties. In the first part of this chapter some of the results required for such an analysis are presented, with emphasis on the detailed development of the structure of the optical constants at critical points, (or Van Hove singularities).

The fundamental absorption edge of semiconductors corresponds to the threshold for electron transitions between the highest nearly filled valence band and the lowest nearly empty conduction band. The study of the fundamental absorption provides information about electron states near the band extrema. By studying the spectral dependence of the absorption coefficient one can distinguish between direct and indirect transitions, and can calculate the energy gap. The experimental technique which was used for the optical experiments will be described. In table 5.3 the experimental values for the energy gaps are given for the quaternary compounds. In table 5.4 will be given the values for four quaternary normal adamantine compounds; these values are taken from the paper by D.M.Schleich and A.Wold (64). It is interesting to point out that these are the only values of energy gaps known up till now of this large family of quaternary adamantine compounds.

The reflection coefficient provides much information about the position and nature of the energy bands in $CuGaSn□Se_4$. The interpretation of the data is aided by the existence of definite family relationships between materials having similar crystal

structure & outer electronic configurations. We have observed in the structure of the reflectivity spectrum three transitions E_A, E_B and E_C that characterise the chalcopyrite materials because of the crystal field and spin-orbit splitting of the Γ_{15} valence bands of zincblende. The E_A, E_B and E_C versus T curves consist of a near-linear sloping part above 190 K, a bending part at their intermediate temperature region and a near leveling-off part at lower temperatures. There are two kinds of contribution to this effect: one is due to the effect of volume thermal expansion of the crystal, and the other arises from the electron-phonon interaction in the crystal. Also the variation of the Δ_{cf} and Δ_{so} are given in table 5.6 and figure 5.13.

5.2 Properties of the optical constants (direct transitions)

Optical techniques have provided much information about the position of energy bands and the symmetry of their associated wave functions in a large number of materials.

The optical properties of a solid may be conveniently discussed in terms of complex dielectric constant $\varepsilon(\omega) = \varepsilon_r + i\varepsilon_i$. The interband contribution to $\varepsilon(\omega)$ is produced by direct transitions if imperfections (phonons, defects, etc) are neglected. $\varepsilon_i(\omega)$ the imaginary part of the dielectric constant may be expressed in terms of energy band parameters (52):

$$\varepsilon_i(\omega) = \frac{4\pi^2 e^2}{m^2\omega^2} \sum_{v,c} \int_{BZ} \frac{2\underline{dk}}{(2\pi)^3} |\underline{e}.\ \underline{M_{vc}}|^2\ \delta(E_c - E_v - k\omega) \quad (5.1)$$

where ω is the frequency of the incident optical radiation, e and m are the electronic charge and mass. The matrix element is the usual one for electric dipole transitions:

$$\underline{e} \cdot \underline{M_{vc}} = \langle \psi_{ck} | \underline{e} \cdot p | \psi_{vk} \rangle = \underline{e} \cdot \int_V \psi_c^*(\underline{k},\underline{r})(-ih\underline{\nabla})\psi_v(\underline{k},\underline{r})\underline{dr} \qquad (5.2)$$

V is the volume of the crystal. The sum in equation (5.1) is over all occupied valence bands with energy $E_v(k)$ and wave function ψ_{vk} and all unoccupied conduction bands with energies $E_c(k)$ and wave function ψ_{ck}. The real and imaginary parts of the dielectric constant are related by the Kramers-Kronig relation: (53)

$$\varepsilon_r(\omega) = 1 + \frac{2}{\pi} P \int_0^\infty \omega' \varepsilon_i(\omega') \frac{d\omega'}{\omega'^2 \omega^2} \qquad (5.3)$$

where P is the Cauchy principal value of the integral. The equation (5.1) can be transformed into a surface integral by using the δ-function relation

$$\int_a^b g(x)\delta[f(x)]dx = \sum_{x_o} g(x_o) \left|\frac{df}{dx}\right|^{-1}_{x=x_o} \qquad (5.4)$$

in which x_o represents a zero of the function f(x) contained in the interval (a,b). In three dimensions

$$\varepsilon_i(\omega) = \frac{4\pi^2 e^2}{m^2\omega^2} \sum_{v,c} \int_S \frac{2|\underline{e}.\underline{M}_{vc}|^2}{(2\pi)^3 |\nabla_k (E_c - E_v)|} ds \qquad (5.5)$$

where ds represents an element of surface in $\underline{k}$ space on the surface defined by the equation

$$E_c(k) - E_v(k) = E \qquad (5.6)$$

The matrix elements $|\underline{e}.\ \underline{M}_{cv}(\underline{k})|^2$ between a given couple of valence and conduction bands are shown to be smooth functions of $\underline{k}$, except near special $\underline{k}$ vectors where $|\underline{e}.\underline{M}_{vc}(\underline{k})|$ vanishes because of symmetry. Neglecting such a situation and taking $|\underline{e}.\underline{M}_{vc}(\underline{k})|$ as a constant, we find from equation (5.5) that the contribution to the dielectric function from a pair of bands is proportional to ω^{-2} and the quantity

$$J_{vc}(\omega) = \frac{2}{(2\pi)^3} \int_S \frac{ds}{|\nabla_k [E_c(\underline{k}) - E_v(\underline{k})]|} \quad ; \tag{5.7a}$$

or

$$J_{cv}(\omega) = \int_{BZ} \frac{2d\underline{k}}{(2\pi)^3} \delta[E_c(\underline{k}) - E_v(\underline{k}) - h\omega] \tag{5.7b}$$

which is called the joint density of states because it gives the density of pairs of states, one occupied and other empty, separated by an energy $h\omega$. This quantity mainly determines the interband contribution to ε_i and thus to the optical constants of solids. From equation (5.7) we see that singularities in the joint density of states are expected when

$$\nabla_k E_c(\underline{k}) = \nabla_k E_v(\underline{k}) = 0 \ , \tag{5.8}$$

or more generally when

$$\nabla_k E_c(\underline{k}) - \nabla_k E_v(\underline{k}) = 0 \ . \tag{5.9}$$

Critical points of type (5.8) occur in general at high symmetry points of the Brillouin zone, while critical points of the type (5.9) may occur at any $\underline{k}$ vector. The properties of critical points and their consequences for the phonon dispersion curves in crystals were first discussed by Van Hove (54) and Phillips (55) making use of topological considerations. Similar results hold for the electronic states in a periodic crystal where the energy difference function is a periodic function in the reciprocal lattice and must therefore possess such Van Hove singularities.

The analytic behaviour of $J_{vc}(\omega)$ near a critical point may be found by expanding $E_c(\underline{k}) - E_v(\underline{k})$ in a Taylor series about a singularity of energy difference $E_g(\underline{k}_g)$. In the expansion linear term is

identically zero at a critical point because of $\nabla_k[E_c(\underline{k})-E_v(\underline{k})] = 0$ anin parabolic approximation we retain only the quadratic term

$$E_c(\underline{k})-E_v(\underline{k}) = E_g(\underline{k}_g) + \sum_{i=1}^{3}\left(\frac{d^2(E_c-E_v)}{dk_i^2}\right)_{k=k_o}(k_i-k_{oi})^2 \qquad (5.10)$$

It can be written in the form

$$E_c(\underline{k})-E_v(\underline{k}) = E_g(\underline{k}_g) + \sum_{i=1}^{3} a_i(k_i-k_{oi})^2 \qquad (5.11)$$

The coefficients a_i in (5.11) represent the relative interband curvatures; in the effective mass notation

$$a_i = h^2[(1/m_i^c) - (1/m_i^v)] \qquad (5.12)$$

Denoting the wave vectors along the principal axes with the origin at the critical point by k_x, k_y, k_z.

$$E_c(\underline{k})-E_v(\underline{k}) = E_g + a_1k_x^2 + a_2k_y^2 + a_3k_z^2 \qquad (5.13)$$

We obtain four types of singularities, depending on the signs of a_1, a_2 and a_3. The critical points are called:

M_0 when all a_i (coefficients) are positive (minimum);

M_1 when two of a_i (coefficients) are positive and one negative (saddle point);

M_2 when two of a_i (coefficients) are negative and one positive (saddle point);

M_3 when all a_i (coefficients) are negative (maximum).

The analytical behaviour of the joint density of states near critical points can be obtained using (5.7b) and (5.13). The results are reported in table 5.1 and Fig. 5.1 for the three-dimensional case. A limiting two-dimensional case occurs when one of the coefficients a_i becomes vanishingly small. The results for the two-dimensional case are reported in table 5.2 and fig. 5.2. We notice that there are sharp discontinuities at the critical points (56).

TABLE 5.1 Joint density of states near critical points for the three-dimensional case. For convenience $A = 4\pi\,(a_1 a_2 a_3)^{-\frac{1}{2}}$ and B indicates a constant which depends on the detailed band structure. The expression $O(E-E_g)$ indicates a quantity that vanishes at least linearly when $E \to E_g$.

Type of c.p.	Notation	a_1 a_2 a_3	Joint density of states J_{vc}	
			$E < E_g$	$E > E_g$
Minimum	M_0	+ + +	$B+O(E-E_g)$	$B+A(E-E_g)^{\frac{1}{2}}+O(E-E_g)$
Saddle point	M_1	+ + −	$B-A(E_g-E)^{\frac{1}{2}}+O(E-E_g)$	$B+O(E-E_g)$
Saddle point	M_2	+ − −	$B+O(E-E_g)$	$B-A(E-E_g)^{\frac{1}{2}}+O(E-E_g)$
Maximum	M_3	− − −	$B+A(E_g-E)^{\frac{1}{2}}+O(E-E_g)$	$B+O(E-E_g)$

TABLE 5.2 Joint density of states near critical points for the two-dimensional case. For convenience $A = (4\pi/c)(a_1 a_2)^{-\frac{1}{2}}$, and B indicates a constant which depends on the detailed band structure.

Type of c.p.	Notation	a_1 a_2 a_3	Joint density of states J_{vc}	
			$E < E_g$	$E > E_g$
Minimum	M_0	+ + →0	$B+O(E-E_g)$	$B+A+O(E-E_g)$
Saddle point	M_1	+ − →0	$B-(A/\pi)\ln\lvert 1-(E/E_g)\rvert+O(E-E_g)$ when $E \neq E_g$	
Maximum	M_2	− − →0	$B+A+O(E-E_g)$	$B+O(E-E_g)$

The results for the singular part of the dielectric constant near any type of allowed three-dimensional critical point can be represented by the expression (7):

$$\varepsilon(\omega) \;\alpha\; (i)^{j+1}\,(\omega-\omega_g)^{\frac{1}{2}} \qquad (5.14)$$

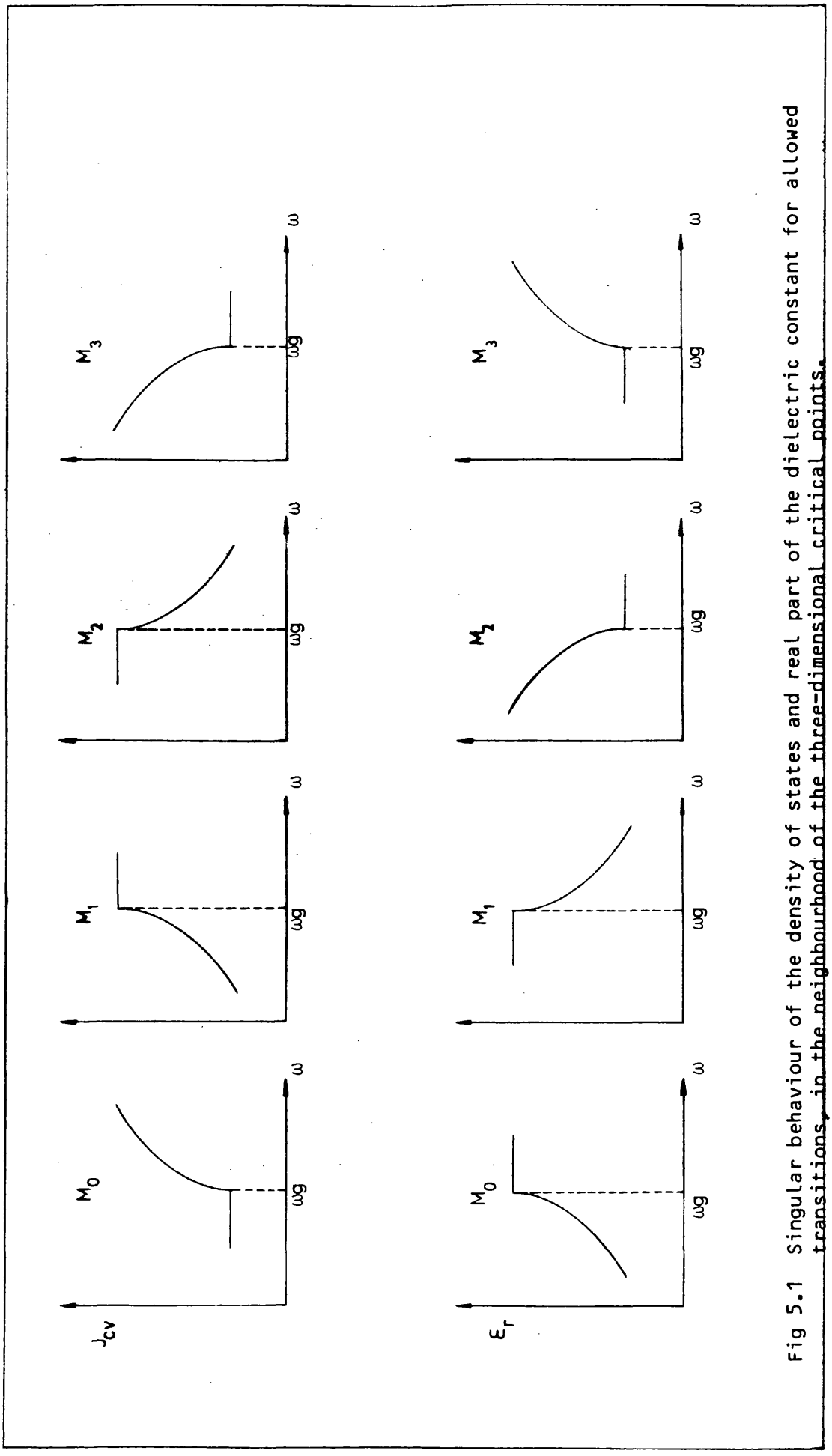

Fig 5.1 Singular behaviour of the density of states and real part of the dielectric constant for allowed transitions, in the neighbourhood of the three-dimensional critical points.

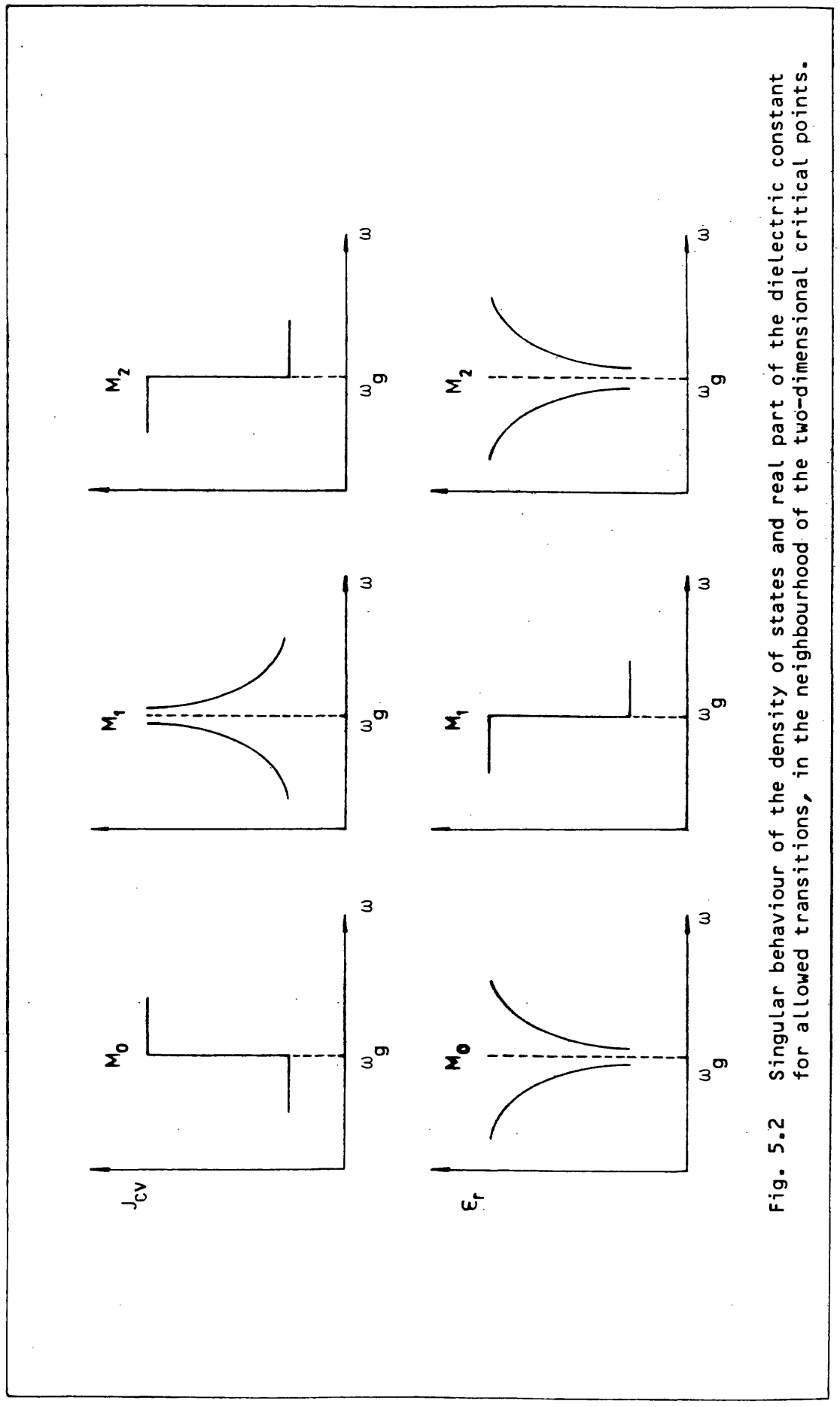

Fig. 5.2 Singular behaviour of the density of states and real part of the dielectric constant for allowed transitions, in the neighbourhood of the two-dimensional critical points.

where j is the subindex which designates the type of critical point. The shape of ε_r around a two-dimensional minimum can be obtained from the equation (5.3) and the table 5.2. The result is the following expression:

$$[\varepsilon_r(\omega) - 1] \propto -\frac{1}{\omega^2} \ln\left|1 - \frac{\omega^2}{\omega_g^2}\right| \qquad (5.15)$$

The shapes of $\varepsilon_r(\omega)$ near three- and two-dimensional critical points are sketched in figs. 5.1 and 5.2.

5.3 Properties of the optical constants (indirect and forbidden transitions)

We have considered only interaction between the electrons and the electromagnetic field resulting in vertical transitions on an E - k diagram. There can be other perturbations of the system in real crystals as impurities, dislocations etc. There is further, also in perfect crystals, the interaction with the phonons as quanta of the vibrational modes of the crystal lattice. The theory was first provided by Bardeen et al (58) and has been reviewed by Cardona (57), and others.

An indirect transition is produced by the interaction of a photon, an electron and a phonon. The imaginary part of the dielectric constant can be calculated by second order perturbation theory. Terms representing the electron-photon and electron-phonon interactions are included in the Hamiltonian. The electromagnetic interaction takes the electron from the initial state ($\underline{k}_i$) to a virtual intermediate state ($\underline{k}_v$) of the same crystal momentum ($\underline{k}_i = \underline{k}_v$), without conserving energy, while the phonon absorption or emission takes it from the intermediate state to the final state ($\underline{k}_f \neq \underline{k}_i$). Energy must be conserved in the total process.

The conservation laws for the complete transition are:

$$\underline{k}_i + \underline{k}_o = \underline{k}_f \pm \underline{k}_p; \quad E_i + h\omega = E_f \pm E_p \tag{5.16}$$

The plus sign refers to phonon emission and the minus to phonon absorption; $\underline{k}_o$ is the photon wave vector and can be neglected; $\underline{k}_p$ and E_p are the wave vector and energy of the phonon.

From second order perturbation theory are obtained close to threshold for parabolic bands the approximate expression (57)

$$\varepsilon_i \propto |M|^2 \frac{(\omega-\omega_g \pm \omega_p)^2}{\omega^2(\omega_f-\omega_i)^2}; \quad \text{for } \omega > \omega_g \pm \omega_p$$

$$\varepsilon_i = 0; \qquad \text{for } \omega < \omega_g \pm \omega_p \tag{5.17}$$

M is the matrix element of the electron-phonon interaction, which contains the temperature dependent phonon occupation numbers, $|M|^2$ is therefore proportional to the Bose-Einstein function $f_B(\omega_p/t)$ for phonon absorption and f+1 for phonon emission. The equation (5.17) describes a rather smooth variation of ε_i near ω_g. The curve consists of several pairs of components with the thresholds of the two components of a pair being equally spaced above and below E_g by the amount E_p. The temperature dependence of the two components is markedly different since the phonon absorption process freezes out at low temperatures. In principle these can be as many pairs of components as these are phonon branches in the crystal.

No maximum in reflectance is observable for certain other types of absorption threshold. It has so far been assumed that $|M_{vc}|$ is constant and non zero in the vicinity of an allowed transition in the electric dipole approximation. But if $|M_{vc}| = 0$ at $\underline{k}_o$ the transition is said to be forbidden. In such cases an expansion of $|M_{vc}|$ near $\underline{k}_o$ gives terms in $|\underline{k} - \underline{k}_o|$ that will make $|M_{vc}|^2$

proportional to $(E-E_g)$ and $\varepsilon_i \propto (E-E_g)^{3/2}$. In such cases a maximum in n and R is not detectable. The same is true for indirect transitions. The energy dependence of ε_i for indirect forbidden transitions is $\varepsilon_i \propto (E-E_g)^3$. (52)

The absolute values of ε_i however, are some orders of magnitude lower than for direct transitions. Hence indirect transitions can only be observed in absorption at energies where no direct transitions occur and cannot be detected in reflectance. When characteristic line shapes are available from optical measurements, they are useful to identify the nature of the interband transition experimentally observed and therefore to determine its location in the B.Z. when the band structure is known.

5.4 Experimental techniques

Direct measurements of the dielectric constant in the optical spectrum are possible using ellipsometric techniques, but such measurements are tedious and beset with problems of sample surface preparation. It is generally more convenient to measure absorption and reflection coefficients. Absorption measurements may be used only in spectral ranges where the sample is not highly absorbing. This limits such measurements to photon energies below and slightly above the fundamental energy gap. Reflectivity measurements have no such limitations and are useful over a wide spectral range. The absorption coefficient α is related to the dielectric constant

$$\alpha(\omega) = \frac{\omega \varepsilon_i(\omega)}{nc} \qquad (5.16)$$

where c is the free space velocity of light and n (the ordinary refraction index) is the real part of the complex index of refraction $N = n + ik$ where k is known as the extinction coefficient. The index

of refraction and the dielectric constant are related by:

$$\varepsilon_r = n^2 - k^2 \qquad (5.17)$$

$$\varepsilon_i = 2nk \qquad (5.18)$$

So in order to determine $\varepsilon_i(\omega)$ from experiments, optical absorption measurements would be the most appropriate. However, in those frequency ranges where there is strong absorption, it becomes inpractical to measure $\alpha(\omega)$.

In semiconductor, as with other material, strong absorption is due to lattice, plasma and electron interband transitions. Above the fundamental gap, other parameters, such as reflectance (R) carry all the information about ε_i and contain more detailed structure not available in absorption measurements.

The normal incidence reflectivity R is related to n and k by Fresnel's equations:

$$R = \frac{(1-n)^2 + k^2}{(1+n)^2 + k^2} \qquad (5.19)$$

or

$$R = \frac{(\varepsilon_r^2+\varepsilon_i^2)^{\frac{1}{2}} - [2\varepsilon_r + 2(\varepsilon_r^2+\varepsilon_i^2)^{\frac{1}{2}}]^{\frac{1}{2}} + 1}{(\varepsilon_r^2+\varepsilon_i^2)^{\frac{1}{2}} + [2\varepsilon_r + 2(\varepsilon_r^2+\varepsilon_i^2)^{\frac{1}{2}}]^{\frac{1}{2}} + 1} \qquad (5.20)$$

From equation (5.20) it can be seen that it is not possible to separate ε_r and ε_i from a single reflectance measurement at normal incidence reflectivity.

Since reflectivity measurements involve a wide spectral range, it is not possible, in the region above the fundamental energy gap, to make any simplifying assumptions about equation (5.19 or 5.20). It is possible, however, to rewrite the Kramers-Kronig relations in a form that provides sufficient information to determine n and k. If we consider the complex reflection coefficient r:

$$r = \rho e^{i\theta} \tag{5.21}$$

where $\rho = R^{\frac{1}{2}}$ and θ is the angular phase shift suffered by the incident light upon reflection, related to R by the dispersion relation given by Toll (59)

$$\theta(\omega) = \frac{2\omega}{\pi} P\int_0^\infty \frac{\ln\rho(\omega') - \ln\rho(\omega)}{\omega'^2 - \omega^2} d\omega' \tag{5.22}$$

$$n = \frac{1 - \rho^2}{\rho^2 - 2\rho \cos\theta + 1} \tag{5.23}$$

$$k = \frac{-2\rho \sin\theta}{\rho^2 - 2\rho \cos\theta + 1} \tag{5.24}$$

$$\varepsilon_i = -\frac{4\rho(1-\rho^2)\sin\theta}{(\rho^2 - 2\rho\cos\theta + 1)^2} \tag{5.25}$$

The integral of equation (5.22) is nonsingular for $\omega \to \omega'$, since the experimental $R(\omega)$ never exhibits an infinite slope. This integral is evaluated numerically with a standard polynomial integration formula. The low-frequency limit of experimental data coincides normally with the region in which the optical constants (and hence ρ) become frequency-independent. It is assumed that no frequency variation of ρ occurs below this limit. For low frequency we have:

$$\varepsilon_r = \text{constant}, \quad \varepsilon_i = 0, \quad R(\omega) = \text{constant} \tag{5.26}$$

At high frequencies, ρ becomes small and can be approximated by the asymptotic behaviour of ε (62) for $\omega \to \infty$

$$\varepsilon(\omega) \sim 1 - \frac{2c}{\omega^2} \tag{5.27}$$

and

$$\rho(\omega) \approx \frac{c}{\omega^2} \tag{5.28}$$

where C is a constant which reconciles $\rho(\omega)$ of equation (5.28) with the experimental value of ρ at high-frequency cutoff ω_c.

For the case of large-band-gap materials where typical cutoff frequencies ω_c correspond to about 25ev photon energy, equation (5.28) can be modified by:

$$\rho(\omega) \sim \frac{c}{\omega^m} \qquad (5.29)$$

The exponent m can be adjusted to fit directly measured values of ε_i (or the absorption coefficient) near the fundamental absorption edge. In insulators and semiconductors m can be chosen so that the absorption coefficient is zero at frequencies below the fundamental absorption edge.

A discussion of the computational methods used are given by Roessler (61) and Cardona (62).

5.5 Experimental conditions for the measurement of optical constants.

The purpose of optical measurements is therefore to obtain transition energies which can be related to the band structure.

When monochromatic light strikes an optically smooth surface, the light is reflected. The ratio of the intensity reflected (I_R) to that incident (I_o) is known as reflectance (R). When some of the incident intensity is transmitted through the sample (I_T), then transmittance (T) is defined as (I_T/I_o).

The surfaces of the sample must not scatter light out of the optical path either upon reflection or transmission. Therefore all the light reflected or transmitted must reach the detector. In addition, when it is known that the atmosphere, and the optical components will absorb some of the radiation, the optical path of the light must be kept the same for both the measurement of the incident intensity I_o and the reflected (I_R) or transmitted (I_T)

intensity. The efficiency of the detectors and source must be independent of time. It is clear that all of these conditions are hard to meet simultaneously and with proper precision over the whole photon energy range.

Modulated reflectance eliminates some of these problems when $\Delta R/R$ or $R'(\omega)/R(\omega)$ is measured as a function of energy. Any intensity losses reduce both ΔR (or R') and R by the same factor.

The experimental configuration is drawn up to satisfy the simple Fresnel conditions and therefore the angle of incidence in this kind of optical work is kept near normal ($\sim 7^{o}$). If the sample thickness is much greater than α^{-1}, the reflectivity at normal incidence (R) is given by the equation (5.19).

For experimental condition such that interference effects due to internal reflections are negligible, the transmission is given by

$$T = \frac{I_T}{I_o} = \frac{(1-R)^2 e^{-\alpha d}}{1+R^2 e^{-2\alpha d}} \qquad (5.30)$$

where α is the absorption coefficient and d is the sample thickness. Equation (5.30) enables us to calculate α from the experimental values of T and R.

$$\alpha = \frac{1}{d} \ln \left\{ \frac{(1-R)^2}{2T} + \left[R^2 + \left(\frac{(1-R)^2}{2T} \right)^2 \right]^{\frac{1}{2}} \right\} \qquad (5.31)$$

Generally, the reflectivity varies slowly with photon energy, and the spectral variation of the transmission is principally due to the variation of the absorption coefficient. The absorption coefficient characterizes the medium through which the wave is travelling. The structure in the reflectivity is usually similar to that of the structure in ε_r and ε_i of the type associated with a Van Hove critical point. It is therefore, sometimes possible to identify

critical points in the reflection spectrum without doing the Kramers-Kronig analysis.

5.6 Optical absorption of the I-III-IV-□-VI_4 compounds near the fundamental edge. Analysis and results.

A standard grating monochromator was used to give radiation in the wavelength range 1.85 to 0.45μm which covered the required range for the various band gap energies of this family of quaternary materials. The light source was a tungsten filament lamp powered by a stabilized supply and the light was chopped at the input to the monochromator. The output from the monochromator was focussed on the surface of the crystal and behind the sample was the photomultiplier. The outputfrom the photomultiplier was applied to a pre-amplifier and lock-in amplifier system, and the output of this to a chart recorder. Thus a spectrum of the transmitted light as a function of wavelength was obtained at room temperature for each material and also the variation of the incident light intensity as a function of wavelength. The ratio gives the transmittance (T) of the radiation through the sample. The absorption coefficient is given by equation (5.31). In this equation R the reflectance can be taken as a constant over the range of wavelengths concerned. For thin specimens used in the measurements of very high absorption coefficient the denominator in the equation (5.30) is effectively unity.

Transmission data were processed by digital computer methods to obtain absorption coefficients as a function of photon energy ($h\nu$). The absorption functions were analysed to identify interband-transition mechanisms. The general formulation for this analysis has been developed in the sections (5.2) and (5.3).

For direct band transitions, the absorption coefficient should vary with photon energy as $(A/h\nu)(h\nu-Eg)^n$, where n is $\frac{1}{2}$ for allowed and 3/2 for forbidden transitions and A is a constant. For indirect band transitions, the absorption coefficient should vary with photon energy as $(B/h\nu)(h\nu-E_g \pm E_p)^m$, where m is 2 for allowed and 3 for forbidden transmitions and B is a constant. A review of this analysis is given by Johnson (63). The computer program for the absorption coefficient included the numerical calculation of $(\alpha h\nu)^i$ for $i = 2, \frac{2}{3}, \frac{1}{2}, \frac{1}{3}$. We plot these values versus $h\nu$.

This analysis of the absorption coefficients for these quaternary materials shows the rise of α follows the relation

$$\alpha = (A/h\nu)(h\nu-E_g)^{\frac{1}{2}} \qquad (5.32)$$

The direct gap was found from the plot of the straight line $(\alpha h\nu)^2$ vs $h\nu$ and the intercept gives us $E_g = (h\nu)_{int}$. A typical curve of this analysis for $CuGaSn\square Se_4$ is shown in Figure 5.3. The values of the energy gaps of the materials are shown in table 5.3. The values for related ternary I-III-VI_2 compounds are included for comparison. As indicated in the chapter 2, the quaternary defect compounds have the same chalcopyrite structure as the related ternaries. It is therefore of interest to look at changes in energy gaps from ternary to quaternary.

It can be seen that for each ternary there is a systematic variation of both energy gaps of the quaternaries related with the same ternary. With the inclusion of the larger atom of Sn (compare with Ge) there is an observed decrease in the energy gap. The inclusion of the atom Ge increases the energy gap compared with the related ternary. Another change of interest is the higher value of the energy gap for silver than for copper compounds.

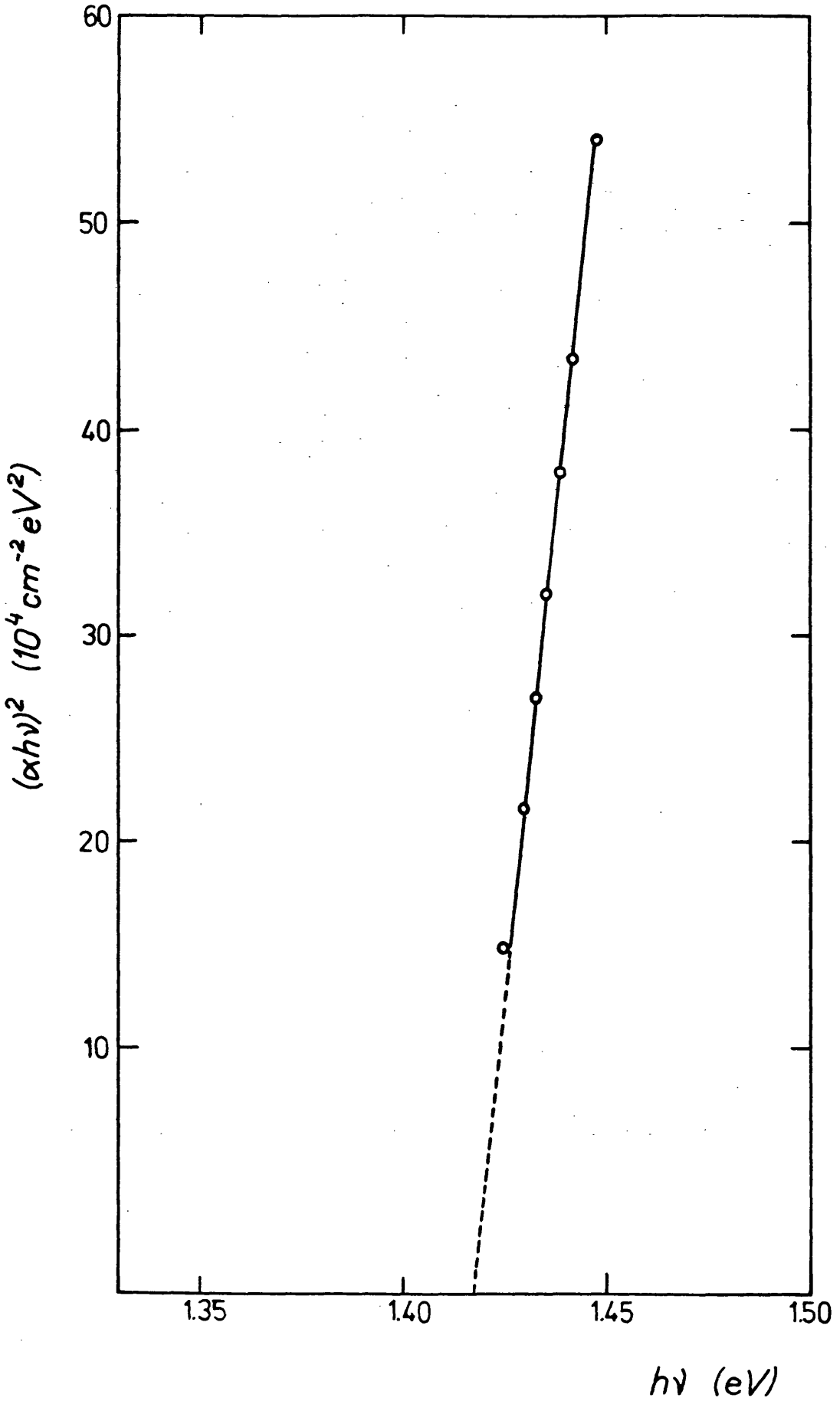

Figure 5.3 Absorption data indicating direct transition in $CuGaSn\square Se_4$ at room temperature

TABLE 5.3

Comparison of physical properties of some ternary and quaternary defect adamantine compounds

SELENIDE COMPOUNDS							
Ternary	a(nm)	c/a	E_g (eV)	Quaternary	a(nm)	c/a	E_g (eV)
$CuGaSe_2$	0.5616	1.962	1.68	$CuGaGe\square Se_4$	0.5568	1.947	1.854
				$CuGaSn\square Se_4$	0.5611	1.958	1.420
$AgGaSe_2$	0.5992	1.817	1.73	$AgGaGe\square Se_4$	0.5826	1.782	1.845
				$AgGaSn\square Se_4$	0.5869	1.843	1.690
$CuInSe_2$	0.5782	2.000	1.04	$CuInGe\square Se_4$	0.5640	1.980	1.232
				$CuInSn\square Se_4$	0.5700	2.000	0.710
$AgInSe_2$	0.6102	1.910	1.24	$AgInGe\square Se_4$	0.5759	1.877	1.575
				$AgInSn\square Se_4$	0.5877	1.920	0.940
$CuAlSe_2$	0.5617	1.940	1.94	$CuAlGe\square Se_4$	0.5575	1.916	2.360
				$CuAlSn\square Se_4$	0.5604	1.954	1.900
$AgAlSe_2$	0.5968	1.800	2.65	$AgAlGe\square Se_4$	0.5871	1.755	
				$AgAlSn\square Se_4$	0.5882	1.821	
SULPHIDE COMPOUNDS							
$CuGaS_2$	0.5349	1.959	2.43	$CuGaGe\square S_4$	0.5302	1.926	
				$CuGaSn\square S_4$	0.5358	1.956	1.910
$AgGaS_2$	0.5757	1.790	2.73	$AgGaGeS_4$	Orthorhombic a = 0.8310 b = 0.5775 c = 0.5950		1.860
				$AgGaSn\square S_4$	0.5757	1.844	1.765

TABLE 5.4

Energy gap of some quaternary normal adamantine compounds

Compound	Energy gap (eV)
Cu_2ZnSiS_4	3.25
$Cu_2ZnSiSe_4$	2.33
Cu_2ZnGeS_4	2.10
$Cu_2ZnGeSe_4$	1.29

This is probably connected with a lower electronegativity value for silver than for copper. The unexpectedly low value of the energy gap for $AgGaGe\square Se_4$ may be connected with the high lattice distortion of this compound (c/a = 1.782) producing changes in the band structure of this compound. Comparing only the defect quaternary compounds in this table, it can be seen that as the group IV atom changes from germanium to the larger tin atom there is an observed decrease in the optical band edge. This was observed also by D.M.Schleich and A.Wold (64) in the normal quaternary compounds reported in the table 5.4. In this table it can be seen that where silicon atoms are changed to the larger germanium atoms, there is a decrease in the band gap. A similar change in the band edge is also observed when the larger selenium atom is substituted for sulphur.

5.7 Electronic structure of the quaternary defect adamantine compounds of the type I-III-IV-□-VI_4

The search for new semiconducting materials for application in light emitting diodes, lasers, solar cells, light detectors and nonlinear optical elements has resulted in a great deal of activity in the investigation of the energy band structures of ternary compounds during the last decade and we report here the first analysis of the band structure of some quaternary defect adamantine compounds based on the experimental results.

Since the crystal structures of the defect quaternaries under consideration (excepting $AgGaGeS_4$) are very closely related to the ternary compounds, and the I-III-VI_2 chalcopyrite compounds are closest structural and electronic analogue II-VI compounds, we would expect that much useful information can be gained from the perturbation treatment based on the well established properties

of the simple zincblende materials. Special consideration must, of course, be given to the vacancy in these compounds which cannot be treated as a perturbation (66).

The electronic band structures of I-III-VI_2 and II-IV-V_2 chalcopyrite semiconductors have been reviewed by Gorynova et al (67), Shay and Tell (68), Shileika (69), Chaldyshev (70), Shay and Wernick (71), Shileika (72) and Miller et al (66). In this work some recent results will be considered and the problems for further studies of the energy band structure of these quaternary compounds will be discussed.

In the partially ordered defect chalcopyrite structure of these quaternary compounds there are five interesting aspects of this structure

(a) Compression of the crystal lattice along z-axis ($c < 2a$).

(b) Anion shift from the tetrahedral positions.

(c) Doubling of the unit cell in the z-direction resulting from the position of the three cations and the vacancy. Since the volume of the unit cell of chalc. lattice is 4 times that of zincblende the Brillouin zone (B.Z.) is 4 times smaller. A comparison of the B.Z. is shown in fig. 5.4.

(d) There are vacancies into the structure.

(e) There are statistical population of cations and vacancy (see chapter IV).

Calculations of the band structure of these compounds is not so simple, and requires inclusion of all three first points (non cubic potentials) and the last two points listed above.

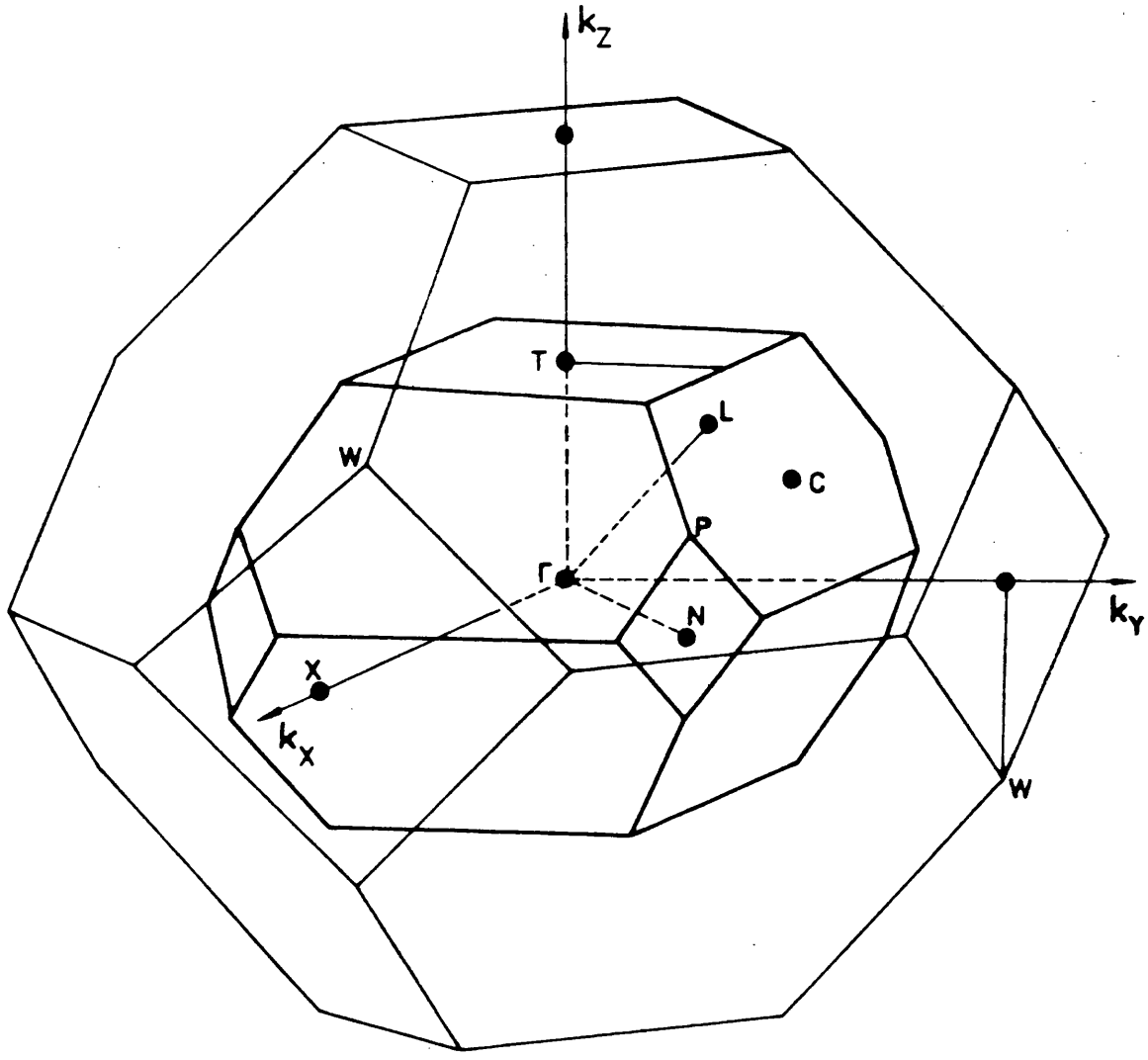

Fig. 5.4 Comparison of the Brillouin zones of the zincblende and chalcopyrite lattices.

The most obvious effect of the vacancies occurs in lattice dynamics. The force constants associated with the missing atom go to zero. In this case the vibration mode drops significantly in frequency. This is called the breathing mode which turns out to have several interesting properties. In this mode the four neighbours of the vacancy move together along the anion-vacancy band direction (see fig. 5.5). Grouped theoretically such a mode may be treated as having spherical symmetry, like an s-orbital on the vacant site.

Miller (66) reported that the irreducible representations (IR's) of the breathing modes may be found by performing all symmetry operations on such spherical basis functions and forming the scalar products of thin characters with the rows of the character table for the appropriate point group. The IR's of the lost modes may be found in a similar way using x, y and z displacement basis functions or p-orbitals. Thus one vacancy per unit cell has the symmetry of $x^2 + y^2 + z^2$ (A_1) and the missing modes have that of x, y, z ($B_2 + E$).

The positive potential energy at the vacant site ensures that in the highest valence states the electrons are concentrated near the vacancies. Such bands are very flat because they are made up of weakly interacting orbitals associated with the vacancies and their energies are extremely sensitive to the breathing modes.

The absence of an ion on the vacant site makes the Coulomb field seen by the anions not only significant but also extremely asymmetric, especially as seen by the breathing mode. We should therefore expect to observe nonlinear effects.

The energy gaps observed in I-III-IV-□-VI_4 and I-III-VI_2 compounds are listed in table 5.3. These materials all have direct

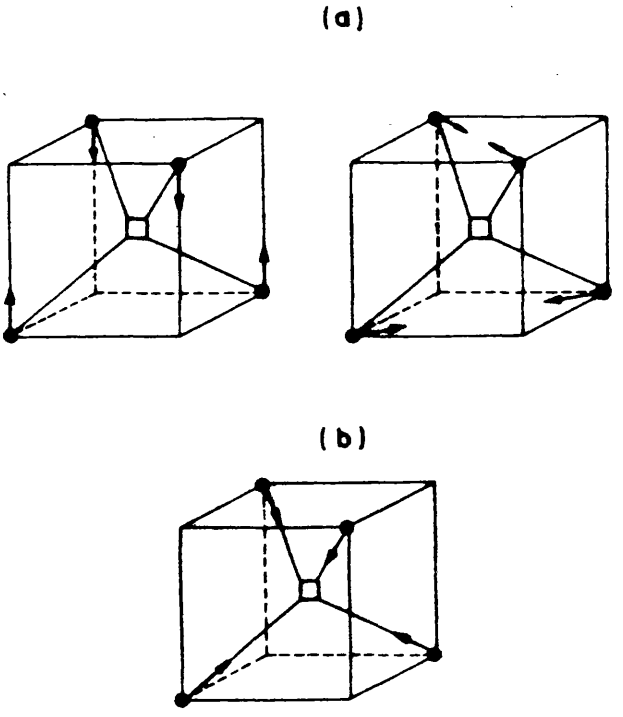

Fig. 5.5 (a) Two A_1 modes with displacements as shown in the neighbourhood of a vacancy. The correct A_1 modes are linear combinations of these.

(b) As the central constant is reduced, the lower lying A_1 modes takes the form shown (breathing mode). See ref. 13.

band gaps and we studied in $CuGaSn\square Se_4$ the three transitions E_A, E_B and E_C that characterise the chalcopyrite materials because of the crystal field and spin-orbit splitting of the Γ_{15} valence bands of zincblende. The quasi-cubic model is again fairly successful in describing the crystal field splitting in terms of the tetragonal compression.

Fig. 5.6 illustrates the band structure of I-III-VI_2 chalcopyrite compounds, and we propose the same band structure for the I-III-IV-$\square$-VI_4 chalcopyrite compounds because this model explains our experimental results very well, and also because these two groups of the adamantine family have the same crystal structure. This figure shows how the lowest direct energy gap of chalcopyrite is related to that of zincblende. The combined action of spin-orbit coupling and tetragonal field completely removes the triple orbital degeneracy of the zincblende Γ_{15} valence band. The five-fold degenerate d-levels split into a three-fold Γ_{15} and a two-fold Γ_{12} in a tetrahedral field. The spin-orbit contribution splits the p-like Γ_{15} into Γ_8 and Γ_7 levels while the d-like Γ_{15} gives Γ_7 and Γ_8 in reverse order. The Γ_8 band derived from the d-like Γ_{15} band will force the p-like Γ_8 upwards reducing the band gap energy. Likewise, the close proximity of the two Γ_7 bands will reduce the spin orbit splitting of the p-levels in chalcopyrite. A mixing of the wave functions for these states will accompany the change in position of the bands and an estimate of the amount of hybridization can be obtained either from the downshift of the energy gap relative to the cubic binary analogue or from the observed spin-orbit splittings of p-like binary analogue and atomic d-levels.

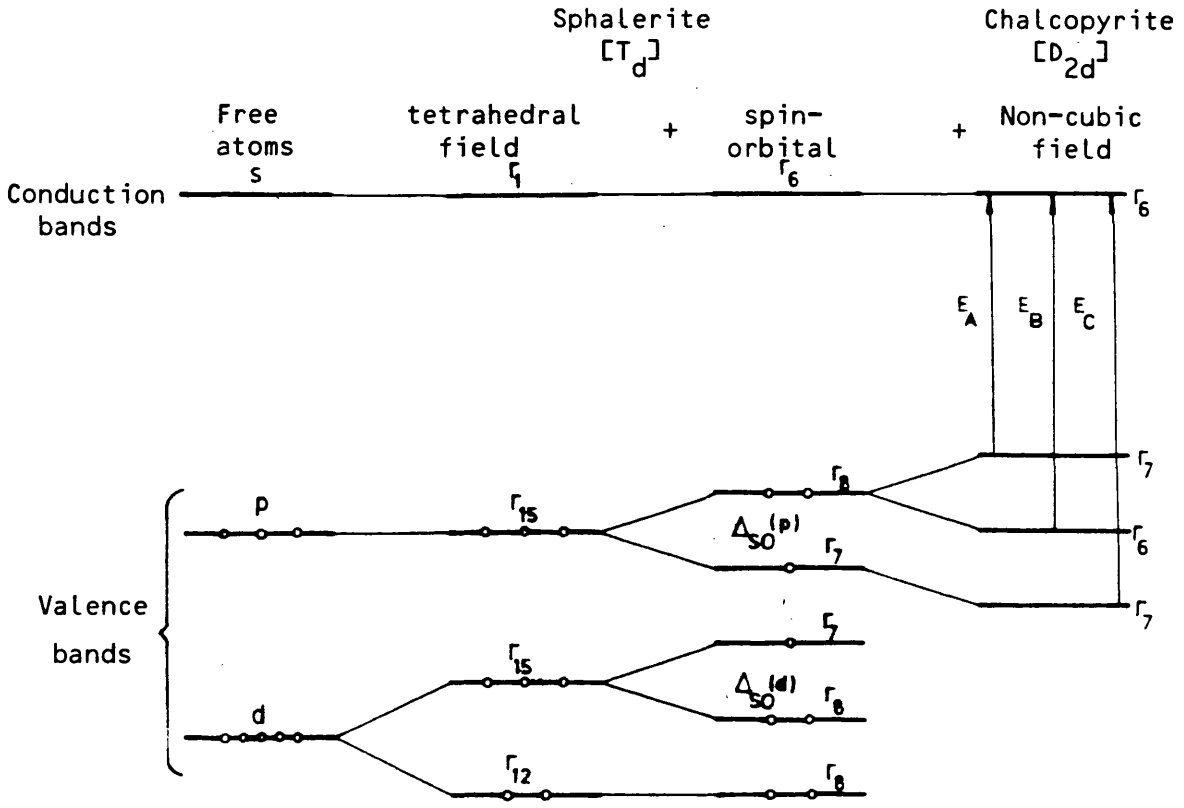

Fig. 5.6 Sketch of the band structure of chalcopyrite compounds at the centre of Brillouin zones (Shay and Tell ref. 68).

5.8 Reflectance measurements on $CuGaSn\square Se_4$

The object of this experiment is to measure the values of reflectance as a function of wavelength or photon energy over an extended range for a semiconductor whose reflecting surface has been prepared with care. In our case the surface of the crystal was very good and no further polishing was necessary for the reflectance work. A back reflection Laue photograph showed that the plane of the reflectance surface of the sample was the (112) and the principal c-axis was inclined at 35.7^{o} to this plane.

It is possible to obtain a reflectance spectrum by two methods. I_o and I_R may be measured separately over the wavelength spectrum and then R may be calculated, or I_o and I_R are found for each wavelength, thus R, over the spectrum.

Optical measurements were performed with a system designed for measurements of specular reflectance and absorption on samples with small surface areas. The basic system employs a standard grating monochromator to give radiation in the wavelength range 0.5 to 0.85μm which covers the required range for the various energy levels in the vicinity of E_g. The light source was a tungsten filament lamp powered by stabilised supply and the light was chopped at the input to the monochromator. The output from the photomultiplier was applied to a preamplifier and lock-in amplifier system and the output of this applied to a chart recorder. Thus a spectrum of reflected signal as a function of wavelength was obtained at each temperature and also for a standard aluminised glass. The ratio of sample to standard reflectance reading was taken as the reflectance value R.

A polarizer could be placed in the beam between monochromator & sample so that the reflectance spectrum could be determined for different polarizations. Thus the spectrum with polarization perpendicular

to the c-axis was obtained, but it was not possible with normal reflection to have the polarization parallel to the c-axis owing to the orientation of the sample face. However spectra were taken with the polarization having a maximum component parallel to c.

The use of the two polarization orientations was necessary since the wavelength of the peaks corresponding to transitions (E_A and E_B) are obscured. From the second and third valence bands could be determined satisfactory. From the curve (fig. 5.7) without polarization, it was not possible to obtain E_A, the transition from the highest valence band, with reasonable accuracy as is shown by the curve. Figs. 5.8, 5.9 and 5.10 show the reflectance for room temperature 295K, 200K and 4K respectively with the two polarization arrangements. To determine the wavelength of E_A, graphs of $\Delta R = R_{\parallel} - R_{\perp}$ were plotted as a function of λ and the curves for 295K, 200K and 4K are shown in fig. 5.11.

The variations of E_A, E_B and E_C with temperature are shown in table 5.5.

TABLE 5.5 Variation of the transitions to a single conduction band from three valence bands for different temperatures.

Temp.(K)	E_A(eV)	E_B(eV)	E_C(eV)
4	1.514	1.578	1.803
50	1.513	1.578	1.803
100	1.510	1.573	1.799
150	1.506	1.566	1.790
200	1.498	1.552	1.776
250	1.486	1.538	1.753
295	1.471	1.524	1.736

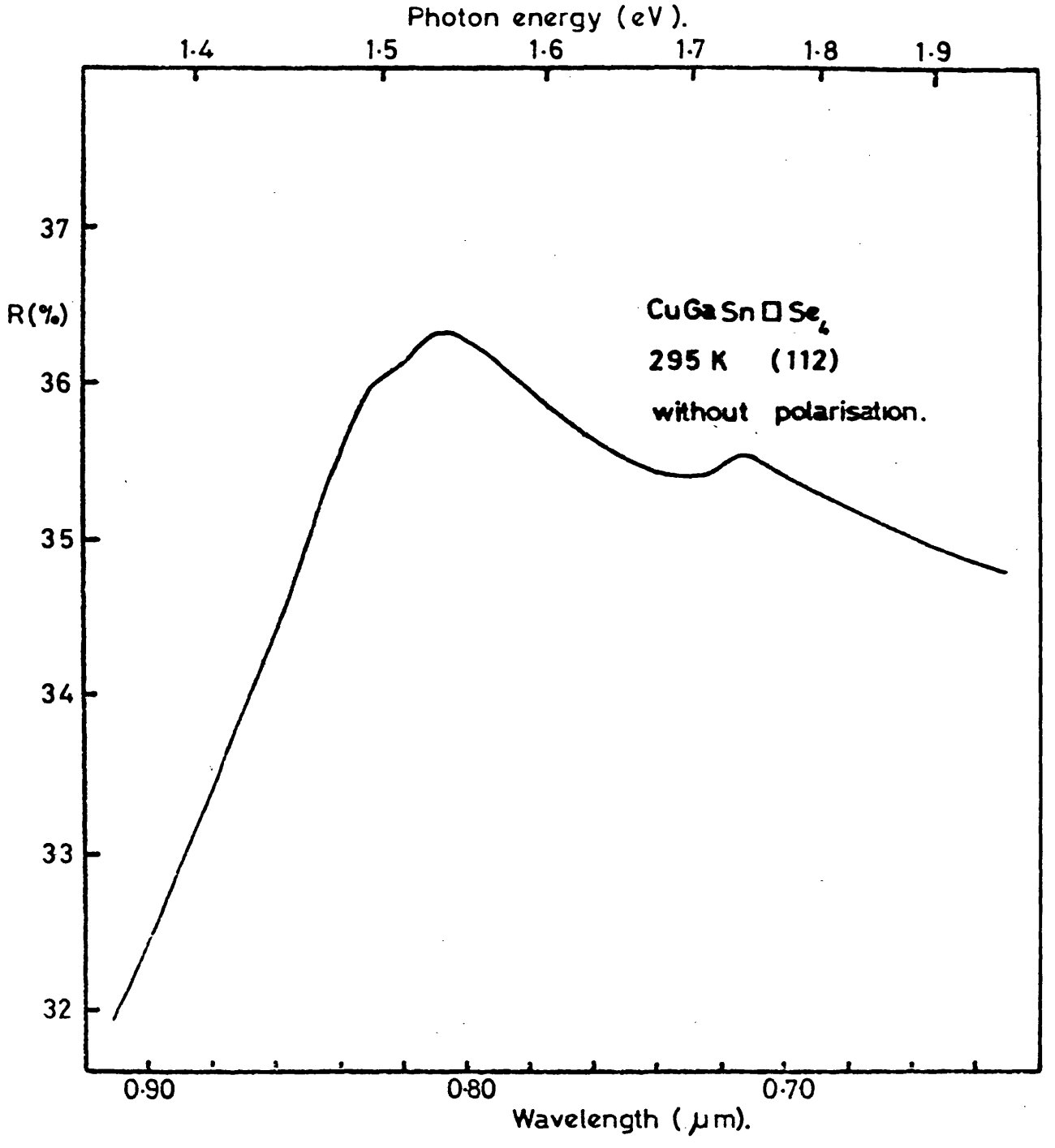

Fig. 5.7 Reflectivity spectrum of $CuGaSn\square Se_4$ at room temperature.

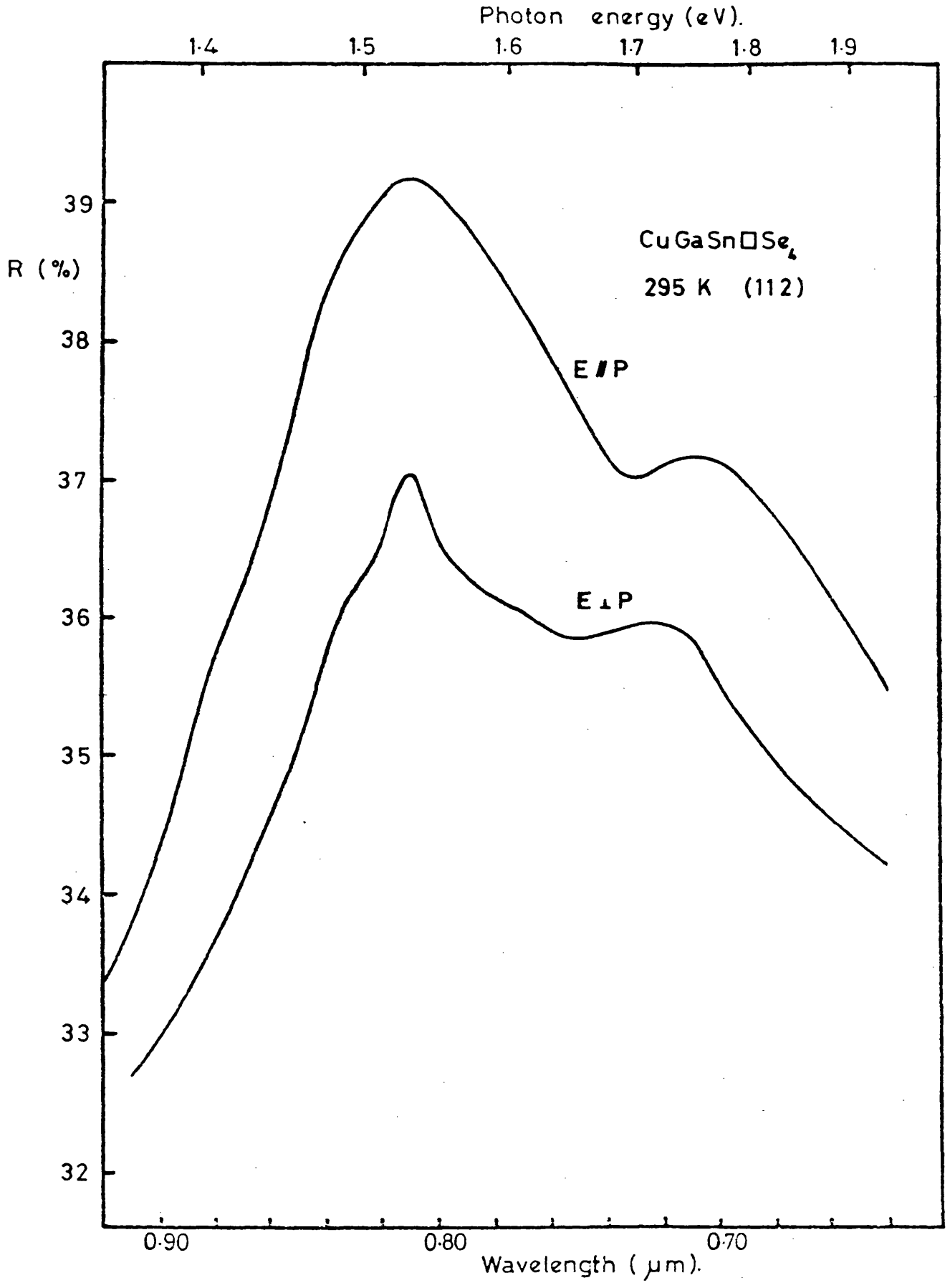

Fig. 5.8 Reflectivity spectrum of $CuGaSn\square Se_4$ at room temperature (295K)

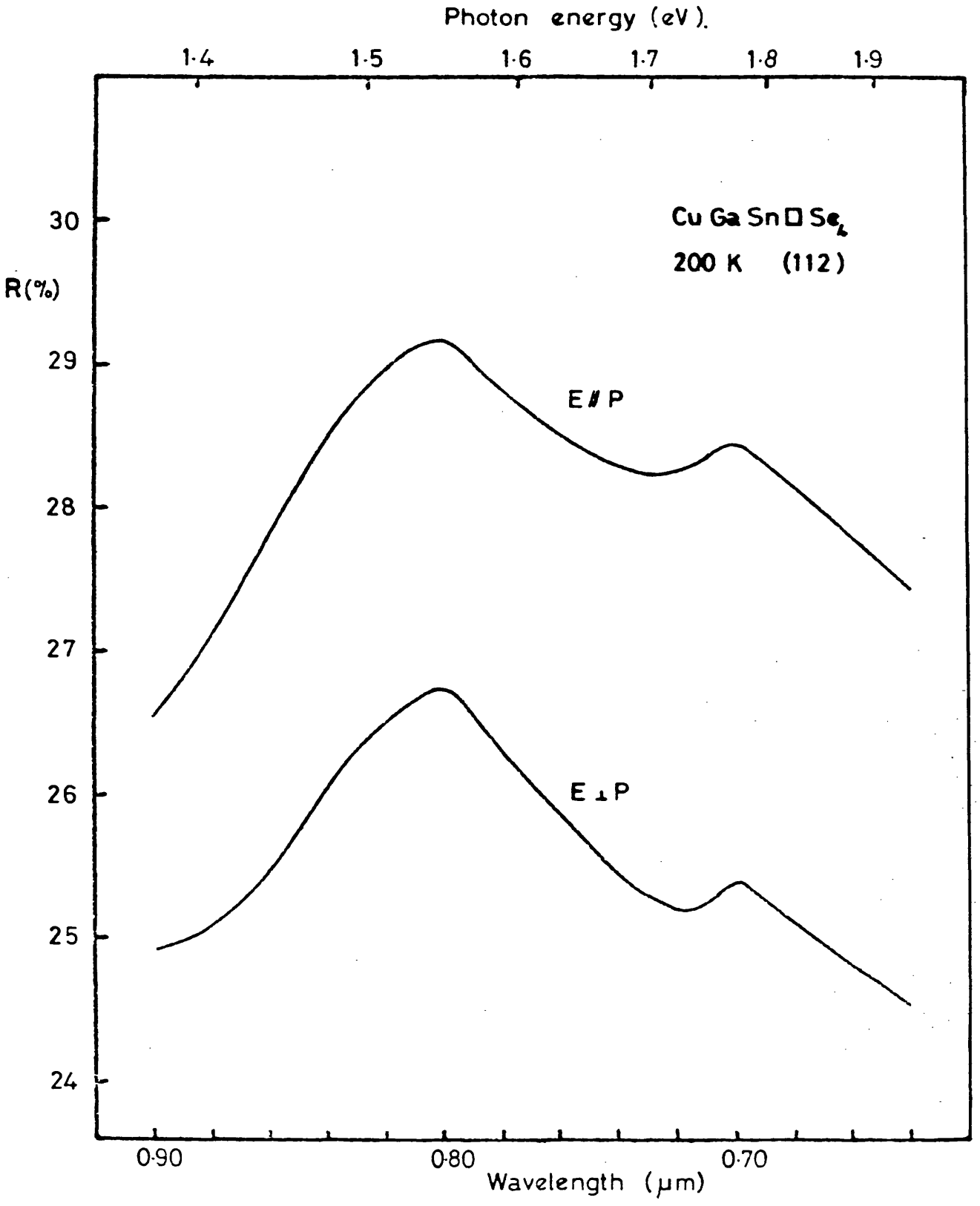

Fig. 5.9 Reflectivity spectrum of $CuGaSn\square Se_4$ at temperature 200K

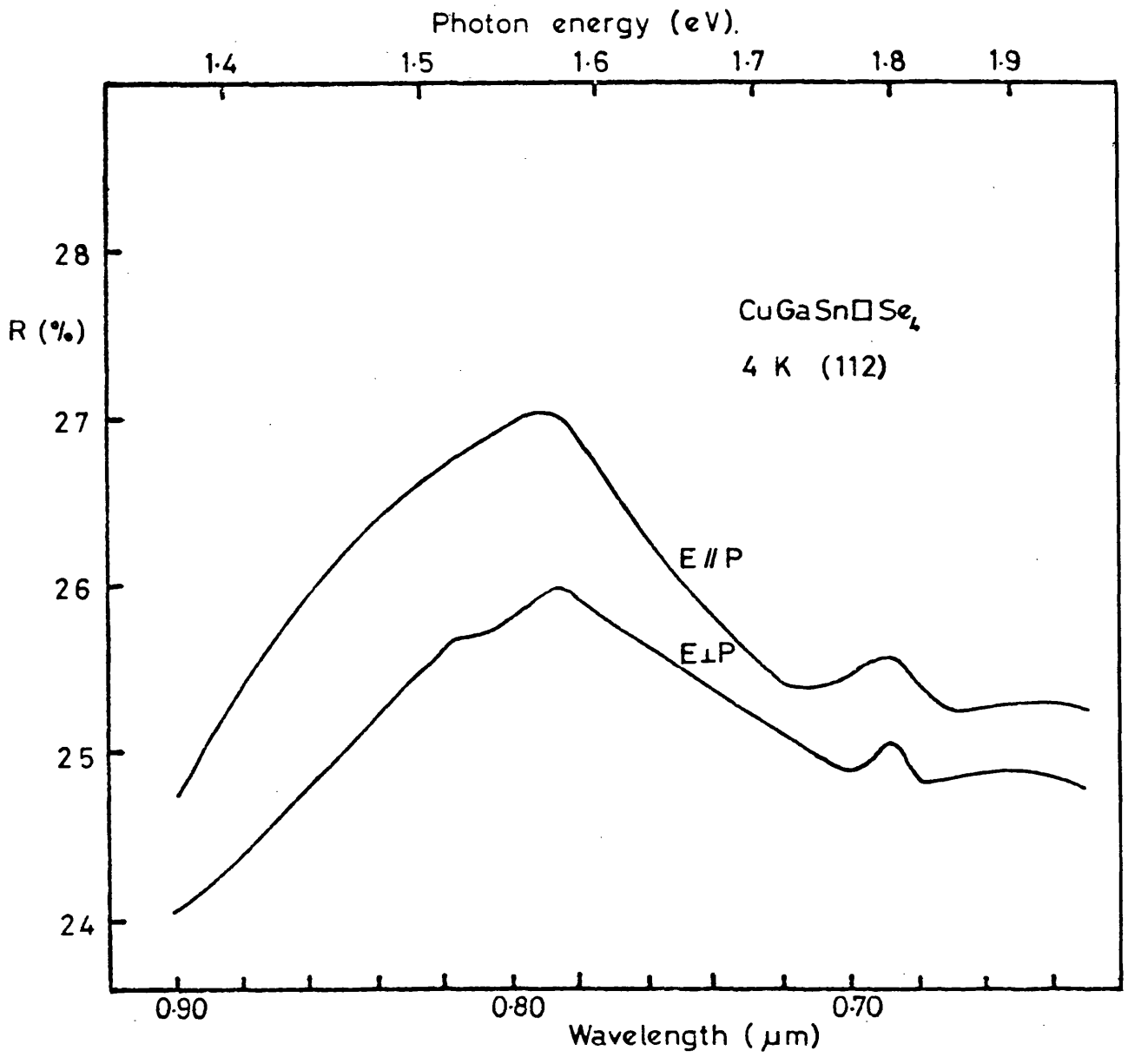

Fig. 5.10 Reflectivity spectrum of $CuGaSn\square Se_4$ at temperature 4K.

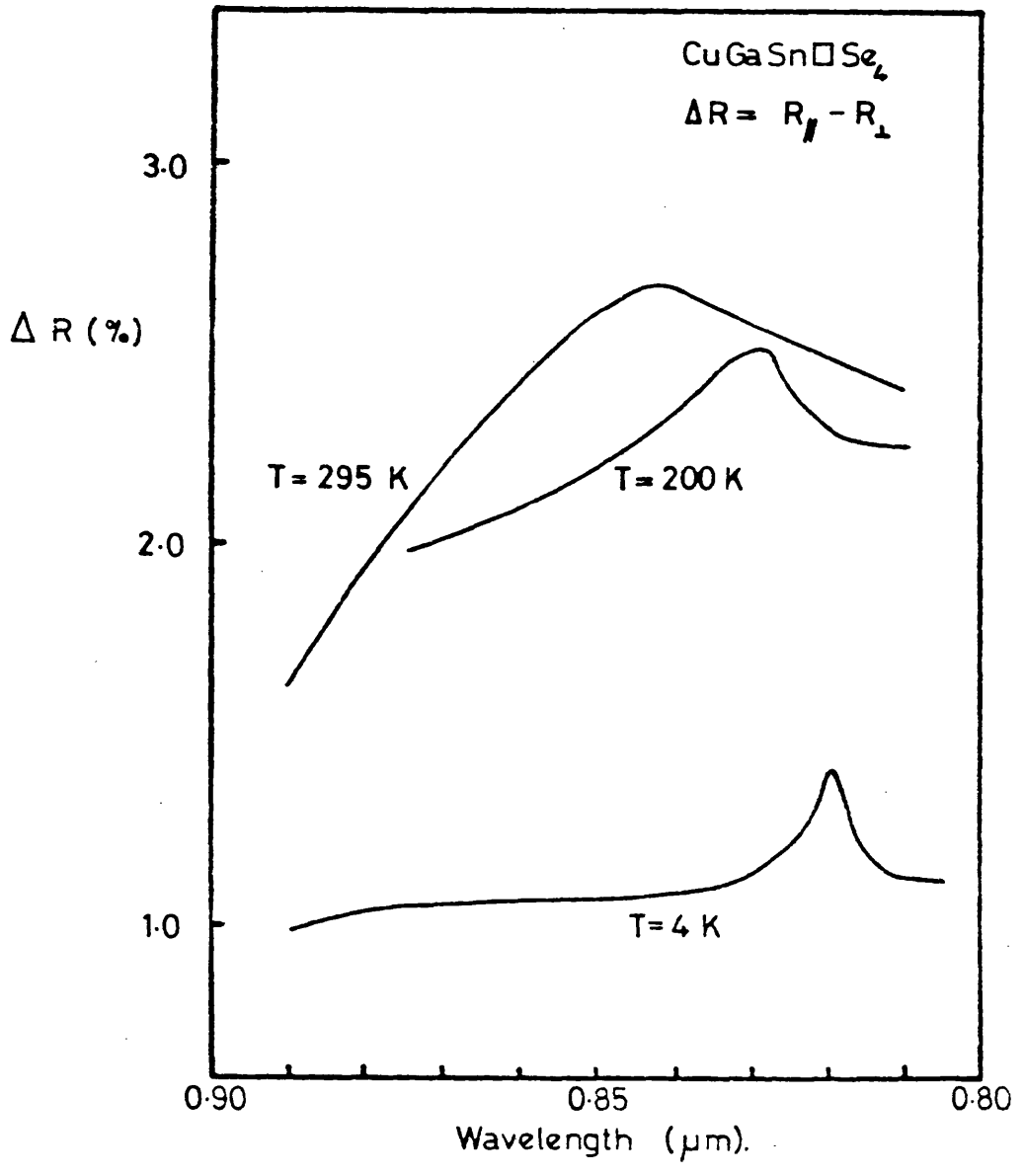

Fig. 5.11 Graphs of $\Delta R = R_{\parallel} - R_{\perp}$ versus λ for three different temperatures, 295K, 200K and 4K

5.9 Temperature dependence of bands structure, analysis and results

As was found in the case of the chalcopyrite alloys of $CuGa(Se_{1-x}S_x)_2$, the Varshni equation (73) could not be made to give a good fit to this experimental data. Hence here again the equation of Manoogian and Leclerc (74) was used in the form

$$\Delta E = E_o - E = UT^{2/3} + V\theta[\coth(\theta/2T) - 1] \qquad (5.33)$$

where U, V and θ are parameters independent of temperature. The first term in equation (5.33) represents the effect of lattice dilation. It is the function of T raised to the power (2/3). The second term represents the contribution due to vibration frequency (θ) of the phonon, where $\theta = h\nu/k$ with ν being the average excitation frequency. Manoogian and Leclerc (74) indicate that $k\theta$ is the mean phonon energy for the material and so in the present analysis, the condition has been imposed that θ has the same value of all three curves. These three curves have been obtained with seven variables by θ, U_A, U_B, U_C, V_A, V_B and V_C. Under those conditions good fits were obtained to all curves as is shown in fig. 5.12.

The resulting values for the fitted curves are:

E_A: $E_{A_0} = 1.514eV$ $\theta = 505\ K$ $U_A = 5.2 \times 10^{-5}$ $V_A = 1.81 \times 10^{-4}$

E_B: $E_{B_0} = 1.578eV$ $\theta = 505\ K$ $U_B = 9.8 \times 10^{-5}$ $V_B = 2.28 \times 10^{-4}$

E_B: $E_{C_0} = 1.808eV$ $\theta = 505\ K$ $U_C = 4.1 \times 10^{-5}$ $V_C = 3.00 \times 10^{-4}$

It is of interest to compare these values with those obtained for the $CuGa(Se_{1-x}S_x)_2$ alloys. In that case, the value of θ varied from 771 K for $CuGaSe_2$ to 884 K for $CuGaS_2$. The value of $k\theta$ effectively measures the average bond strength in the material,

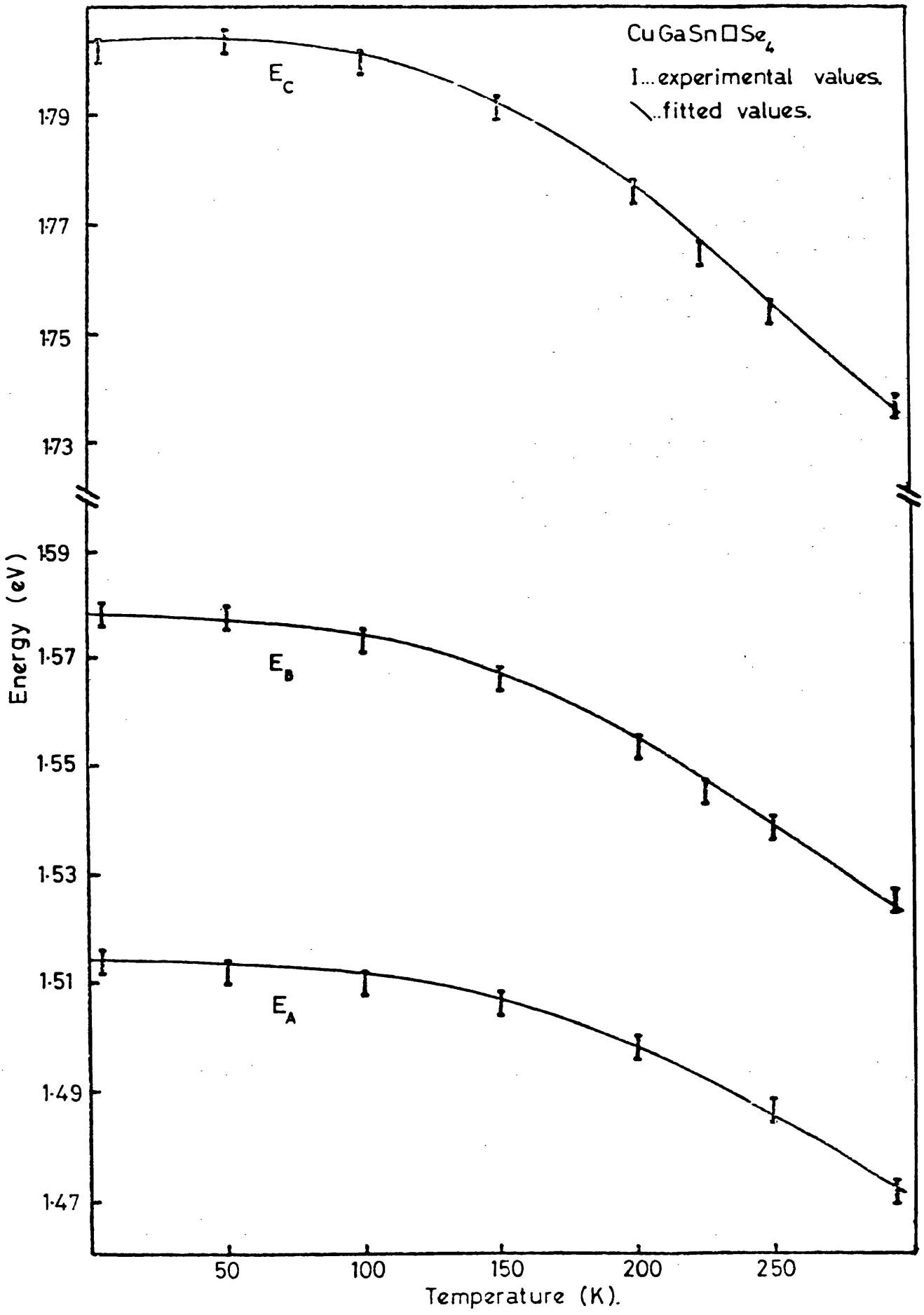

Fig. 5.12 Variation of E_A, E_B and E_C transitions with temperature.

so that a lower value of θ in $CuGaSn\square Se_4$ is not unreasonable since it is a defect structure with an average of one cation site for every four vacant.

The V term is the dynamic term due to phonon interaction again the V parameters here are smaller than those of $CuGa(Se_{1-x}S_x)_2$. The U term is a static or dilatation term and the present values are a factor of 3 or 4 less than those of the alloys. Both of these effects may be due to the softer constant of the defect structure. Here $V_A < V_B < V_C$ which is consistent with the variation in the $CuGa(Se_{1-x}S_x)_2$ case. In that case it was found that the U_B variation was approximately twice that of U_A. Here again U_A and U_C are approximately of the same size while U_B is roughly twice the value. The A valence bands on Γ_6 symmetry and B is Γ_7. It appears for the materials considered that the dilation effect is considerably larger for a Γ_7 band than a Γ_6 band.

For the linear part of $E_A(t)$, $E_B(t)$ and $E_C(t)$ above 190K we obtain

$$\frac{dE_A}{dt} = -2.7 \times 10^{-4} \text{ (eV/K)}, \frac{dE_B}{dt} = -3.4 \times 10^{-4} \text{(eV/K)}, \text{ and}$$

$$\frac{dE_C}{dt} = -4.2 \times 10^{-4} \text{ (eV/K)}.$$

Hoppfield (65) has discussed a model for the splitting of p-like levels in a nearly cubic crystal, including both the effects of a noncubic crystalline field and spin-orbit iteration. Within this so called, quasicubic model, the energies of the Γ_7 levels relative to the Γ_6 level in the valence band of a chalcopyrite crystal are given by:

$$E_{1,2} = -\frac{1}{2}(\Delta_{so}+\Delta_{cf}) \pm \frac{1}{2}[(\Delta_{so}+\Delta_{cf})^2 - \frac{8}{3}\Delta_{so}\Delta_{cf}]^{\frac{1}{2}} \qquad (5.34)$$

where Δ_{so} is the spin-orbit splitting of the valence bands in a cubic field, Δ_{cf} is the crystal-field splitting of the valence bands in the absence of spin-orbit interaction, $E_1 = E_A - E_B$ and $E_2 = E_C - E_B$. From the equation (5.34) we obtain

$$\Delta_{cf} = \frac{1}{2}\{(E_2+E_1) - [(E_2+E_1)^2 - 6E_1E_2]^{\frac{1}{2}}\} \qquad (5.35)$$

$$\Delta_{so} = \frac{1}{2}\{(E_2+E_1) + [(E_2+E_1)^2 - 6E_1E_2]^{\frac{1}{2}}\} \qquad (5.36)$$

Replacing the experimental values for E_1 and E_2 in the equations (5.35) and (5.36) we obtain the crystal field splitting and the spin-orbit splitting for each temperature and the results are shown in the table 5.6 and the variation with the temperature is sketched in Fig. 5.13.

TABLE 5.6 Variation of spin-orbit and crystal field splittings with the temperature

T(K)	Δ_{so}(eV)	Δ_{cf}(eV)
4	0.249	-0.088
50	0.248	-0.088
100	0.248	-0.086
150	0.246	-0.082
200	0.244	-0.075
250	0.236	-0.072
295	0.232	-0.071

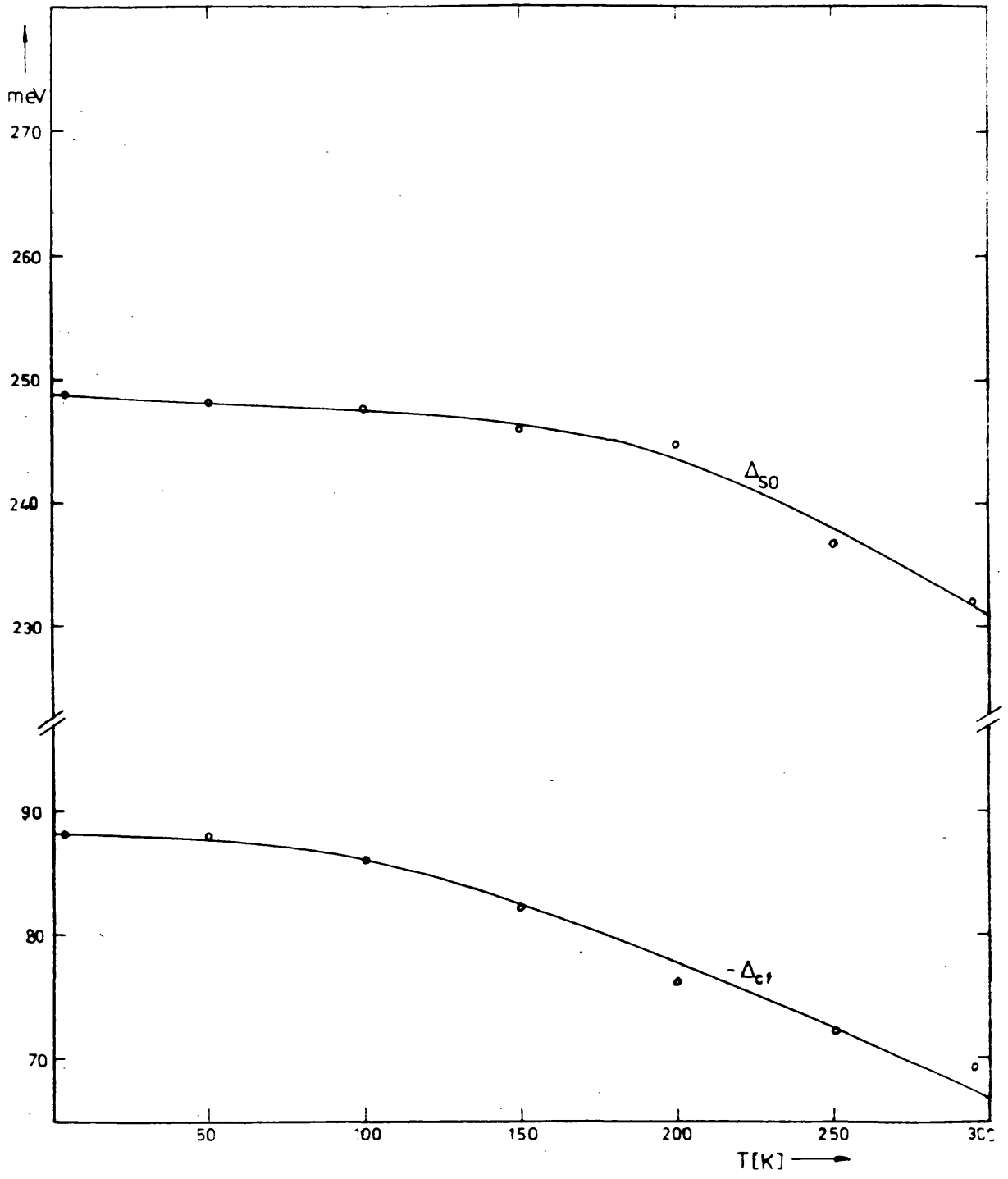

Fig. 5.13 Crystal field splitting and spin-orbit splitting versus temperature.

Theoretically Δ_{cf} is related to the c/a value by:

$$\Delta_{cf} = -\frac{3}{2} b \left[2 - \frac{c}{a}\right] \quad (eV) \qquad (5.37)$$

where b is the deformation potential. If b is assumed to be -1.0, the value for the ternary analogue $CuGaSe_2$, with c/a = 1.958, equation (5.37) gives Δ_{cf} = -0.063 eV for the room temperature value, as compared with the value from the experimental data of -0.071 eV is very good agreement.

CHAPTER 6

STUDY OF THE OPTICAL PROPERTIES OF I-III-IV-□-VI_4 SEMICONDUCTORS BY WAVELENGTH MODULATION

6.1 Introduction

The object of this chapter is to study the optical properties of $AgGaSn□Se_4$ and $CuGaGe□Se_4$ by wavelength modulation reflectance. Experimentally, the application of optical derivative spectroscopy to solids has greatly improved the resolution of optical spectra.

The common feature of all modulation techniques of optical spectroscopy is the measurement of the derivative of some optical property (e.g. absorption or reflectance) with respect to some parameter (75). The sensitivity in the measurement of this derivative can be made very large with the use of phase-sensitive detection techniques. The various methods that have been used can be divided into two general classes according to the choice of the parameter of differentiation: on the one hand we have wavelength modulation techniques (76, 77, 78, 79), in which the variable of differentiation is the wavelength of the radiation, and on the other we have sample modulation techniques, in which the variable of differentiation is an external perturbation applied to the sample (e.g. stress (80, 81, 82), temperature (83), electric field (76, 84) magnetic field (85)). In all these schemes except wavelength modulation the interpretation of the derivative spectrum depends very much on how the solid responds to the perturbation. Thus, in electroreflectance, we must

know how the band structure of the solid change with an applied electric field. In piezoreflectance and thermoreflectance, we must know the variation of the band structure as a function of pressure and temperature respectively. Unfortunately our knowledge on such properties of these quaternary compounds is limited. Therefore, the fact that no perturbation on the crystal is needed makes the wavelength modulation reflectance method most attractive to study the optical properties of these compounds. Since the wavelength modulation is simply the derivative of the normal spectrum, there is no ambiguity in the interpretation.

However, unlike the other modulation schemes, the wavelength modulation method requires careful construction of the experimental system in order to eliminate the huge background in the derivative spectrum. In this chapter, the principles of operation construction and the details of this technique are described.

6.2 The wavelength modulation spectrometer

The discussion of the change of a simple spectrometer into a modulation spectrometer will be limited to reflectivity measurements (the extension to absorption measurements is trivial). In order to extend wavelength modulation techniques to reflectivity measurements covering a wide spectral range, improvements of 100 to 1000 in rejection of the unwanted signal must be accomplished. The modifications necessary to convert the basic spectrometer to a wavelength modulation system will be first discussed, and then the double beam

detection system used for eliminating the unwanted signals due to the wavelength derivative of the incident light intensity will be described.

6.2.1 The refractor plate modulator

The first modification of the spectrometer is the convertion of the monochromator to a wavelength modulated light source. Several schemes such as vibrating mirrors and vibrating slits have been proposed as methods by which the radiation emerging from the exit slit of the monochromator may be wavelength modulated. The method suitable for use on the Spex monochromator is a technique suggested by Drews (86) and Gilgore, et al. (87). This technique utilizes the lateral displacement suffered by a beam of light passing through a dielectric slab at an oblique angle of incidence. This displacement produces a virtual displacement at the entrance slit of the monochromator as shown in fig. 6.1.

The beam is displaced by an amount:

$$\Delta d = T\left[1 - \frac{\cos\theta}{\sqrt{n^2-\sin^2\theta}}\right]\sin\theta \qquad (6.1)$$

where n is the index of refraction of the dielectric slab. If "D" is linear dispersion of the monochromator, then the change in wavelength $\Delta\lambda$ of the radiation emerging from the monochromator will be:

$$\Delta\lambda = D(\Delta d) \qquad (6.2)$$

If $\sin\theta$ is made to vary harmonically as:

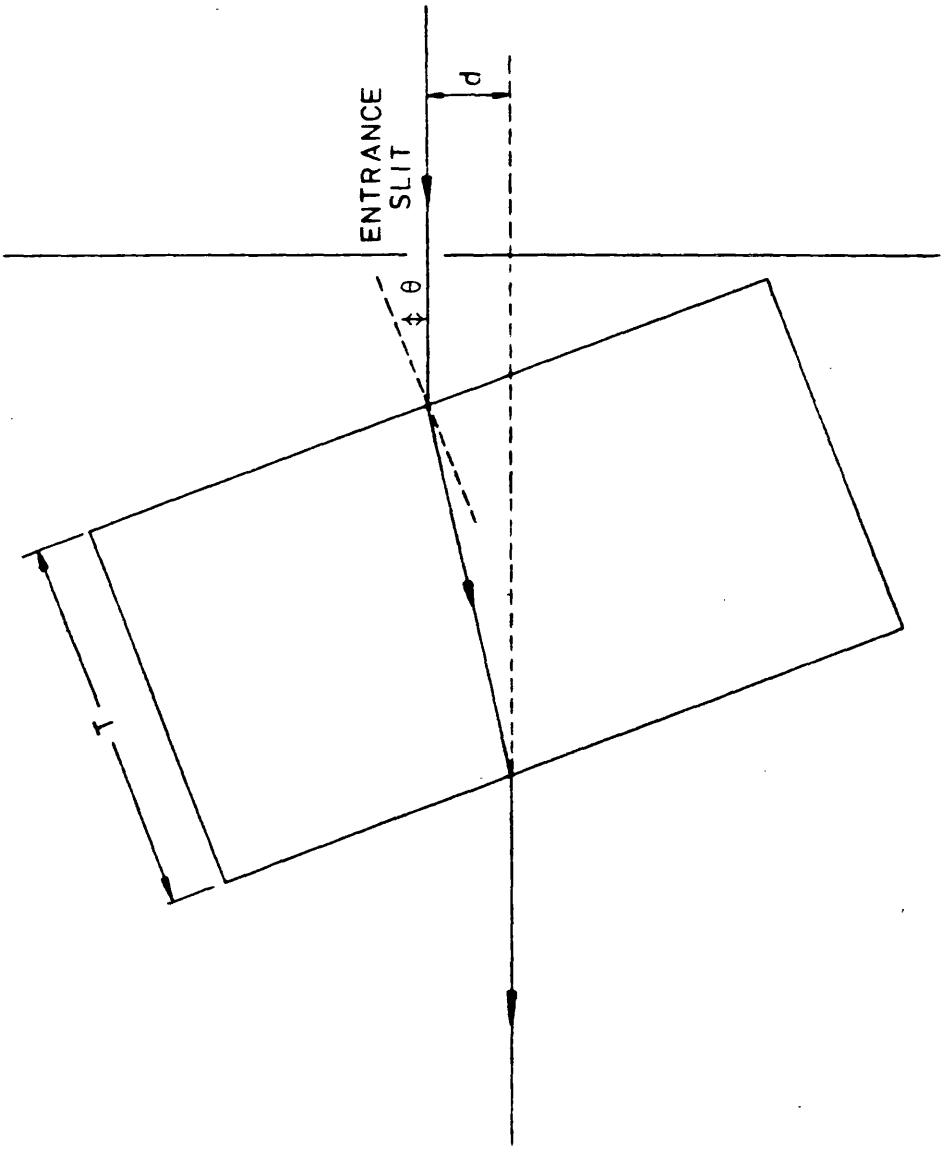

Figure 6.1 Schematic of refractor plate modulator

$$\sin\theta = B\cos(\Omega_2 t) \qquad (6.3)$$

Where $B << 1$, thus the wavelength of the light emerging from the exit slit of the monochromator will have the form:

$$\lambda = \lambda_o + \Delta\lambda = \lambda_o + D(\Delta d) \qquad (6.4)$$

where λ_o is the mean wavelength. From the equation 6.1 it follows that the wavelength λ should follow the relation

$$\lambda = \lambda_o + TD(1 - \frac{1}{n}) B\cos(\Omega_2 t) \qquad (6.5)$$

The equation (6.5) has the form:

$$\lambda = \lambda_o + a\cos(\Omega_2 t) \qquad (6.6)$$

where a is a constant equal to $(TD[1-n^{-1}]B)$.

Let us calculate the reflected (or transmitted) light intensity as a function of mean wavelength λ_o and time t. The light reflected (or transmitted) at a wavelength λ is a function of λ and represented by $I_R(\lambda)$ (or $I_T(\lambda) = I \equiv F(\lambda)$. The corresponding signal i_p from the photomultiplier is then given by (88):

$$i_p = C\ F(\lambda_o + a\cos\Omega_2 t) \qquad (6.7)$$

where C is a proportional constant and the spectral variation of photomultiplier and light output from the lamp have been ignored because of the small wavelength range considered. If 'a' is small then expanding equation 6.7 in terms of a $\sin\Omega_2 t$ (by Taylor's expansion), this equation becomes:

$$i_p = C\left[\left(F(\lambda_o) + \frac{a^2}{4}\frac{d^2F}{d\lambda^2}_o + \ldots\right) + \right.$$

$$+ \left(a\frac{dF}{d\lambda}_o + \frac{a^3}{12}\frac{d^3F}{d\lambda^3}_o + \ldots\right) \sin \Omega_2 t +$$

$$\left. + \left(-\frac{a^2}{4}\frac{d^2F}{d\lambda^2}_o + \ldots\right)\cos \Omega_2 t + \ldots\right] \qquad (6.8)$$

The signal from the photomultiplier, is fed into a differential amplifier and then into the phase-sensitive detector (see figure 6.2), therefore contains one component of angular frequenct Ω_2, and another component of angular frequency $2\Omega_2$. Two different cases will be considered:

(a) When the reference signal is fed to the phase-sensitive detector is at frequency Ω_2, then the dc output S_{Ω_2} from the phase-sensitive detector is given by

$$S_{\Omega_2} = A\left[a\frac{dF}{d\lambda}_o + \frac{a^3}{12}\frac{d^3F}{d\lambda^3}_o + \ldots\right] \qquad (6.9)$$

where A is a proportional constant. Thus if a is small

$$S_{\Omega_2} \approx (A\ a)\frac{dF}{d\lambda}_o \qquad (6.10)$$

(b) When the reference signal frequency is doubled and is in phase with the $\cos(2\Omega_2 t)$ component of the photomultiplier output then the dc output $S_{2\Omega_2}$ is given by

$$S_{2\Omega_2} = B\left[\frac{a^2}{4}\frac{d^2F}{d\lambda^2}_o + \text{higher order terms}\right] \qquad (6.11)$$

where B is a proportional constant. Thus if a is small

$$S_{2\Omega_2} \approx \left(B \frac{a^2}{4}\right) \frac{d^2F}{d\lambda_o^2} \qquad (6.12)$$

Thus, if the experimental arrangements leading to equations (6.10) or (6.12) are used, the signal S from the output of the phase-sensitive detector is proportional to either the first derivative (F') or the second derivative (F'').

6.2.2 The double beam detection system

The major modification required to adapt the basic spectrometer for use in wavelength modulation measurements is concerned with the elimination of the background. In reflectance experiment the reflected light intensity I_R is given by:

$$I_R = I_o R \qquad (6.13)$$

where R is the sample reflectivity and I_o is the incident light intensity. The normalized derivative of I_R with respect to the wavelength is given by:

$$\frac{1}{R} \frac{dI_R}{d\lambda} = \frac{1}{R} \frac{dR}{d\lambda} + \frac{1}{I_o} \frac{dI_o}{d\lambda} \qquad (6.14)$$

The equation (6.14) contains two terms. The first term is the normalized derivative of the sample reflectivity and is the quantity we wish to determine. The second term is the normalized derivative of the incident light intensity and makes an undesirable contribution to the wavelength modulation signal. With the double beam detection system the values of

$I_R^{-1}\ (dI_R/d\lambda)$ and $I_o^{-1}(dI_o/d\lambda)$ can be simultaneously measured and obtaining (by electronic subtration)

$$\frac{1}{R}\frac{dR}{d\lambda} = \frac{1}{I_R}\frac{dI_R}{d\lambda} - \frac{1}{I_o}\frac{dI_o}{d\lambda} \qquad (6.15)$$

In order to perform the subtraction, a double beam detection system has been used for the basic spectrometer (78, 89, 90). The double beam detection system utilizes two detectors as shown in figure 6.2. In this system the wavelength modulated light emerging from the monochromator is divided into two beams by a neutral beam splitter. The reflected light is focussed on a reference detector while the transmitted light is reflected from the sample to a second detector. The light reaching the sample photomultiplier contains the a.c. signal (at Ω_2) that is proportional to

$$S_s(\Omega_2) = [R_s(1-R_b)I_o' + I_o(1-R_b)R_s'] \Delta\lambda \qquad (6.16)$$

Where R_b, R_s, I_o and $\Delta\lambda$ are the beam splitter reflectivity, sample reflectivity, incident light, and wavelength modulation amplitude, respectively. In this equation we assumed that R_b is independent of wavelength and that $\Delta\lambda$ is small enough so that only first derivatives terms are important. The d.c. signal from this detector is proportional to

$$S_s(\Omega_2 = 0) = (1 - R_b)R_s I_o \qquad (6.17)$$

Hence, if we normalize the a.c. signal by holding the d.c. signal constant with the electronic servo system shown in detail in the figure 6.3, then the signal at frequency Ω_2

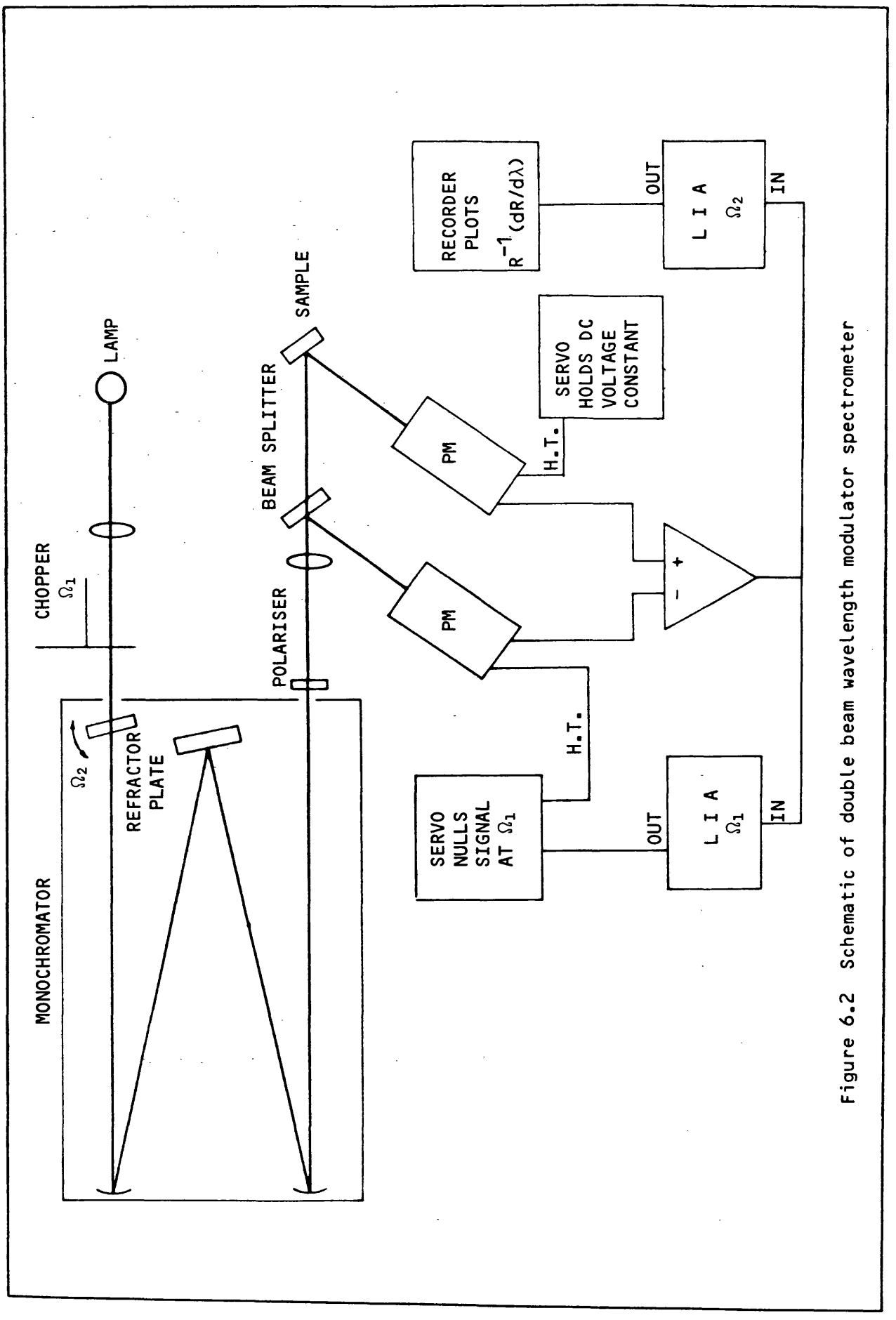

Figure 6.2 Schematic of double beam wavelength modulator spectrometer

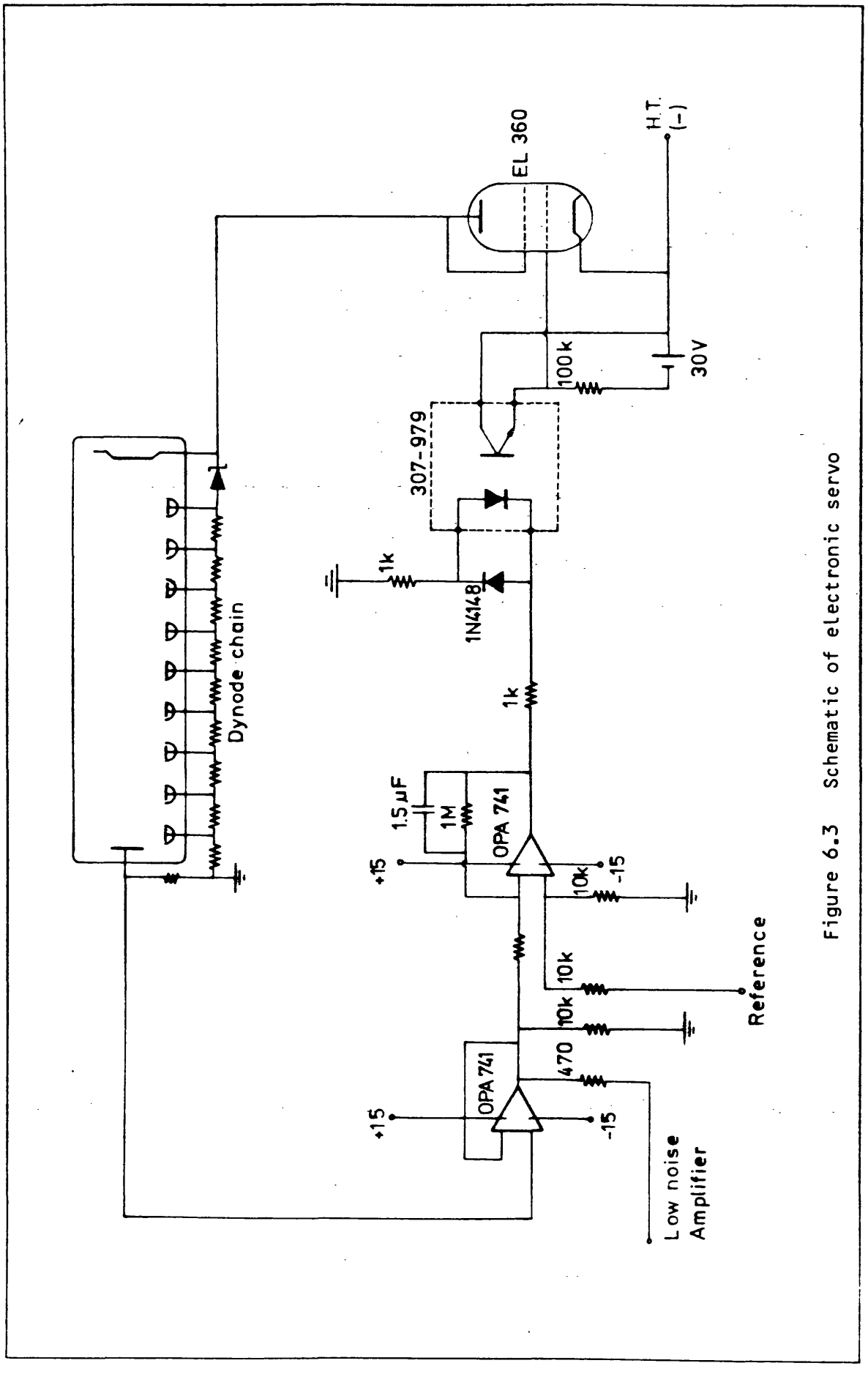

Figure 6.3 Schematic of electronic servo

becomes proportional to

$$S_s(\Omega_2) = \left[\frac{1}{I_o}\frac{dI_o}{d\lambda} + \frac{1}{R_s}\frac{dR_s}{d\lambda}\right]\Delta\lambda \qquad (6.18)$$

From similar considerations applied to the reference photomultiplier it is apparent that the normalized signal from this detector at frequency Ω_2 is proportional to

$$S_R(\Omega_2) = \left[\frac{1}{I_o}\frac{dI_o}{d\lambda}\right]\Delta\lambda \qquad (6.19)$$

But the proportionality constant is not necessarily the same for both detectors; particularly when two different kinds of photomultipliers are used. We can overcome this difficulty by the following procedure. The sample detector is normalized to a d.c. signal (30mV). A wavelength independent modulation of the incident intensity (Ω_1 = 577Hz) is added at a frequency Ω_1 different from the wavelength modulation frequency (Ω_2 = 100 Hz). Hence, the normalization of the two detectors will match if the two signals at Ω_1 are equal. We use a differential amplifier to obtain the difference of the two signals. The difference signal at frequency Ω_1 is measured with a lock-in amplifier (LIA) which drives an electronic servo system to adjust the gain of the reference photomultiplier to null the difference signal at Ω_1. A second LIA is used to measure the component of the difference signal at frequency Ω_2 which (according to equations 6.18 and 6.19) is proportional ro $R_s^{-1}(dR_s/d\lambda)$. The output of this second LIA is plotted continuously with a chart recorder.

The uncompensated polarization in a double beam system can account for background signals. This problem can be eliminated by placing a polarizer at the exit slit of the monochromator with the pass axis oriented either parallel or perpendicular to the plane of incidence. Care must also be taken to insure that the angles of incidence of the light sample and beam splitter are kept small to avoid additional signals due to the wavelength dependence of the Brewster angle.

6.3 Experimental results

In figures 6.4 and 6.5 the derivative spectra dR(E)/RdE of $AgGaSn\square Se_4$ and $CuGaGe\square Se_4$ are shown at room temperature (295 K).

The spectra of these two crystals are are very much alike, reflecting the similarity of their band structure. The discussion of the band structure of these quaternary compounds was made in chapter 5. Following the notation of chapter 5, we labelled the three peaks E_A, E_B and E_C to transitions to a single conduction band from three closely spaced valence bands derived from the p-like Γ_{15} level in zinc blende compounds. The three fold degeneracy is completely lifted by the combined influences of spin-orbit interaction and noncubic crystalline field.

In table 6.1 the list of the positions of all the reflectivity peaks (zeros with negative slope in the $R^{-1}(dR/d\lambda)$ spectrum) obtained for these two compounds in the range of energy between 1.5 to 3.0 eV.

TABLE 6.1

ROOM TEMPERATURE VALENCE BAND PARAMETERS OF $AgGaSn\square Se_4$ AND $CuGaGe\square Se_4$ CRYSTALS (IN eV)

Material	E_A	E_B	E_C	$-\Delta_{cf}$(expt)	$-\Delta_{cf}$(Theory)	Δ_{SO}
$AgGaSn\square Se_4$	1.680	1.930	2.120	0.298	0.230	0.238
$CuGaGe\square Se_4$	1.856	2.020	2.160	0.200	0.232	0.174

We now proceed to comment on the room-temperature spectrum of each semiconductor separately.

6.3.1 $AgGaSn\square Se_4$

The figure 6.4 shows the derivative spectrum of this material. The value for the energy gap obtained in the derivative spectrum (E_A = 1.680 eV) is in very good agreement with that obtained by absorption measurement (E_g = 1.685 eV) in Chapter 5 (Table 5.3).

In Chapter 5 we used the Hoppfield model to explain the splitting of p-like levels in nearly cubic cystals, including both the effects of non-cubic crystalline field and spin-orbit interaction. The equations 5.34, 5.35 and 5.36 are used in order to calculate the crystal field splitting (Δ_{cf}) and spin orbit splitting (Δ_{SO}) reported in the Table 6.1.

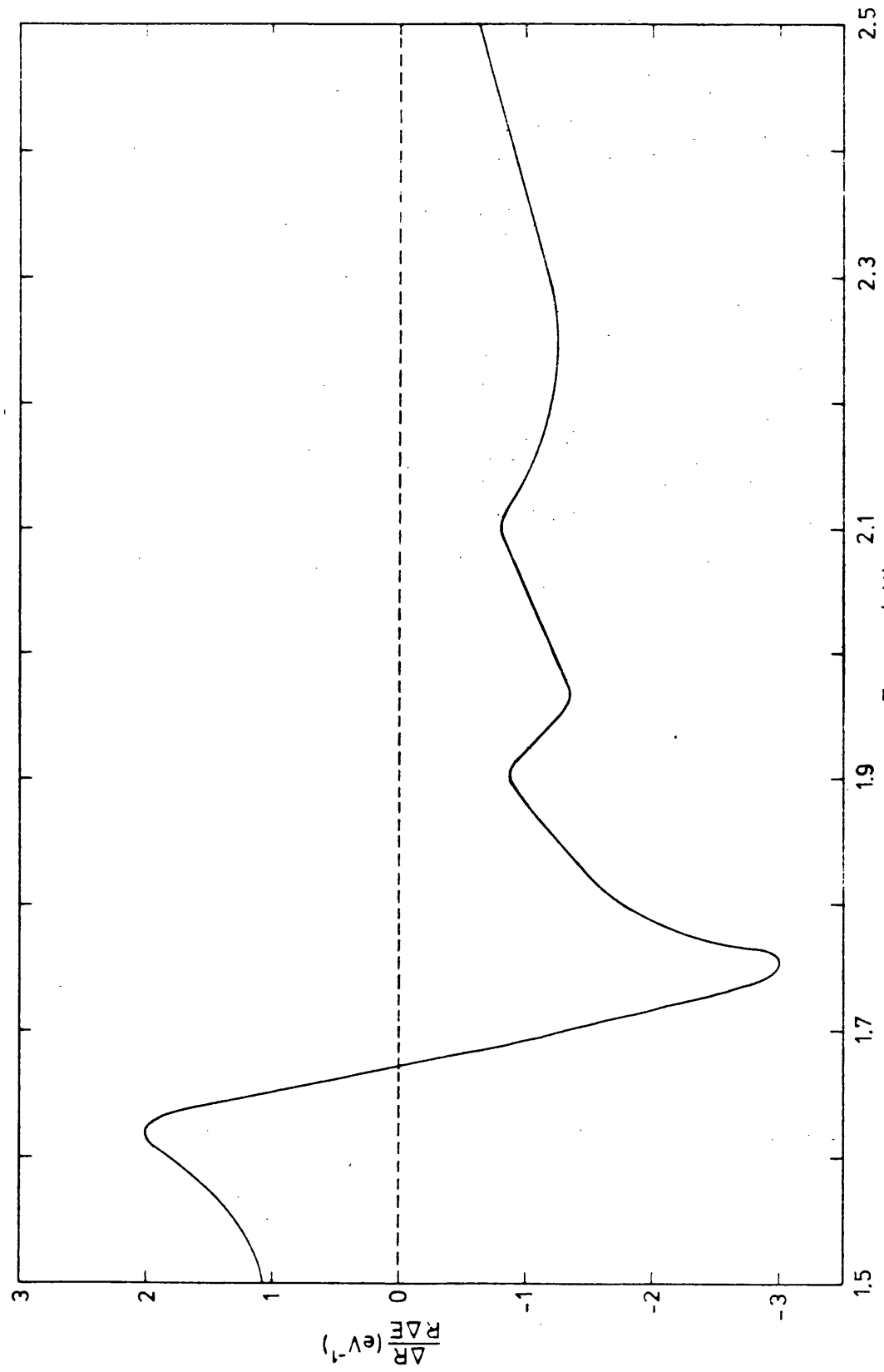

Figure 6.4 Logarithmic derivative of the reflectivity spectrum of $AgGaSnOSe_4$ at 295K

Because Δ_{cf} is dominated by the built-in lattice compression in these quaternary materials, in a similar manner to the analogue ternary compounds, equation 5.37 was used to calculate the Δ_{cf} (theory), from the c/a value ($\Delta_{cf} = -(3/2)$ b[2-c/a]). The value of the deformation potential b is assumed to be -1.0 (eV), the value for the ternary analogue ($AgGaSe_2$). From chapter 3 (Table 3.1) the value of c/a is 1.849. Using this value the equation 5.37 gives Δ_{cf} = -0.230eV at room temperature, as compared with the value from the experimental data of -0.298 eV.

6.3.2 $CuGaGe\square Se_4$

The figure 6.5 shows the derivative spectrum of this material. Comparing the value of the energy gap obtained by the derivative spectrum (E_A = 1.856 eV) and the value obtained by absorption measurement (E_g = 1.854 eV Table 5.3) are in very good agreement. The value of the crystal field splitting (Δ_{cf}) experimental (0.200 eV) and theory value (0.232) are also in very good agreement.

The derivative spectra show clear improvement of resolution over the conventional technique. We can consistently assign all the observed reflectivity peaks to proper transitions between bands. Values of spin-orbit and crystal field splittings at the Γ symmetry point in the B.Z. can then be deduced. Results agree well with theoretical calculations.

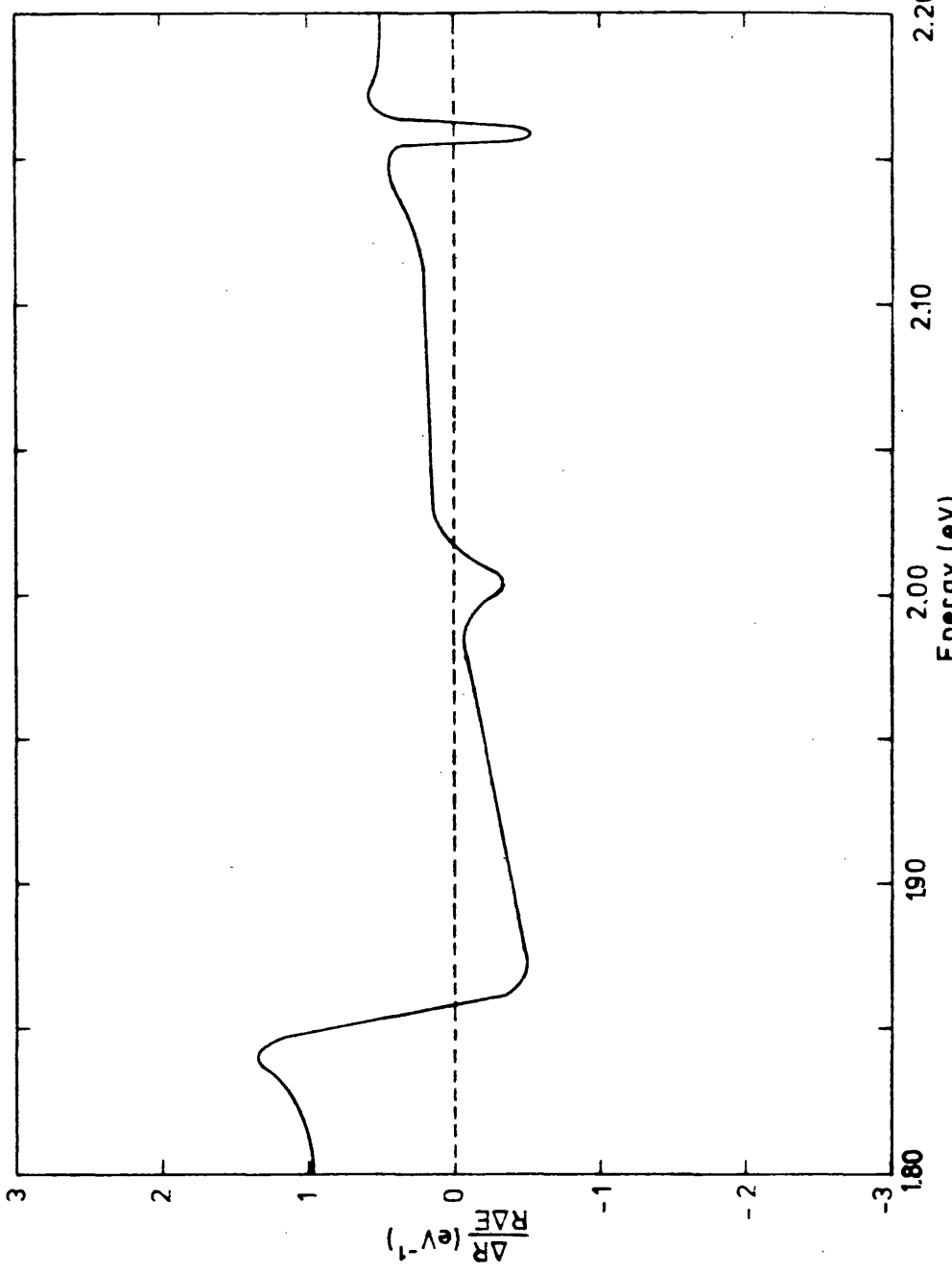

Figure 6.5 Logarithmic derivative of the reflectivity spectrum of $CuGaGeSe_4$ at 295K

CHAPTER 7

CONCLUSIONS

7.1 Synthesis, growth and x-ray analysis

The quaternary normal and defect adamantine compounds can be considered to be the natural extensions of the ternaries because of very close structural analogies. In table 2.1 and 2.2 are listed all the quaternary compounds synthesized up till now, with the respective structure, space group and lattice parameters. The quaternary compounds are divided into two main groups, the normal and defect adamantine structures. In the normal quaternary adamantine compounds sixty two compounds have the composition I_2-II-IV-VI_4, twenty four the composition I-II_2-III-VI_4 and two the composition I_4-II-IV_2-VI_7. In the defect quaternary adamantine compounds twenty six have the composition I-III-IV-□-VI_4 and three the composition I-III_2-□-VI_3-VII. These 117 quaternary adamantine compounds should be enlarged with many new compounds. Many of these new quaternary adamantine phases are proposed in chapter 2.

From the systematic study of the quaternary defect compounds of composition I-III-IV-□-VI_4, three different structures have been found. One is the partially ordered defect chalcopyrite structure, the second is the super-ionic spinel structure. The third one is the hitherto unknown structure of $AgGaGeS_4$, with orthorhombic symmetry. Many tellurides do not appear to be single phase at this composition. For twelve selenide compounds and three of the sulphur compounds, the structure was found to be tetragonal. The (c/a) ratio of approximately 2 was confirmed

for all of tetragonal compounds by a study of the ordering lines observed in the powder photographs. In all cases except $CuGaSn\square Se_4$ and $CuAlSn\square Se_4$ the quaternary unit cell is smaller than that of the ternary one. This is presumably because the vacancies allow the atoms to pack slightly more closely.

The c/a ratio for the normal quaternary compounds is bigger than the defect quaternary. That is the indication that the structure of the defect quaternary compounds is more distorted than the structure of the normal quaternary compounds, and bigger non-linear effects should be expected in the defect quaternary compounds.

$CuGaSn\square Se_4$ was chosen as the archetypal compound of quaternary defect adamantine compounds to study the crystal structure of these compounds. The structure was found to be the partially ordered defect chalcopyrite structure, space group $I\bar{4}2d$ (D_{2d}^{12}) and point positions was found for an ABX_2 with:

A = Cu and Ga at random in (a) $0,0,0$; $0,\frac{1}{2},\frac{1}{4}$; $\frac{1}{2},\frac{1}{2},\frac{1}{2}$; $\frac{1}{2},0,\frac{3}{4}$

B = Sn and $\square$ at random in (b) $0,0,\frac{1}{2}$; $0,\frac{1}{2},\frac{3}{4}$; $\frac{1}{2},\frac{1}{2},0$; $\frac{1}{2},0,\frac{1}{4}$

C = Se in (d) $x,\frac{1}{4},\frac{1}{8}$; $\bar{x},\frac{3}{4},\frac{1}{8}$; $\frac{3}{4},x,\frac{7}{8}$; $\frac{1}{4},\bar{x},\frac{7}{8}$

The parameter x, locating the position of the Se atoms in the unit cell was found to be 0.2571. It will be interesting to discover whether the vacancy always teams up with the group IV atom in the chalcopyrite structure, whether complete ordering is possible under other growth conditions and if so with what structure.

The results of the high temperature lattice parameter determination in $CuGaSn\square Se_4$ are interesting and this is worth extending to other defect quaternary adamantine compounds.
A second phase at 590K was found by differential thermal analysis,

x-ray analysis indicated that this second phase is probably the dichalcogenide $SnSe_2$. The increase in the tetragonal compression with temperature could be explained in terms of the different thermal expansions of the A-Se [A = $\frac{1}{2}$(Cu+Ga)] and B-Se [B = $\frac{1}{2}$(Sn + □)] bonds.

A modification of Pendölofen vapour transport was described in chapter 3 produced single crystals which were large enough for optical and x-ray measurements. This interesting technique proved that it is possible to transport simultaneiously three non-votatile metals in the closed tube.

7.2 Electronic band structure

We propose the same band structure as the I-III-VI_2 chalcopyrite compounds for the I-III-IV-□-VI_4 defect quaternary adamantine compounds, because this model explains our experimental results very well and also because these two groups of the adamantine family have very closely related structures. The figure 5.6 illustrates the band structure of the chalcopyrite compounds at the centre of Brillouin zones. Fitting the energy band structure of zinc blende compounds in to smaller chalcopyrite Brillouin zone gives a general understanding of the band structure of I-III-VI_2 and I-III-IV-□-VI_4 compounds. The combined action of spin-orbit coupling and tetragonal field completely removes the triple orbital degeneracy of the zinc blende Γ_{15} valence bands. The five-fold degenerate d-levels split into a three-fold Γ_{15} and two-fold Γ_{12} in a tetrahedral field. The spin-orbit contribution splits the p-like Γ_{15} into Γ_8 and Γ_7 levels while the d-like Γ_{15} gives Γ_7 and Γ_8 in reverse order. The Γ_8 band

derived from the d-like Γ_{15} band will force the p-like Γ_8 upwards reducing the band gap energy. Likewise, the close proximity of the two Γ_7 bands will reduce the spin orbit splitting of the p-levels in chalcopyrite.

The results of absorption measurements in the region of the lowest direct transition shows the rise the absorption coefficients (α) for these defect quaternary materials follows the relations 5.32. This is a general feature of direct gap semiconductors. There was found to be systematic variation of both energy gaps of the quaternaries related with the same analogous ternary. With the inclusion of the larger atom of Sn (compared with Ge atom) there is an observed decrease in the energy gap. The inclusion of the atom Ge increases the energy gap compared with the related ternary. Another change is the higher value of the energy gap for silver than copper compounds. This is probably connected with a lower electronegativity value for silver than for copper.

The reflectance and wavelength modulation reflectance method gave structure at energies above the band gap. The experimental limit of observation was at 3.0eV. It should be very interesting to do these measurements above 3.0eV in order to observe the complete electronic structure of these materials.

The other goal that has been achieved in this work is the construction of a very sensitive wavelength modulation spectrometer. The derivative spectra show clear improvement of resolution over the conventional technique. We can consistently assign all the observed reflectivity peaks (zeros with negative slope in the $R^{-1}(dR/d\lambda)$ spectrum) to proper transitions between bands. Values of spin-orbit and crystal field splittings at the centre

of the brillouin zones was calculated. Results agree well with theoretical calculations.

Our measurements at various temperatures also yield valuable information about the temperature dependence of the band structure. All the reflectivity peaks shift to higher energies at lower temperatures. There are two kinds of contribution to this effect; one is due to the effect of volume thermal expansion of the crystal, and the other one arises from the electron-phonon interactions in the crystal.

7.3 Possible applications

The figure 7.1 shows a selection of various classes of semiconductive compounds ordered by their energy gap Eg. As pointed out by Loferski (91) and Shockley and Queisser (92), H.J.Bachmann et al (93), the optimum Eg for solar power conversion is in the vicinity of 1.4eV varying by ± 0.2eV depending on geometrical factors and on absorption conditions in the atmosphere. There exist several compounds, e.g. GaAs, InP, CdTe, $CuInS_2$, $AgInGe\square Se_4$, $CuGaSn\square Se_4$ and $CuInGe\square Se_4$, within this optimum energy range which is indicated in figure 7.1 as a cross hatched band. The dashed area in this figure corresponds to the visible region. All these materials have a direct band gap which makes them particularly suited for polycrystalline thin film applications since the absorption length for radiation of energy near Eg in such materials is of the order of $\sim 1\mu m$ so that a grain size of similar dimensions suffices to avoid boundaries in the minority carrier diffusion path to the p-n junction.

A basic requirement for the fabrication of a heterojunction

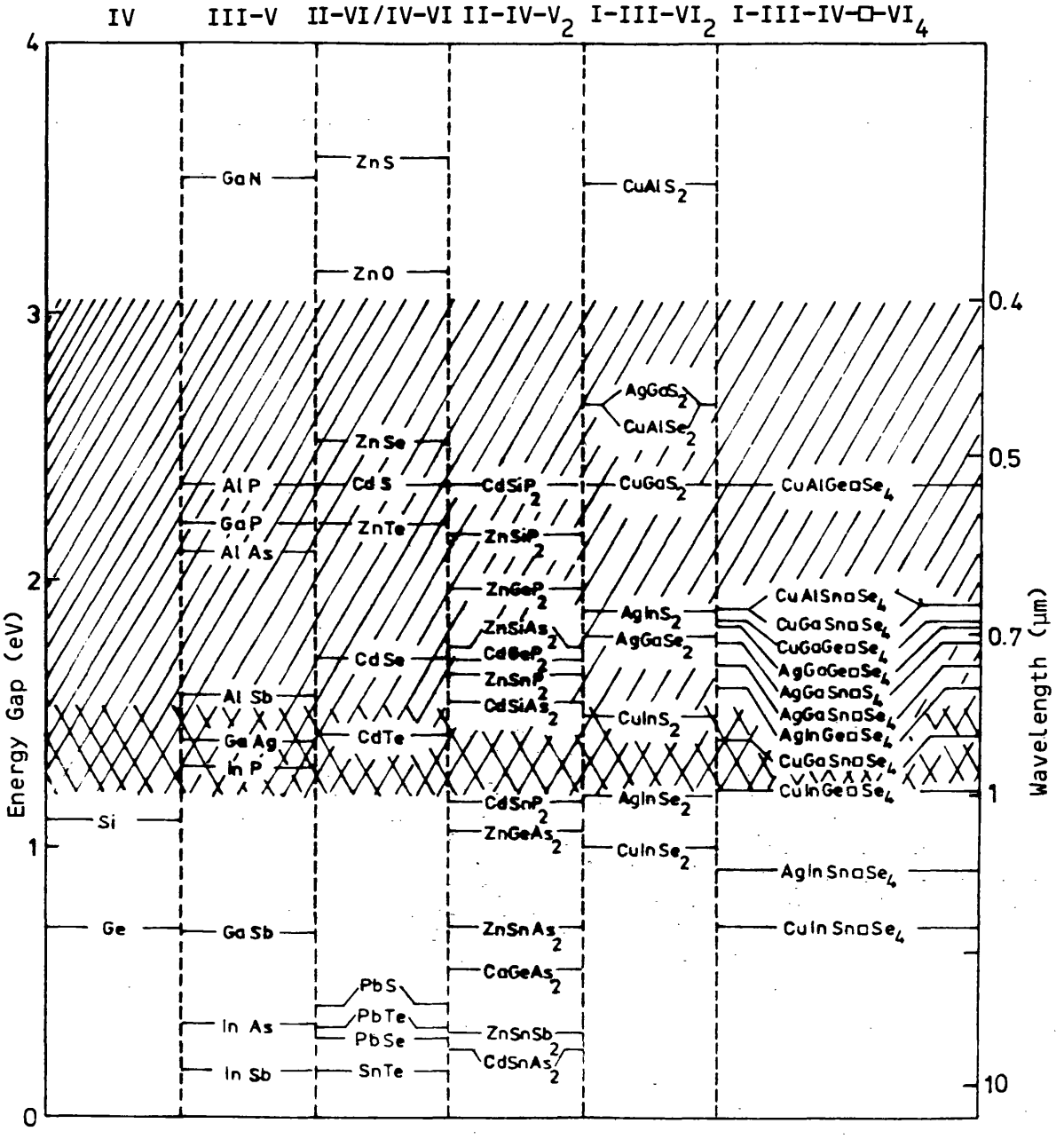

Figure 7.1. Energy gap of compound semiconductors at 300K. The cross hatched band shows the optimum energy range for solar cell applications and the dashed area corresponds to the visible region.

is that the lattices of the two materials match each other. Figure 7.2 shows the compounds in figure 7.1 ordered by the lattice parameters. As can be seen it is, in principle, always possible to select a suitable substrate material for each of the defect quaternary compounds assuming a sufficiently low lattice misfit to grow high-quality epitaxial layers. For the preparation of polycrystalline thin film solar cells, generally a good lattice match is required for the crystallographic orientation that contributes to the interface of the p-n junction. For single crystal devices good lattice match on one particular crystallographic plane is sufficient in noncubic lattices.

Virtually no work has been done on the doping and electrical properties of these optoelectronic materials, so it is hard to say what practical applications may emergy. However they do provide a scientifically interesting extension of the range of adamantine semiconductors.

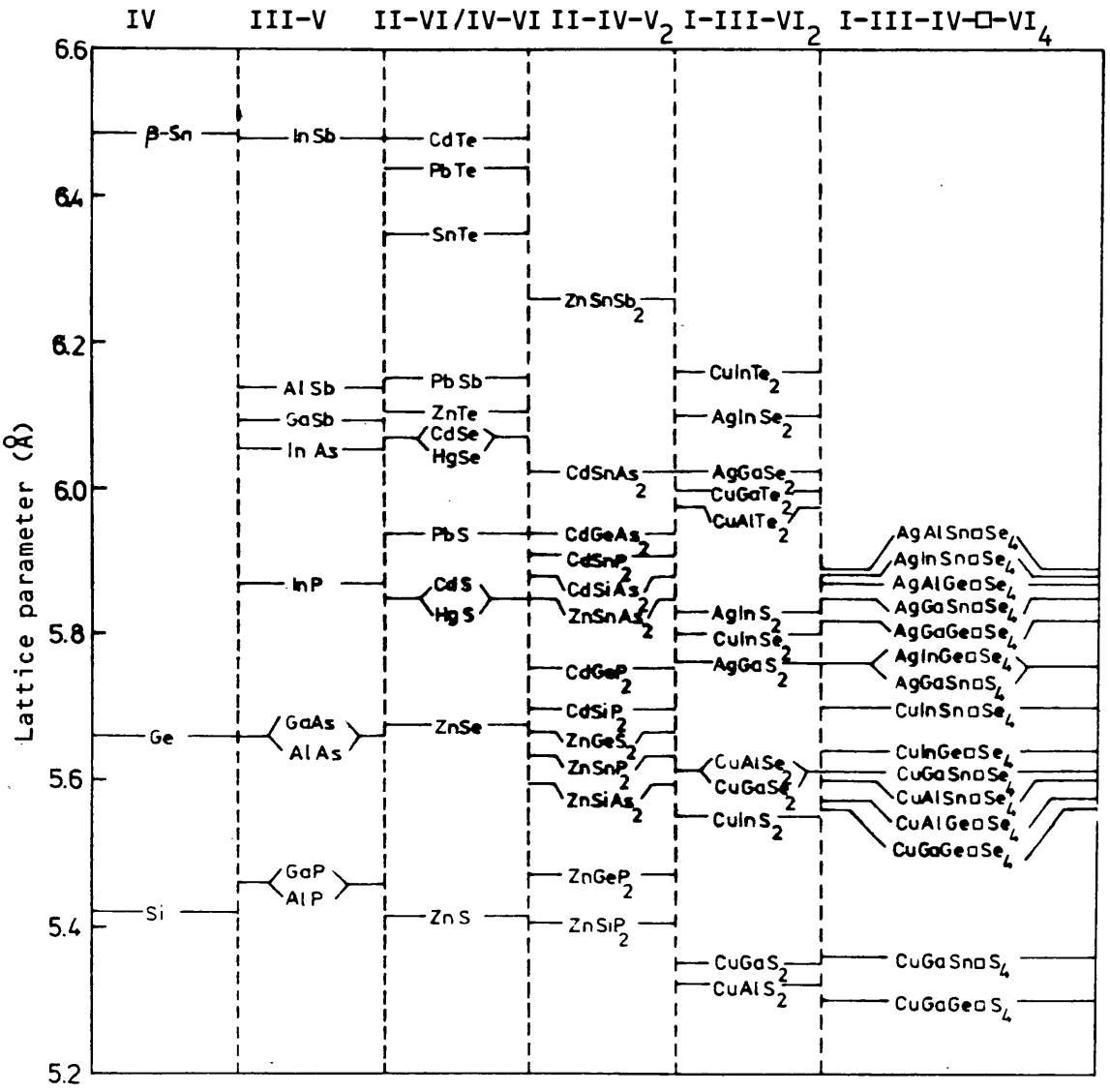

Figure 7.2 Lattice parameters of compound semiconductors at 300K

REFERENCES

1. E. Parthé, "Crystal Chemistry of Tetrahedral Compounds", Gordon and Breach (1964).

2. T.Ohachi and B.R.Pamplin, Institute of Physics Conferences Series 35, 21-34 (1977).

3. B.R.Pamplin, Nature 188, 136-137 (1960).

4. E.Parthé, Z.Krist. 119, 204-225 (1963).

5. C.H.L.Goodman, J.Phys.Chem.Solids 6, No.4, 305-314 (1958).

6. J.L.Shay and J.H.Wernick, "Ternary chalcopyrite semiconductors: growth, electronic properties and applications", Pergamon Press, Oxford (1975).

7. Brockway, L.O. Z.Kristallogr. 89, 434 (1934)

8. Hahn, H. and Schulze, H. Naturwissenschaften 52, 426 (1965).

9. Nitshe, R., Sargent, D.F. and Wild, P. J.Crystal Growth, 1, 52 (1967).

10. E.Parthé, K.Yuon and R.H.Deitch, Acta Cryst. B25, 1164 (1969).

11. W.Schäfer and R.Nitsche. Mat.Res.Bull. 9, 645-654 (1974).

12. U.Ganiel, E.Hermon and S.Shtrikman. J.Phys.Chem.Solids. 33, 1873-1878 (1972).

13. L.Guen and W.S.Glaunsinger, Journal of Solid State Chemistry, 35, 10-21 (1980).

14. L.K.Samanta and G.C.Bhar. Phys. Stat. Sol. 41, 331 (1977).

15. M.S.Donald and Aaron Wold. Mat.Res.Bull. 12, 111-114, (1977).

16. J. Allemand and M.Winterberger. Bull.Soc.Fr.Mineral.Cristallogr. 93, 14 (1970).

17. R.Caye, Y.Laurent, P.Picot, R.Pierrot et C.Lévi. Bull.Soc.Fr.Minéral.Crystallogr. 91, 383-387. (1968).

18. P.Tarte et R.C.Cahay. R.Acad.Sci.Paris 271, 777-779 (1970).

19. C.A.Joubert-Bettan, R.Lachenal, E.F.Bertaut et E.Parthé. J.Solid State State Chem. 1, 1-5 (1969).

20. E.F.Apple. J.Electrochem.Sco.105, 251-255 (1958).

21. L. Garbato and P.Manca. Mat.Res.Ball. 9, 511-518, (1974)

22. J.C.Woolley & E.W.Williams. J.Electrochem.Soc. 113, 899-901 (1966).

23. W.Schäfer, K. Scheunemann and R.Nitsche. Mat. Res.Bull, 15, 933-937 (1980).

24. H.Hahn and G.Strick. Naturwissenschaften 54, 225 (1967).

25. B.R.Pamplin, T.Ohachi, S.Maeda, P.Negrete, T.P.Elworthy, R.Sanderson and H.J.Whitlow. Institute of Physics Conferences Seriew 35, 35-42 (1977).

26. O.H.Hughes, J.C.Woolley, S.A.Lopéz and B.R.Pamplin. Solid State Comm. 35, 573-575 (1980).

27. B.R.Pamplin, S.A.Lopez, R.C.J.Draper, J.C.Wooley and D.H.Hughes. Sixth International Conference on Crystal Growth, Moscow. Extended abstracts 1, 384-385, (1980).

28. H.Hahn and W.Nickels. Z.Anorg.Allg.Chem. 303, 107-112 (1960).

29. T.Ohachi and B.R.Pamplin. "Ternary Compounds". Institute of Physics Conference series 35, 21-34 (1977).

30. H.Hahn and G.Strick. Naturwissen, 54, 225 (1967).

31. G.Strick and H.Hahn. Z. Anorg. a Allge. Chemie, 357, 338.

32. B.R.Pamplin, T.Ohachi, S.Macda, P.Negrete, T.P.Elworthy, R.Sanderson and H.J.Whitlow. "Ternary Compounds". Institute of Physics Conference Series, 35, 35 (1977).

33. J.B.Nelson, and D.P.Riley. Proc. Phys.Soc. (London) 57, 160 (1945).

34. Y.L.Lee. Ph.D. thesis, Bath University (1970).

35. R.C.Evans, "An Introduction to Crystal Chemistry", Cambridge University Press (1952).

36. E.Kaldis, "Crystal Growth Theory & Techniques" Vol. 1. Edited by C.H.L.Goodman, Plenum Press (1974).

37. A.F.Fray and S.Nielson. Brit.J.Appl.Phys. 12, 603 (1961).

38. H.Scholz. Acta.Electronica, 17, 69-73 (1974).

39. B.R.Pamplin, T.Kiyosawa and K.Masumato, Progress in Crystal Growth and Characterisation. 1, 331 (1979).

40. Rauben Rudman. Journal of Chemical Education. (1967).

41. T.Barrett and T.B.Massalski. "Structure of Metals". Pergamon Press. (1980).

42. A.J.C.Wilson. "Elements of X-ray Crystallography". Addison-Wesley Publishing Company (1970).

43. M.J.Buerger. "The Photography of the Reciprocal Lattice", Am.Soc.X-ray and Electron Diffraction Monograph No. 1 (1944).

44. M.H.Buerger. "The Precession Method". John Wiley & Sons Inc. (1964).

45. P.B.Braun and A.J. Van Bommel. Philips Technical Review, 22, 127-129 (1960-61).

46. J.M.Stewart, F.A.Kundell and J.C.Baldwin. X-ray System of Crystallographic Programs. Version 76. University of Maryland (1976).

47. H.G.Brühl, H.Newmann and G.Kühn. Solid State Comm. 34, 225 - 272 (1980).

48. S.C.Abrahams & J.L.Bernstein. J.Chem.Phys. 52 (1970).

49. A.Miller, R.G.Humphreys & B.Chapman. Appl.Phys.Suppl. 36, C3-31 (1975).

50. W.B.Pearson. "Handbook of Lattice Spacings and Structures of Metals and Alloys", Vol. 2, Pergamon Press, Oxford (1967).

51. F.D.Enck and J.G.Dommel. J.App.Phys. 36, 839 (1965).

52. D.L.Greenaway and G.Harbeke. "Optical Properties and Band Structure of Semiconductors". Pergamon Press. Oxford (1968).

53. C.Kittel. "Introduction to Solid State Physics" John Wiley & Sons. Inc. (1976).

54. L.Van Hove. Phys. Rev. 89, 1189 (1953).

55. J.C.Phillips. Phys. Rev. 104, 1263 (1956).

56. Bassani and P.Parravicini. "Electronic States and Optical Transitions in Solids". Pergamon Press (1975).

57. Manuel Cardona. "Modulation Spectroscopy" Solid State Physics. Sup. 11. Academic Press (1969).

58. Bardeen, F.J.Blatt and L.J.Hall. "Photoconductivity Conference" John Wiley (1957).

59. J.S.Toll. Phys.Rev. 104, 1760-70 (1956).

60. H.R.Phillip & H.Ehrenreich. Phys.Rev. 129, 1550 (1963).

61. D.M.Roessler. Brit. J.Appl.Phys. 17, 1313 (1966).

62. M.Cardona. "Optical Properties of Solids". Plenum Press. (1969). (S.Nudelman and S.Mitra, eds.).

63. E.J.Johnson. "Semiconductors and Semimetals" edited by R.K.Willardson and A.C.Beer. Academic Press, Vol. 3, 153 (1967).

64. D.M.Schleich and A.Wold. Mat.Res.Bull. 12, 111-114 (1977).

65. J.J.Hopfield. J.PHys.Chem. Solids 15, 97-107. (1960).

66. A.Miller, A.MacKinnon and D.Weaire, to appear in "Solid State Physics" edited by Ehreureich and Turnbull. Academic Press. (1981).

67. N.A.Gorganora, A.S.Poplavnoi, Y.Polygalov and Chadyshev. Phys. Stat. Solidi 39, 9-17, (1970).

68. J.L.Shay and B.Tell. Surf.Sci. 37, 748-762 (1973).

69. A.Shileika. Surf.Sci. 37, 730-747 (1973).

70. V.A.Chaldyshev, Poluprovoduiki, $A^2B^4C_2^5$, (Moskva : Soveskoe Radio). p. 212 (1974).

71. J.L.Shay and T.H.Wernick. "Ternary Chalcopyrite Semiconductors: Growth, Electronic Properties and Applications", Pergamon Press (1975).

72. A.Shileika "Ternary Compounds", (1977), ed. G.D.Holah, p. 129.

73. Y.P.Varshni, Physica 34, 149 (1967).

74. A.Manoogian and A.Leclerc. Phy.Stat.Sol. (b) 92, K23 (1979).

75. B.O.Seraphin and R.B.Hess, Phys. Rev. Letters. 14, 138 (1965).

76. G.Bonfiglioli and P.Brovetto, Appl.Optics, 3, 1417 (1964).

77. W.E.Engeler, H.Fritsche, M.Garfinkel and J.J.Tiemann. Phys.Rev.Letters, 14, 1069 (1965).

78. K.L.Shaklee and J.E.Rowe. Appl.Optics. 9, 627-632 (1970).

79. Ricardo R.L. Zucca and Y.R.Shen, Phys.Rev. B, 1, 2668-2676 (1970).

80. G.W.Engeler, H.Fritsche, M.Garfinkel and J.J.Tiemann. Phys.Rev.Letters, 14, 1069 (1965).

81. G.W.Gobeli and E.O.Kane, Phys.Rev.Letters, 15, 142, (1965).

82. F.H.Pollak and M.Cardona. Phys.Rev. 172, 816-933 (1968).

83. B.Batz. Solid State Comm. 4, 241 (1956).

84. M.Cardona, K.L.Shaklee and F.H.Pollak. Phys.Rev., 154, 696, (1967).

85. S.E.Schnatterly. Bull.Am.Phys.Soc., 13, 387, (1968).

86. R.E.Drew, Bull.Am.Phys.Soc. 12, 384 (1967).

87. A.Gilgore, P.J.Stoller and A.Fowler
Rev.Sci. Instrum. 36, 1535 (1967).

88. B.L.Evan and K.T.Thompson. Journal Scientific Inst. 2,
327 (1969).

89. T.O.Tuomi. Phys.Stat.Sol. 38, 623 (1970).

90. A.G.Thompson and J.E.Rowe. Journ.App.Phys. 40, 3280 (1969).

91. J.J.Loferski, J.Appl.Physics 27, 777 (1956).

92. W.Shockley and H.J.Queisser, J.Appl.Physics 32, 510 (1960).

93. K.J.Bachmann, E.Buehler, H.L.Shay and S.Wagner. Z.Phys.Chem.
NF 98, 365 (1975).